PhD Thesis

Lasse Bøhling

Computer Simulations of Viscous Liquids and Aspherical Particles

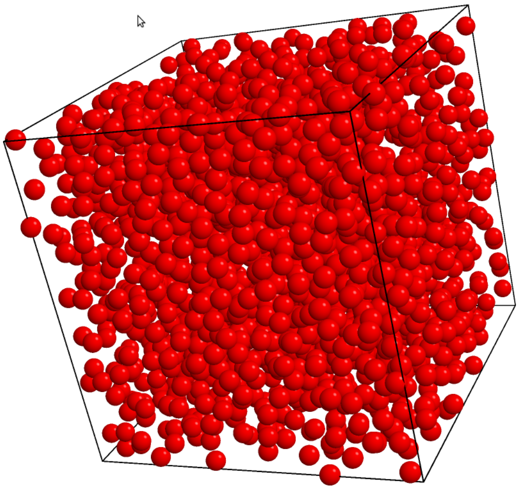

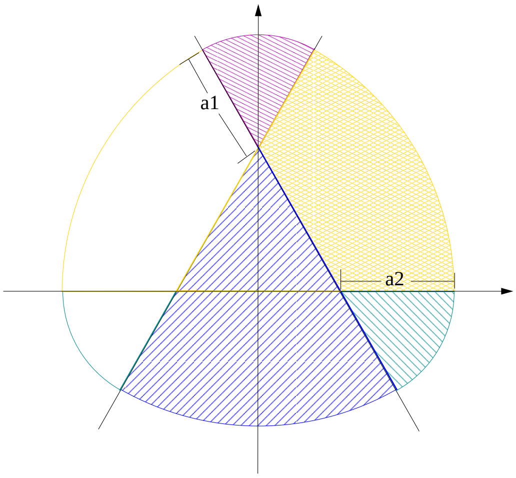

Thesis Advisor: Thomas Schrøder

Danish National Research Foundation
Centre for Viscous Liquid Dynamics

Glass and Time

Roskilde University

IMFUFA
Department of Science, Systems and Models

February 28, 2013

Abstract

This Ph.D. thesis falls into two basic parts. Part **I** explores a class of liquids commonly referred to as **Strongly Correlating Liquids**. The central aim of the first part of the study is to establish a better understanding of these liquids through an investigation of their pair interaction potential. Part **II** examines the socalled **rolypoly**-particle, an aspherical surface of constant width. This part of the study focuses on the self assembly and densest packing of this particle. The overall objective of this part of the study is to connect the shape of the particle directly to its glass forming ability. Both parts rely on theoretical observations combined with *Molecular Dynamics* and *Monte Carlo* simulations.

The main conlusions are as follows:

Part I For liquids with strong virial and potential energy fluctuations in the canonical ensemble, the two dimensional (density and temperature (ρ, T)) phase diagram can be reduced to one variable $(h(\rho)/T)$. The scaling function $h(\rho)$ is derived analytically for atoms interacting via a pair potential constituting a sum of Inverse Power Laws: $\phi(r) = \sum_n \varepsilon_n(\sigma_n/r)^n$. It is shown how the scaling function $h(\rho)$ directly links to the pair interaction potential.

Part II The glass forming ability of the rolypoly's is to a first approximation determined by the non-sphericity of the particle and for high pressures, crystallization is controlled by diffusion, consistent with classical nucleation theory. Densest packing is found for the Rolypoly with a packing fraction $\simeq 0.7698$, having two particles in the unit cell.

Keywords: Viscous liquids, isomorphs, glass transition, strongly correlating liquids, interaction potential, self assembly, densest packing, glass forming ability, aspherical particles

Abstract in Danish

Denne Ph.D. afhandling består af to dele. Første del undersøger en klasse af væsker kaldet **stærkt korrelerende væsker**. Formålet med dette studie er at forstå disse væsker gennem deres par potentiale. Anden del af afhandlingen udforsker en *næsten sfærisk* partikel kaldet **rolypoly**. Målet med dette studie er at vise en direkte sammenhæng mellem formen og dens evne til at krystallisere på den ene side og rolypolyens pakningstæthed på den anden side. Begge dele er teoretiske studier underbygget af *Molecular Dynamics* og *Monte Carlo* simuleringer.

De væsentligste konklusioner er som følger:

Del I For væsker med stærke viriale – potentielle energi fluktuationer i det kanoniske ensemble kan det to dimensionale faserum (densitet og temperatur (ρ, T)) reduceres til én variabel $(h(\rho)/T)$. Skalerings funktionen $h(\rho)$ er udledt analytisk for partikler der vekselvirker med et potentiale bestående af en sum af inverse potens funktioner $\phi(r) = \sum_n \varepsilon_n (\sigma_n/r)^n$. Det bliver vist hvordan skaleringsfunktionen $h(\rho)$ kan forstås ud fra det vekselvirkende par potential.

Del II Evnen til at krystallisere for rolypolyen kan til en første approksimation beskrives ved partiklens ikke sfæriske egenskab. Højtryks delen af krystalliserings kurverne er kontrolleret af diffusions koefficienten i væsken, konsistent med klassisk nukleations teori. Den tætteste pakning af rolypolyen fylder rummet med $\simeq 76.98\%$ med to rolypolyer i enheds cellen.

Nøgleord: Viskøse væsker, isomorfer, glas overgang, stærkt korrelerende væsker, vekselvirknings potential, krystallisering, tættest pakning, krystalliserings egenskab, ikke sfæriske partikler

Preface

This thesis is the outcome of my efforts as a Ph.D. student between March 2010 and February 2013. The predominant part of the thesis is made up of numerical analysis carried out in the simulation fraction of the Glass and Time group. The numerical analyses have been executed in the in-house gpu Molecular Dynamics program **RUMD** developed by the Glass and Time group.(see `rumd.org`). Enabled by vast computational resources a large number of simulations with different systems have been investigated. Only a few of those, however, have made it all the way to the thesis. Hopefully the ones that appear are those that best cast a light on the core issues of the thesis.

A visit to Professor Sharon Glotzers group at the University of Michigan in the early spring of 2012 forms the basis of the second part of this thesis. This second part of the thesis can be read independently of the first part. The character of the work in this section is fundamentally theoretical revolving around Monte Carlo simulations of a mathematical shape named the *rolypoly.* The programs **incsim** and **injavis** used are developed by the Glotzer group.

All data and figures in this thesis were produced and prepared by myself unless otherwise stated.

Lasse Bøhling
Roskilde University
February 2013

Acknowledgments

I wish to express my thanks to the people mentioned below for their help and support during my work as a Ph.D. student.

First of all I wish to thank my advisor Thomas Schrøder and Professor Jeppe Dyre for giving me the opportunity to join the "Glass and Time" group. It has been a true pleasure to work with and learn from such enthusiastic and intelligent scientists. I feel privileged to be part of a group with so many talented and gifted people and I sincerely appreciate the warm unpretentious and inspiring environment present in the group. Especially I want to thank the simulation people: Nicholas P. Bailey, Jesper S. Hansen, Søren Toxværd, Claire Lemarchand, Arno A. Veldhorst and Trond S. Ingebrigtsen. A special thanks to Heine Larsen for keeping the cluster up and running and taking care of every thinkable computer related problem and to Niels Boye Olsen for excellent collaboration.

I am thankful to Sharon Glotzer for opening the doors to the Glotzer group. I won't forget their kind hospitality. Michael Engel and Elizabeth R. Chen have been infinitely helpful with the implementation and problem solving of the rolypoly. Ulf R. Pedersen is acknowledged for an abundance of good ideas and inputs to the rolypoly.

Finally, my loving thanks go to my parents: Birgit and Poul, grandpa Jørgen and brother Frederik for moral support. Big thanks to my wonderful girlfriend Ida for her patience and understanding.

This work was financed by the Danish National Research Foundation Center for Viscous Liquids Dynamics "Glass and Time" Grant No. NRF61.

Papers

Paper I

A.A. Veldhorst, L. Bøhling, J.C. Dyre and T.B. Schrøder *Isomorphs in the phase diagram of a model liquid without inverse power law repulsion.* The European Physical Journal B, vol. 85, pages 1–7, 2012.

Paper II

Lasse Bøhling, Trond S. Ingebrigtsen, A Grzybowsk, M Paluch, Jeppe C. Dyre and Thomas B. Schrøder. *Scaling of viscous dynamics in simple liquids: theory, simulation and experiment.* New Journal of Physics, vol. 14, no. 113035, 2012.

Paper III

Trond S. Ingebrigtsen, Lasse Bøhling, Thomas B. Schrøder and Jeppe C. Dyre. *Thermodynamics of condensed matter with strong pressure-energy correlations.* Journal of Chemical Physics, vol. 137, no. 6, February 2012.

Paper IV

Lasse Bøhling, Arno A Veldhorst, Trond S Ingebrigtsen, Nicholas P Bailey, Jesper S Hansen, Søren Toxvaerd, Thomas B Schrøder and Jeppe C Dyre. *Do the repulsive and attractive pair forces play separate roles for the physics of liquids?* Journal of Physics: Condensed Matter, vol. 25, no. 3, page 032101, 2013.

Contents

Part I

Strongly Correlating Liquids and Isomorphs

Chapter 1
Introduction

In this chapter we introduce the concept of strongly correlating liquids and isomorphs. We investigate some consequences of strongly correlating liquids and derive a number of invariant properties.

1.1 Motivation and supercooled liquids

Glass is one of the oldest artificial materials used by humans. Traditional usages of glass include *optical fibers*, *ceramics*, *windows*, *containers*, *touch-screens* and of course *art work*. But also less known applications like *memory storage devices*, *thin films* and *amorphous pharmaceuticals* are playing an ever increasing role in financial growth sectors like the information-, energy- and medical industries [Ediger 2012]. From the earliest findings thousands of years ago up till now applications have continued to grow and thus the need for understanding the basic nature of this intriguing form of matter.

Glass is a liquid cooled fast enough to avoid crystallization. Below some critical temperature or pressure, the free energy of a crystal lattice becomes lower than that of the liquid. Given time to relax and reach equilibrium the particles of this liquid will arrange themselves into a crystal lattice [Dyre 2006]. If the kinetics of the particles, however, are slower than the cooling, the particles will never find the crystal lattice sites and will be frozen in this non equilibrium fluid configuration. In the Ehrenfest classification of phase transitions where the n'th order refer to the n'th derivative of the free energy displaying a discontinuity, there is no phase transition from a viscous liquid to a glass. A glass is simply defined as a very viscous liquid with shear viscosity $\geq 10^{12}$ Pa$\cdot$s. Despite this simple picture of what a glass is, many fundamental problems still remain unanswered.

1.2 Short introduction to Molecular Dynamics simulations

Molecular Dynamics simulations are used in a wide range of areas e.g. as material sciences, protein folding, DNA structure analysis, nucleation theory and several others. In this thesis molecular dynamics are used in the study of viscous liquids. The complexity of problems involving thousands of particles by far exceeds what is possible to solve analytically which is why we need numerical methods. A brief basic introduction to molecular dynamics simulation is presented in the following.

Newtons law defining the equations of motion for classical particles is used. Given the force for particle i as the gradient of the potential:

$$F_i = -\nabla_i \phi \tag{1.1}$$

and initial conditions for all particles positions and velocities is essentially all the information needed. We calculate new positions and velocities by stepping Δt forward in time using a discrete Leapfrog integration algorithm [Allen 2010]:

$$\begin{aligned} \mathbf{r}_i(t+\Delta t) &= \mathbf{r}_i(t) + \Delta t\, \mathbf{u}_i(t) + \frac{1}{2}(\Delta t)^2 F_i(t) \\ \mathbf{u}_i(t+\Delta t) &= \mathbf{u}_i(t) + \frac{1}{2}\Delta t\, [F_i(t) + F_i(t+\Delta t)] \end{aligned} \tag{1.2}$$

with $\mathbf{r}_i$ being the position of particle i, bold font indicating a vector: $\mathbf{r} = (r_x, r_y, r_z)$, and $\mathbf{u}_i$ as the velocity of particle i. Iterating this procedure with specific constraints depending on the ensemble, we calculate the motion and trajectories of the particles. In this thesis we are working in the canonical NVT ensemble meaning that we keep the numbers of particles N, the Volume V and Temperature T constant. The Nose-Hoover thermostat [Nosé 1984, Hoover 1985] is implemented in **RUMD** for thermal equilibration. See `rumd.org` for more information on our **gpu** accelerated MD program.

All potentials, except the standard Lennard Jones 12-6, in the thesis are implemented in **RUMD** by myself.

1.3 Introducing Strongly Correlating Liquids

Strongly Correlating Liquids (SCL) is a class of liquids introduced by the Glass and Time group [Bailey 2008a, Bailey 2008b, Schrøder 2009, Gnan 2009, Schrøder 2011]. The discovery of these liquids dates back to 2008 where the Glass and Time group identified this feature in a simulation of a Lennard–Jones fluid [Pedersen 2008]. Since then, more computer and real liquids have been identified as strongly correlating. The correlations refer to instantaneous equilibrium potential energy and virial fluctuations in the canonical ensemble. Recall that energy and pressure are divided into two terms, an ideal and an excess term; the ideal terms are functions of momenta and the excess are functions of positions:

$$\begin{aligned} E &= K(\mathbf{p}_1, ..., \mathbf{p}_N) + U(\mathbf{r}_1, ..., \mathbf{r}_N) \\ p &= Nk_BT(\mathbf{p}_1, ..., \mathbf{p}_N)/V + W(\mathbf{r}_1, ..., \mathbf{r}_N)/V. \end{aligned} \tag{1.3}$$

where $T(\mathbf{p}_1, ..., \mathbf{p}_N)$ is the kinetic temperature, $W(\mathbf{r}_1, ..., \mathbf{r}_N)$ the virial and K and U are kinetic and potential energies respectively. The virial is defined as [Allen 2010]

$$W = -\frac{1}{3}\sum_{i<j} r_{ij} \frac{\mathrm{d}\phi(r_{ij})}{\mathrm{d}r_{ij}} \tag{1.4}$$

where $\phi(r)$ is the interacting pair potential and r_{ij} is the distance between particles i and j. We neglect many body effects and just look at the pair interaction: $\phi(r) = \phi(r_{ij})$. The correlation between U and W is quantified by the standard correlation coefficient

$$R = \frac{\langle \Delta W \Delta U \rangle}{\sqrt{\langle (\Delta W)^2 \rangle \langle (\Delta U)^2 \rangle}}. \tag{1.5}$$

Angle brackets $\langle \cdots \rangle$ denote time and ensemble averages and Δ denotes deviation from mean value $\Delta X = X - \langle X \rangle$ and is the fluctuation. Strongly correlating liquids have correlation coefficient $R > 0.90$. An example of visualizing the correlation can be seen in figure 1.1 where the time evolution and instantaneous values of the potential energy and virial are plotted for a single component Lennard Jones liquid. The density of the system is given by the number density: $\rho = N/V$, where V is the volume and N is the total number of particles.

An important quantity we will use and discuss intensively is the density scaling exponent γ. An example is seen in figure 1.1. There are different ways of defining γ, but only one that keeps the excess entropy constant:

$$\gamma = \left(\frac{\mathrm{d}\ln T}{\mathrm{d}\ln \rho}\right)_{S_{ex}} = -\frac{\beta_V^{ex}}{c_V^{ex}} = \left(\frac{\partial W}{\partial U}\right)_V = \frac{\langle \Delta U \Delta W \rangle}{\langle (\Delta U)^2 \rangle}\,, \tag{1.6}$$

β_V^{ex} and c_V^{ex} is the excess isochoric thermal pressure and heat capacity respectively. The theory of strongly correlating liquids concern excess quantities. These relations are derived in [Gnan 2009] and [Schrøder 2011]. This is the γ that will be used in the rest of this thesis.

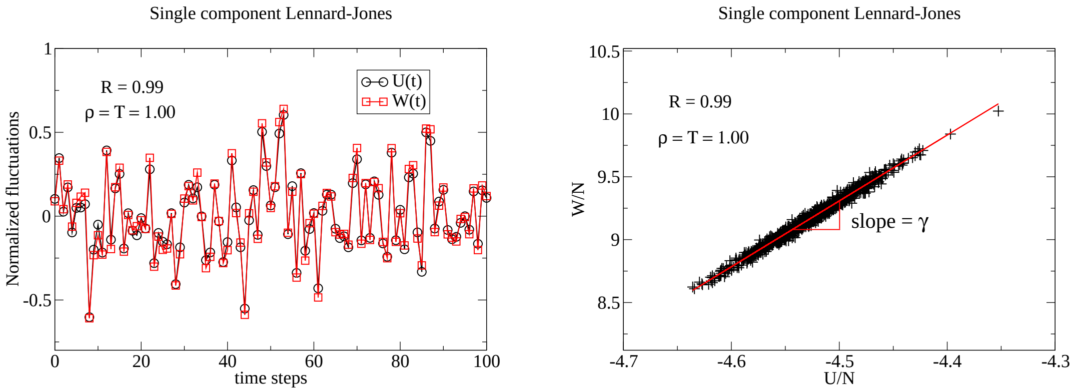

Figure 1.1: UW correlation. Left: Normalized fluctuations as a function of time. Right: Scatter plot: potential energy per particle plotted against the virial per particle. The slope gives the effective exponent γ. See eq. (1.6) for definition.

In appendix A of paper 4 [Gnan 2009] it is shown that if a liquid is strongly correlating it has isomorphs and if it has isomorphs then it is strongly correlating. Isomorphs are state points in the phase diagram with identical reduced dynamics and structure [Gnan 2009]. We denote reduced units with a tilde. Length and energy are given by:

$$\tilde{r} = \rho^{1/3} r \qquad \text{and} \qquad \tilde{\varepsilon} = \frac{\varepsilon}{k_B T} \tag{1.7}$$

Two state points (1) and (2) are said to be isomorphic if pairs of scaled micro configurations $\tilde{\mathbf{r}}^{(1)} = \tilde{\mathbf{r}}^{(2)}$ (reduced units) have proportional canonical (NVT) configurational Boltzmann factors

$$\exp\left(-\frac{U\left(\mathbf{r}_1^{(1)},...,\mathbf{r}_N^{(1)}\right)}{k_BT_1}\right) = C_{12}\exp\left(-\frac{U\left(\mathbf{r}_1^{(2)},...,\mathbf{r}_N^{(2)}\right)}{k_BT_2}\right) \tag{1.8}$$

The proportionality factor C_{12} depends only on state point and is the same for all micro configurations. An isomorph is a line in the phase diagram where all points on the line obey eq (1.8). From this it can be shown that many quantities are invariant along this isomorph [Gnan 2009]. See section II of paper [Gnan 2009] and paper [Schrøder 2011] for a thorough definition and discussion of the isomorphs. The following list show some of the important invariant quantities:

- Reduced structure: $g(\tilde{r})$
- Reduced dynamics: $\tilde{D}$
- Excess entropy: S^{ex}
- Isochoric specific heat: C_V^{ex}
- Normalized auto correlation functions
- Infinite shear modulus: $G_\infty/\rho k_BT$

Structure is quantified by the radial distribution function $g(r)$ and to realize that the reduced structure $g(\tilde{r})$ is an isomorph invariant we notice that using reduced coordinates corresponds to scaling the isomorphic state points onto each other with density. State point (1) with density ρ_1 have reduced coordinates $\tilde{\mathbf{r}}^{(1)} = \rho_1^{1/3}\mathbf{r}^{(1)}$ and state point (2) with density ρ_2 have reduced coordinates $\tilde{\mathbf{r}}^{(2)} = \rho_2^{1/3}\mathbf{r}^{(2)}$. The isomorph invariance follows from the definition of isomorphic state points, that the micro configurations trivially scale into each other: $\tilde{\mathbf{r}}^{(1)} = \tilde{\mathbf{r}}^{(2)}$.

The time evolution is governed by Newtons second law. The force on the i'th particle is given by:

$$\mathbf{F_i} = m_i\frac{\mathrm{d}^2\mathbf{r}_i}{\mathrm{d}t^2}\,, \tag{1.9}$$

with $\mathbf{F_i} = -\nabla_{\mathbf{r}_i}\phi$. In order to identify the reduced force as an isomorph invariant, we rewrite the force in terms of reduced time and mass:

$$\tilde{t} = \rho^{1/3}\sqrt{\frac{k_BT}{m}}\,t \qquad \text{and} \qquad \tilde{m}_i = \frac{m_i}{m} \tag{1.10}$$

where m is the average particle mass. The reduced force is then seen to be:

$$\tilde{\mathbf{F}}_\mathbf{i} = -\nabla_{\tilde{\mathbf{r}}_i}\tilde{\phi} = \tilde{m}_i\frac{\mathrm{d}^2\tilde{\mathbf{r}}_i}{\mathrm{d}\tilde{t}^2} = \rho^{-1/3}(k_BT)^{-1}\mathbf{F_i} \tag{1.11}$$

and because it is a function of reduced particle coordinates $\tilde{\mathbf{r}}_\mathbf{i}$, we know from the previous paragraph that these are identical in reduced units. It then follows that the reduced force and therefore also reduced dynamics is invariant for all state points on the isomorph.

1.4 Generating isomorphs in computer simulations

The method used to generate isomorphs in small steps is described in detail in [Schrøder 2011]. This procedure does not assume any simplicity of the potential and can be used for any strongly correlating system. It has the disadvantage that it is only possible to explore small parts of the phase diagram. It relies on the assumption that the density scaling exponent γ is constant for small density changes. Rearranging and integrating the first equality in equation (1.6) with γ constant we find:

$$\gamma \int \mathrm{d}\ln\rho = \int \mathrm{d}\ln T \quad \Rightarrow \quad \frac{\rho^{\gamma}}{T} = C, \tag{1.12}$$

where C is an integration constant. From one state point (ρ_1, T_1), density is changed by a small amount ($\sim$1%) and the temperature at the isomorphic state point (ρ_2, T_2) is being calculated using power law density scaling with the exponent γ calculated from eq. (1.6) at state point (1):

$$\frac{\rho_1^{\gamma}}{T_1} = \frac{\rho_2^{\gamma}}{T_2} \,. \tag{1.13}$$

The temperature at state point (2) is then found by rearranging equation (1.13).

An example of an isomorph generated by eq. (1.13) can be seen in figure 1.2 where the structure and dynamics are shown for a simulation of the Kob-Andersen Binary Lennard Jones (KABLJ) liquid [Kob 1994] with $N = 1000$ particles. The structure is probed by the radial distribution function and the dynamics by the self part of the incoherent intermediate scattering function. Both for the big A particles in reduced units. The starting state point is $(\rho, T) = (1.20{,}0.458)$, then density is changed by 1% up and down 4-5 times resulting in the state points seen in figure 1.2 and 1.3. For comparison we plot two state points at the same density as the starting state point ($\rho = 1.20$) and temperatures close to the lowest and highest temperature on the isomorph: $T = 0.42$ and $T = 0.69$.

Invariance of structure and dynamics lead to many properties and so these will be the most displayed. In the potential-virial phase space $(U - W)$ we have a parametric description of the isomorphs. It is derived in section III **A** of [Schrøder 2011] using the invariance of structure. We write the potential and virial energies as a sum of two inverse power laws with exponents m and n:

$$U = U_m + U_n \qquad \text{and} \qquad W = \left(\frac{m}{3}\right) U_m + \left(\frac{n}{3}\right) U_n \,. \tag{1.14}$$

Let 0 denote a reference to the starting state point and $\tilde{\rho} = \rho/\rho_0$ as reduced density. Each term in the potential energy has a simple scaling:

$$U_k = \tilde{\rho}^{k/3} U_{k,0} \tag{1.15}$$

Inserting equation (1.15) in (1.14) we recognize these equations as a parametric description of isomorphs in the $U - W$ phase diagram with density $\tilde{\rho}$ as the free parameter:

$$U = \tilde{\rho}^{m/3} U_{m,0} + \tilde{\rho}^{n/3} U_{n,0} \tag{1.16}$$

$$W = \left(\frac{m}{3}\right) \tilde{\rho}^{m/3} U_{m,0} + \left(\frac{n}{3}\right) \tilde{\rho}^{n/3} U_{n,0} \tag{1.17}$$

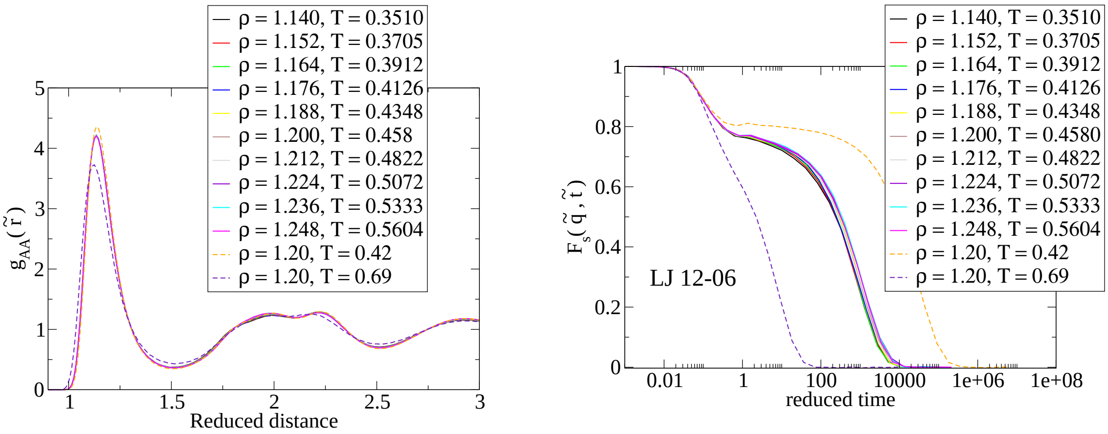

Figure 1.2: Structure and dynamics for an isomorph with the Kob-Andersen system. Left: the radial distribution function. Right: Self part of the incoherent intermediate scattering. The q vector is also in reduced units and is calculated as $\tilde{q} = 7.25(\rho/1.20)^{1/3}$. Potential and virial energies for these state points are black plusses in figure 1.3.

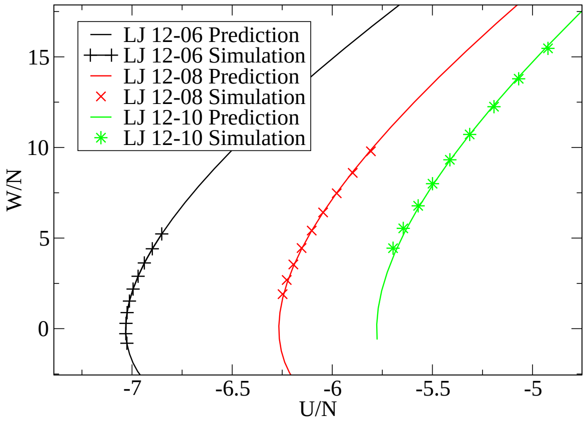

Figure 1.3: Potential and virial energy. The solid lines are the prediction from [Schrøder 2011] and the symbols are the simulated state points. Structure and dynamics for the LJ 12-6 potential can be seen in figure 1.2.

These parametric equations are plotted against simulation data for three different generalized Lennard-Jones potentials with exponents: 12-6, 12-8 and 12-10. It is the Kob-Andersen system for all of them. See next chapter for an introduction to these systems. The correlation is not 100 % and there is some deviation from the prediction to the actual simulated data – this is the nature of the isomorphs. Only pure Inverse Power Law (IPL) systems have 100 % correlation. As can be seen on figure 1.2 the dynamics are more sensitive than the structure and we will mostly probe the dynamics for the KABLJ liquid.

A new way to generate isomorphs is introduced in chapter 3 utilizing the fact that we now have an explicit expression for the density dependence of γ [Paper II]. This paper introduce what we in the Glass and Time group informally call: *The long density jump formula.* It refers to the fact that with this method it is possible to change density more than a factor of 10 (1000%) and still achieve good isomorphs, instead of jumping 1% at the time. By using this method we are able to explore greater parts in the phase diagram that would otherwise be impossible to reach.

Chapter 2

Four generalized Lennard-Jones potentials

We investigate four different generalized Lennard-Jones potentials for the (KABLJ) system. It is done by simulating an isomorph and an isochore for each system in the NVT ensemble. We extract several quantities for these systems, but will focus mostly on the excess infinite frequency shear modulus: G_∞^{ex}. We calculate G_∞^{ex} in two ways: first by integrating the radial distribution function and then from the transient elastic modulus $G(t)$. A prediction of the temperature dependence of G_∞^{ex} on isochores exploiting Rosenfeld - Tarazona scaling and isomorph theory is tested in section 2.2.8. From the plateau value of the transient elastic modulus $G(t)$ we test the Shoving model. In section 2.4 we compare two fitting functions and finish this chapter by discussing quasi universality in section 2.5.

2.1 Introducing the systems

The generalized Lennard–Jones potentials is defined as

$$\phi_{\alpha\beta}(r_{ij}) = \frac{\varepsilon_{\alpha\beta}}{m-n}\left\{ n\left(\frac{\sigma_{\alpha\beta}}{r_{ij}}\right)^m - m\left(\frac{\sigma_{\alpha\beta}}{r_{ij}}\right)^n \right\} . \tag{2.1}$$

The subscripts ij point out that it is a pair potential and r_{ij} is the distance between particle i and particle j. For systems with more than one component, the potential between different species are designated α and β. The system used here is the Kob-Andersen Binary Liquid [Kob 1994] (KABLJ) which is reluctant to crystallize due to its strong interaction between small and big particles [Toxvaerd 2009]. The parameters for the KABLJ liquid is: $\varepsilon_{AA} = 1.00$, $\sigma_{AA} = 1.00 \cdot 2^{1/6}$, $\varepsilon_{AB} = 1.50$, $\sigma_{AB} = 0.80 \cdot 2^{1/6}$ and $\varepsilon_{BB} = 0.50$, $\sigma_{BB} = 0.88 \cdot 2^{1/6}$. All simulations have been running with a total of $N = 1000$ particles, 800 A particles and 200 B particles and we adopt the unit system with $k_B = 1.0$. Because of its superiority in numbers and size the A particles dominate the physics of the entire system and we will mostly focus on the A particles.

In this study we keep the repulsive exponent $m = 12$ fixed and vary the attractive exponent n in steps of 2 from 4 to 10. The r^{-6} attraction in the Lennard-Jones potential describes the dipole-dipole interaction between atoms. Higher order terms like dipole-quadrupole (r^{-8}) and quadrupole-quadrupole (r^{-10}) interactions are usually small compared to the dipole-dipole interaction [Hansen 1986].

The AA interaction potentials are plotted in figure 2.1 together with the 12-6 Kob-Andersen potentials. They are all, except the 12-4, cut and shifted in $r_{cut} = 2.5\sigma_{\alpha\beta}$ which

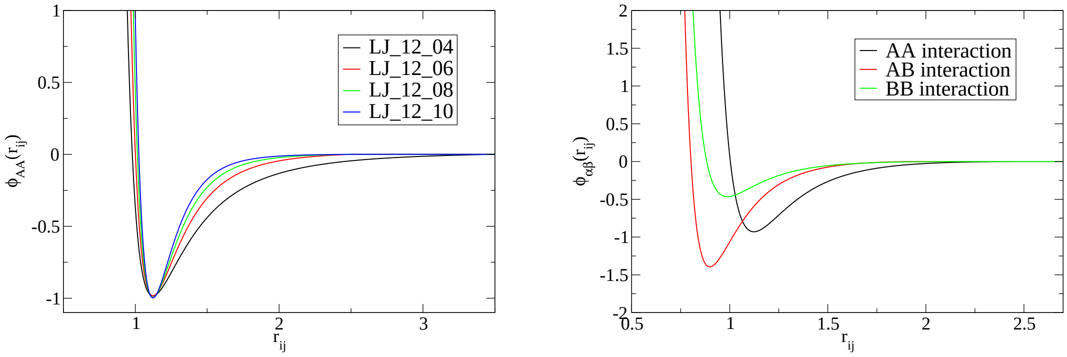

Figure 2.1: Left: Generalized Lennard-Jones potentials. The repulsive exponent $m = 12$ is fixed and the attractive exponent n is varied in steps of 2 from 4 to 10. A higher attractive exponent results in a steeper potential. Right: The Kob-Andersen potentials.

is cut and shifted in $r_{cut} = 3.5\sigma_{\alpha\beta}$ to ensure the minima has the same strength/depth as the others.

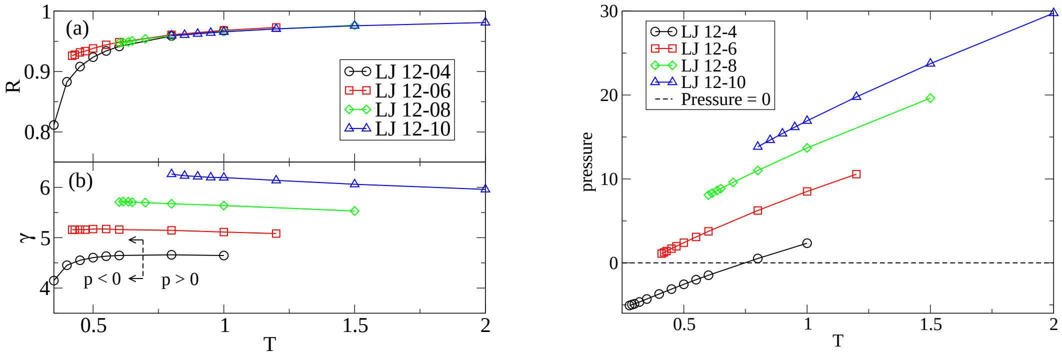

Figure 2.2: Correlation coefficient R and γ on isochores with density $\rho = 1.20$ for the four different potentials. All the potentials are strongly correlating. Only the 12-4 LJ falls below 0.90 at low temperatures where pressure becomes negative. The dynamics, quantified by the self part of the incoherent intermediate scattering function can be seen in figures 2.3 and 2.4.

Figure 2.2 show four isochores for the above mentioned potentials and all of them are strongly correlating in most parts of the phase diagram, only the 12-4 potential falls below 0.90 at low temperatures. Around this temperature the pressure becomes negative and the physics of the simulations changes. Despite the different physics we continue to include all the state points from the 12-4 potential. The lowest temperature for each of the potentials corresponds more or less to the same relaxation time. The temperature is 0.42 at density 1.20 for the 12-6 potential - a quite viscous state point. See figures 2.3 and 2.4 for the dynamics of the 4 isochores where the self part of the incoherent intermediate scattering function has been calculated for the A particles.

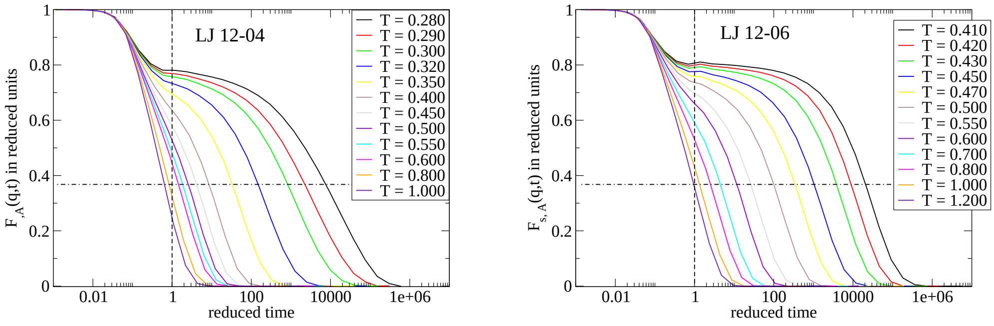

Figure 2.3: Self part of the Incoherent intermediate Scattering function $F_s(\tilde{q}, \tilde{t})$ for the big A particles in reduced units. Left the 12-4 potential. Right: the 12-6 potential. Broken vertical line indicates where the fitting in sec. 2.4.2 has been performed and the horizontal dashed line is the relaxation time where it is decayed to $\exp(-1)$.

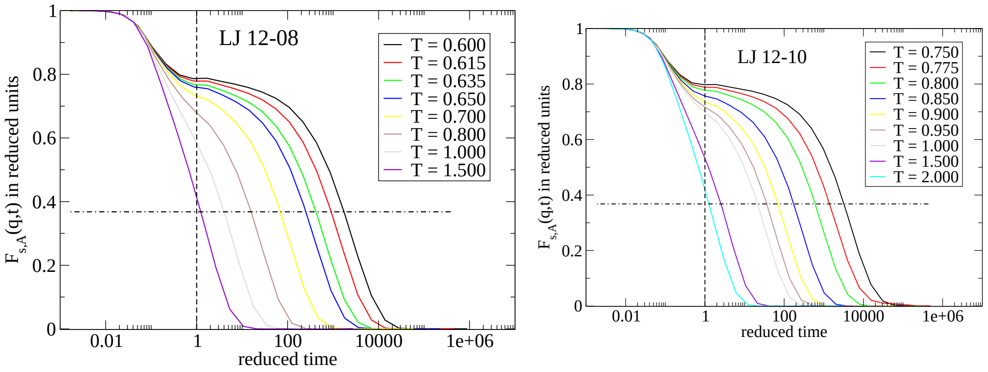

Figure 2.4: Self part of the Incoherent intermediate Scattering function $F_s(\tilde{q}, \tilde{t})$ for the big A particles in reduced units. Left the 12-8 potential. Right: the 12-10 potential. Broken vertical line show where the plateau value is extracted and the horizontal broken–dotted line is the relaxation time where it is decayed to $\exp(-1)$.

Isomorphs for the different potentials was simulated with the same starting density for all ($\rho = 1.20$). An illustrative isomorph for the 12-10 potential is shown on figure 2.5, where structure, dynamics, energies, correlation and scaling exponent γ is plotted. The starting state point for this isomorph is the $(\rho, T) = (1.20,\ 0.80)$ green line in figure 2.4 for the 12-10 Lennard-Jones potential. As seen on this figure, the correlation decreases when temperature (and therefore also density) decreases. The scaling exponent γ also decreases and will at very high temperatures and densities reach $12/3 = 4$ due to the repulsive exponent $m = 12$ controlling the physics at very high densities. The calculated UW state points does not follow the prediction rigorously, but is to a good approximation on the predicted isomorph. For the dynamics we probe the mean squared displacement and see that these curves are less invariant than the structure. The small B particles are faster than the A particles. The AB and BB radial distribution functions are less invariant than the AA distribution. This is a general trend for the Kob-Andersen liquid.

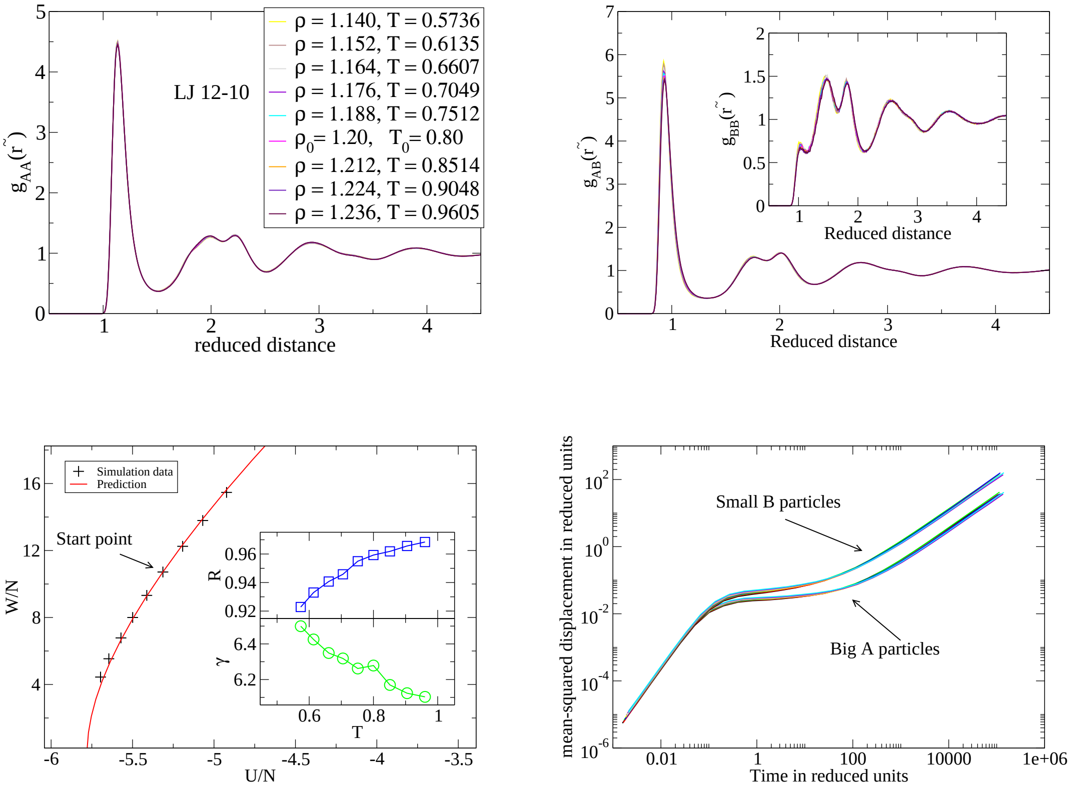

Figure 2.5: An isomorph for the 12-10 potential KABLJ. The starting state point is (ρ_0, T_0) $=$ (1.20, 0.80). Two figures on top show the radial distribution functions for the, left: AA distribution, right: AB and inset BB. Bottom left is the potential-virial mean energy plotted. The prediction from [Schrøder 2011] is also plotted as a red line, see eq. (1.15) for the parametric description and the starting state point is indicated. Inset shows the correlation coefficient and scaling exponent γ as a function of temperature. Bottom right shows the mean squared displacement for the A and B particles.

Choosing an isomorph for one of the other potentials will look very similar, all the trends are the same. The main difference is the density scaling exponent γ that, due to the change in attractive exponent will be lower. See figure 2.2. The reason to include more than the normal LJ (12,6) potential is threefold

1. Generality
2. Analytical solutions exists as functions of the exponents
3. Observing the effect of tuning the attractive term

2.2 Shear modulus

One of the predictions from the isomorph theory is that the infinite frequency shear modulus is invariant in reduced units [Gnan 2009] (section 3f). All normalized time correlation functions expressed in reduced units are predicted to be invariant [Gnan 2009] (section 3c). This follows from the fact that the reduced force is isomorph invariant, as shown in section 1.3. If the normalization is done by dividing with the mean of the squared: $\langle A^2 \rangle$ with A being any time auto correlation function, we ensure the correlation functions amplitudes to be equal.

In the following chapter the invariance of the infinite shear modulus $G_\infty/\rho T$ and the infinite bulk modulus $K_\infty/\rho T$ is tested for the Kob-Anderson binary liquid [Kob 1994]. The infinite shear modulus is calculated first by integrating over the radial distribution function and compared to the zeroth time transient elastic modulus $G(t)$. We find these two methods consistent if we include a tail correction to the integral over the radial distribution function.

By rewriting the integral to calculate the infinite shear modulus in terms of potential energy and virial, we use the isomorph theory together with Rosenfeld–Tarazona scaling [Rosenfeld 1998] to predict G_∞^{ex} on an isochore. We also show that the plateau value from the transient elastic modulus is more invariant on an isomorph than the truly instantaneous. The temperature dependence of these quantities are seen to be monotonic with opposite signs, consistent with other findings for the transient elastic modulus [Yoshino 2010].

First a motivation for calculating these quantities is given. Consult appendix A for a macro– and micro–scopic description of these quantities. The transient elastic modulus is calculated from the off diagonal elements of the stress tensor.

2.2.1 Motivation

When a viscous liquid is cooled, the relaxation time increases dramatically approaching the glass transition temperature. To understand this behavior is one of the big scientific challenges in the glass community. The Arrhenius expression for the relaxation time is given by:

$$\tau_\alpha = \tau_0 \exp\left(\frac{\Delta E(T)}{k_b T}\right) \tag{2.2}$$

where τ_0 is a characteristic microscopic time ($\tau_0 \sim 10^{-13} s$) and $E(T)$ is an activation energy, the subscript α refers to the structural relaxation time. What is the function $E(T)$? Arrhenius behavior implies that $\Delta E(T) = \Delta E$, so the relaxation time is linear in an Angell $(T^{-1}, log(\tau_\alpha))$ plot [Angell 1995]. This behavior is not universal and most liquids has a non-exponential behavior of the relaxation time. Different models have different suggestions of how this function should be. Elastic models, like the shoving model [Dyre 1996], suggests that it should be the high frequency shear modulus times a characteristic volume V_c

$$\frac{\Delta E(T)}{k_b T} \propto \frac{V_c G_\infty}{k_b T} \tag{2.3}$$

Since structure changes very little approaching the glass transition, the characteristic volume V_c is assumed constant in the Shoving model.

2.2.2 Infinite frequency shear and bulk modulus

The shear and bulk modulus are in experiments measured in the frequency regime and related to the frequency dependent viscosities by $G(\omega) = i\omega\eta(\omega)$ with ω being frequency and η the frequency dependent shear viscosity and $K(\omega) = K_0 + i\omega\eta_V(\omega)$ with η_V being the frequency dependent bulk viscosity and K_0 being the zero frequency bulk modulus:

$$K(\omega = 0) = K_0 = -V \frac{\partial P}{\partial V}\bigg|_{S,T} . \tag{2.4}$$

The subscript S, T refers to the adiabatic or isothermal bulk modulus respectively, dependent on whether entropy or temperature are held constant. The zero frequency shear modulus vanish, but the bulk modulus does not. When we calculate the limit of infinite frequency we refer to the limit of the frequency dependent viscosities:

$$G_\infty = \lim_{\omega\to\infty} i\omega\eta(\omega) = \qquad K_\infty = K_0 + \lim_{\omega\to\infty} i\omega\eta_V(\omega) . \tag{2.5}$$

By converting frequency to time it is shown in [Zwanzig 1965] how to calculate the transient elastic modulus. Here we present the results:

$$G_\infty = \rho k_B T + \frac{2\pi}{15}\rho^2 \int_0^\infty \mathrm{d}r g(r) \frac{\mathrm{d}}{\mathrm{d}r}\left[r^4 \frac{\mathrm{d}\phi(r)}{\mathrm{d}r}\right] \tag{2.6}$$

$$K_\infty - K_0 = \frac{2}{3}\rho k_B T + P + \frac{2\pi}{9}\rho^2 \int_0^\infty \mathrm{d}r g(r) r^3 \frac{\mathrm{d}}{\mathrm{d}r}\left[r \frac{\mathrm{d}\phi(r)}{\mathrm{d}r}\right] \tag{2.7}$$

The equations in (2.6) and (2.7) are the equations for single component fluids. For a binary mixture, as we will use them, the infinite shear modulus becomes:

$$G_\infty = \rho k_B T + \frac{2\pi}{15}\rho^2 \sum_{i,j=1}^{2} x_i x_j \int_0^\infty \mathrm{d}r g_{ij}(r) \frac{\mathrm{d}}{\mathrm{d}r}\left[r^4 \frac{\mathrm{d}\phi_{ij}(r)}{\mathrm{d}r}\right] \tag{2.8}$$

and the bulk modulus:

$$K_\infty - K_0 = \frac{2}{3}\rho k_B T + P + \frac{2\pi}{9}\rho^2 \sum_{i,j=1}^{2} x_i x_j \int_0^\infty \mathrm{d}r g_{ij}(r) r^3 \frac{\mathrm{d}}{\mathrm{d}r}\left[r \frac{\mathrm{d}\phi_{ij}(r)}{\mathrm{d}r}\right] \tag{2.9}$$

where $i, j = 1$ indicate A particles and $i, j = 2$ indicate B particles. x_1 is the fraction of A particles and x_2 is the fraction of B particles ($x_1 + x_2 = 1$). g_{ij} is the radial distribution function for the $i - j$ interaction and likewise for the potential ϕ_{ij}. The simulations are performed with the Kob-Andersen parameters.

2.2.3 Invariance of G_∞ and $K_\infty - K_0$

Like other predictions for isomorph invariance, we need to express the quantity in reduced units. In paper [Gnan 2009] section 3f. it is argued that $G_\infty/(\rho k_B T)$ is an isomorph invariant. Inserting reduced units in eq. (2.6) leads to:

$$G_\infty = \rho k_B T + \frac{2\pi}{15}\rho k_B T \int_0^\infty \mathrm{d}\tilde{r}\, g(\tilde{r}) \frac{\mathrm{d}}{\mathrm{d}\tilde{r}} \left[\tilde{r}^4 \frac{\mathrm{d}\tilde{\phi}(\tilde{r})}{\mathrm{d}\tilde{r}} \right], \tag{2.10}$$

and by dividing eq. (2.10) with $\rho k_B T$ we have something that only depends on reduced units on the right hand side. To see that this in fact is an isomorph invariant, consult section 2.2.4 where it is shown that the integral can be written as a function of the reduced force times reduced length. In what follows we focus on the excess shear modulus $G_\infty^{ex} = G_\infty - \rho k_B T$ and we also use the unit system with $k_B = 1$. We do not have a theory for the infinite bulk modulus and the invariance can not be deduced from equation (2.9). The excess bulk modulus is, like the shear, defined as: $K_\infty^{ex} - K_0 = K_\infty - K_0 - \rho k_B T$.

Figure 2.6 display the temperature dependence of G_∞^{ex} and $K_\infty^{ex} - K_0$ on different isomorphs and isochores. It is seen that the isomorphs are more constant than the isochores. To quantify how invariant these modulus are on isomorphs and isochores the logarithmic derivative is used.

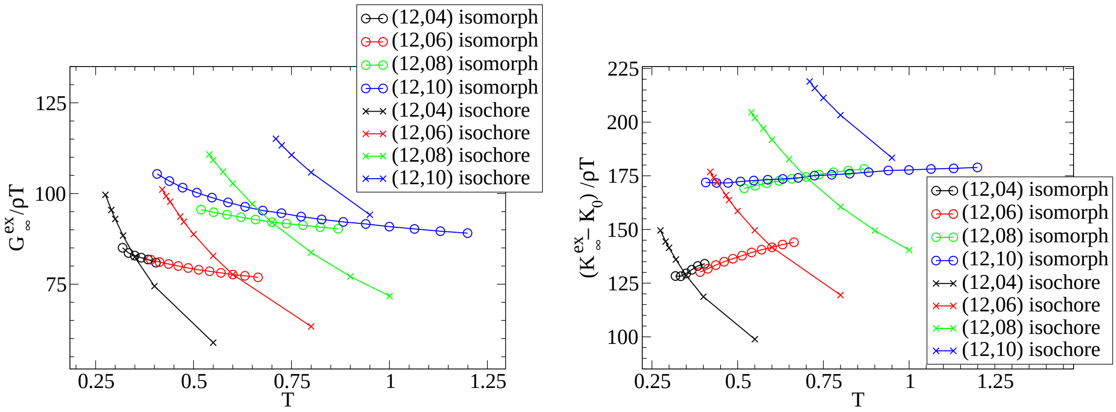

Figure 2.6: Testing invariance of the excess infinite shear and bulk modulus. Left: Reduced infinite shear modulus. Right: Reduced infinite bulk modulus. All on four different isomorphs and four different isochores $\rho = 1.2$ for all the isochores. It is clear that the isochores are changing more than the isomorphs, but the isomorphs are not perfectly constant.

This gives a relative measure of how much the reduced G_∞^{ex} or $K_\infty^{ex} - K_0$ varies as a function of temperature on isomorphs and isochores.

$$\left. \frac{\partial \ln \tilde{G}_\infty^{ex}}{\partial \ln T} \right|_x \tag{2.11}$$

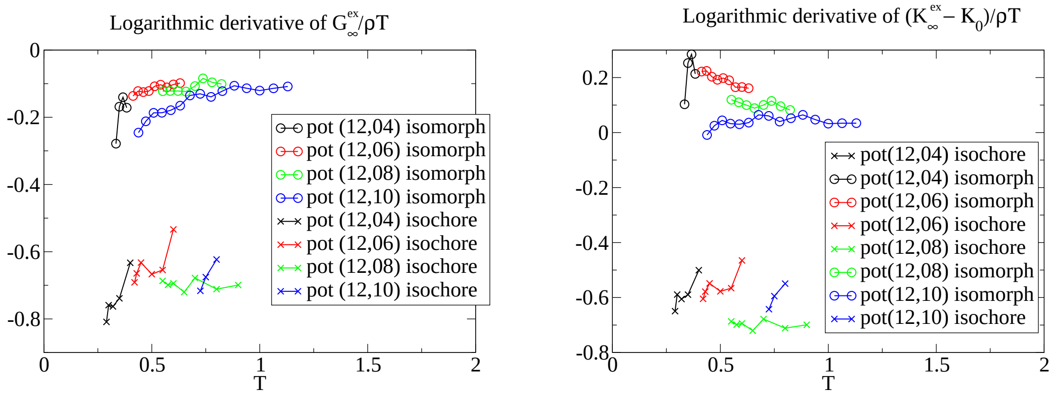

Figure 2.7: Logarithmic derivative $\partial \ln \tilde{G}^{ex}_{\infty}/\partial \ln T|_{x}$. All the isomorphs has a constant relative variation of ~ 0.2 for G^{ex}_{∞} and -0.2 for $K^{ex}_{\infty} - K_0$ whereas the isochores has values around 0.65. This implies that both G^{ex}_{∞} and $K^{ex}_{\infty} - K_0$ are to a good approximation invariant in reduced units.

where $\tilde{G}^{ex}_{\infty} = G^{ex}_{\infty}/\rho T$ is the reduced shear modulus and the x is indicating what to keep constant (volume=isochore or excess entropy=isomorph). It is predicted that the infinite shear modulus in reduced units is invariant on an isomorph.

The infinite shear and bulk modulus are too a good approximation invariant in reduced units. The invariance becomes better at higher densities and temperatures.

2.2.4 Shear modulus from the stress auto correlation function

From the autocorrelation function of the off diagonal elements of the stress tensor, the time dependence of the shear modulus is calculated [Zwanzig 1965]. We call this function the transient elastic modulus:

$$G(t) = \frac{1}{Vk_BT}\langle \sigma_{xy}(0)\sigma_{xy}(t)\rangle \,. \tag{2.12}$$

The stress tensor is microscopically defined as

$$\sigma_{xy} = \sum_{i}^{N}\left(\frac{p_i^x p_i^y}{m} + F_i^x y_i\right) \tag{2.13}$$

where p_i^x is the momenta in the x direction for the i'th particle, F_i^x is the force in the x direction and so forth. Here we have omitted the time dependence (t) on the force, position and momenta for notation clarity. Assuming an isotropic liquid, all off diagonal elements are identical.

In order to identify the instantaneous shear modulus $G(0)$ as an isomorph invariant we rewrite equation (2.12) in reduced units. Inserting the microscopic description for the stress (eq. (2.13)), we get four terms and notice that the two cross terms connecting kinetic and potential contributions are uncorrelated and therefore vanish. Symmetry considerations means any odd power of momenta are zero, x and y factorize-s in the average and the kinetic temperature is $\langle (p_i^x)^2/m\rangle = k_BT$. Recalling the number density is $\rho = N/V$ means the kinetic term is:

$$\frac{1}{Vk_BT}\left\langle \sum_i^N \left(\frac{p_i^x p_i^y}{m}\right) \sum_j^N \left(\frac{p_j^x p_j^y}{m}\right)\right\rangle = \rho k_BT\,. \tag{2.14}$$

Which is seen to be the ideal term in the integral formulation of equation (2.12). Denoting reduced variables with a tilde, length is scaled as: $\tilde{x} = \rho^{1/3}x$, and the reduced force in the x direction is: $F_i^x = -k_BT\rho^{1/3}(\partial\tilde{\phi}/\partial\tilde{x})$ where ϕ is the inter acting potential. Leading to the potential term expressed in reduced units:

$$\frac{1}{Vk_BT}\left\langle\left(\sum_i^N F_i^x y_i\right)^2\right\rangle = \frac{\rho k_BT}{N}\left\langle\left(\sum_i^N \frac{\partial\tilde{\phi}}{\partial\tilde{x}_i}\tilde{y}_i\right)^2\right\rangle \tag{2.15}$$

The isomorph invariance for the instantaneous shear modulus follow by inserting equation (2.15) in equation (2.12) and dividing ρk_BT over:

$$\frac{G_\infty}{\rho k_BT} = 1 + \frac{1}{N}\left\langle\left(\sum_i^N \frac{\partial\tilde{\phi}}{\partial\tilde{x}_i}\tilde{y}_i\right)^2\right\rangle\,. \tag{2.16}$$

Recognizing the right hand side as a reduced force $\partial\tilde{\phi}/\partial\tilde{x}_i$, times a reduced length, we know from section 1.3 that this is an isomorph invariant.

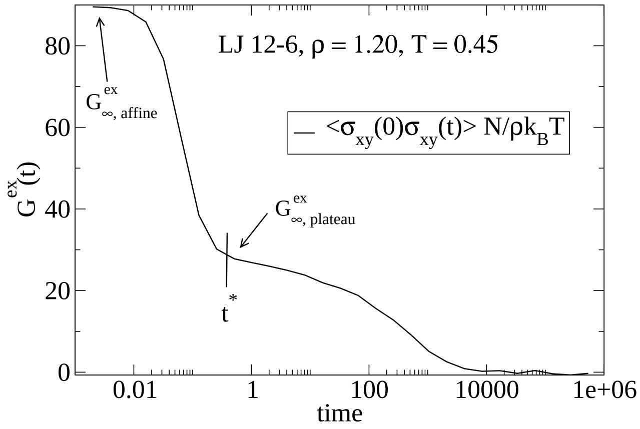

Figure 2.8: Time dependence of the transient elastic modulus $G^{ex}(t) = N\langle\sigma^{xy}(t)\sigma^{xy}(0)\rangle/(\rho k_BT)$ for state point $(\rho, T) = (1.2,\ 0.45)$. It is seen that there exist a two step relaxation. The infinite frequency plateau value is defined as $G^{ex}_{\infty,p} = G^{ex}(t^*)$ where t^* is after the first relaxation on the plateau.

In figure 2.8 it is seen that there exist a two step relaxation function for the stress autocorrelation. The value at $t = 0$ corresponds to the G^{ex}_∞ (2.8). It is also possible to define a plateau value $G^{ex}_{\infty,p}$. In this work a specific reduced time t^* is chosen, after the first relaxation, before it has decayed on the plateau. See figure 2.8.

2.2.5 Consistency check

Because the limits in the integral of eq. (2.8) is from $r = 0$ to $r = \infty$ and the simulations are running in a box with periodic boundary conditions, the radial distribution function is only calculated up to half the box length $L/2$. From there on it is assumed that the radial distribution function is 1. Assuming the radial distribution function $g(r)$ to be 1 at $L/2$ and outward makes a small difference.

$$G^{ex}_{\infty} = \frac{2\pi}{15}\rho^2 \left(\int_0^{L/2} \mathrm{d}r g(r) \frac{\mathrm{d}}{\mathrm{d}r}\left[r^4 \frac{\mathrm{d}\phi(r)}{\mathrm{d}r} \right] + \int_{L/2}^{\infty} \mathrm{d}r \frac{\mathrm{d}}{\mathrm{d}r}\left[r^4 \frac{\mathrm{d}\phi(r)}{\mathrm{d}r} \right] \right). \tag{2.17}$$

The last term in equation (2.17) (the tail correction) are calculated analytically.

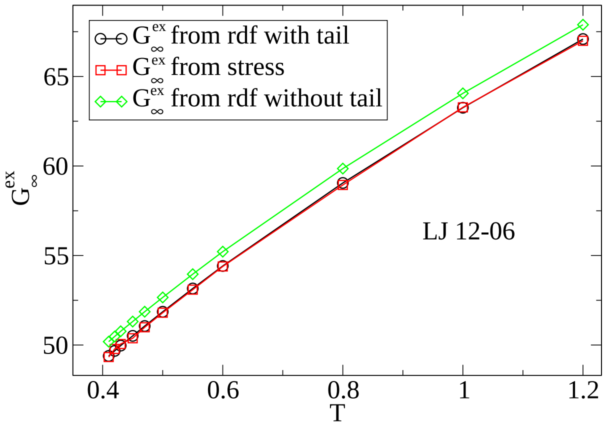

Figure 2.9: Check that G^{ex}_{∞} computed in two different ways give approximate the same value on an isochore $\rho = 1.2$. The relative difference for G^{ex}_{∞} from the autocorrelation function and the integral without the tail correction is around 2% for all the state points. Including the tail correction makes the two curves collapse as they should.

Figure 2.9 show the difference between calculating the integral in equation (2.17) with and without the tail correction. It is seen that including the tail correction is consistent with the $G^{ex}(0)$ calculated from the stress auto correlation function. All the reported G^{ex}_{∞}'s has been calculated including the tail or directly from the auto correlation.

2.2.6 G_∞ from plateau or zero time?

Recently Dyre and Wang [Dyre 2012] and Puosi and Leporini [Puosi 2012] discussed the difference between the plateau value of the transient elastic modulus and the zero time elastic modulus, the same as calculated from the radial distribution function. Both concluding that the plateau value is the right quantity for the instantaneous shear modulus. The truly instantaneous shear modulus is much faster than the phonon times and therefore not the right quantity for the elastic models. Experimentally it is not possible to measure the real instantaneous value because the cross over from the affine zero time G_∞ to the relaxed G_∞ plateau value is in the range of THz – not accessible to experimentalists. Typically the highest obtainable frequency is in the GHz or MHz range.

The existence of a two step relaxation, this feature is seen many places in viscous liquids where the first relaxation is attributed vibrations of the particles in their cage while the second relaxation is attributed structural (α) relaxation of the liquid.

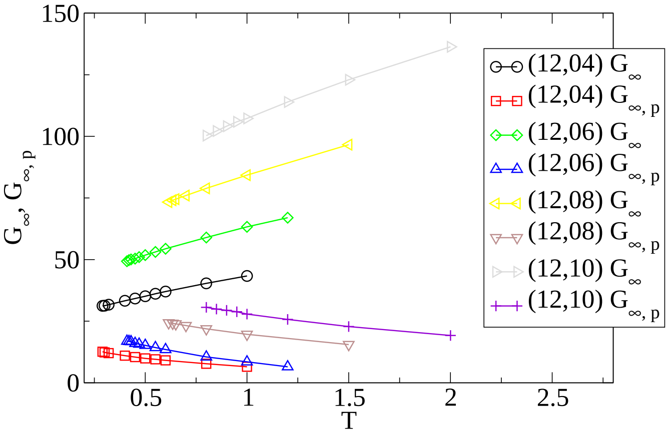

Figure 2.10: The temperature dependence of the infinite and plateau shear modulus on an isochore ($\rho = 1.2$) for all the potentials. The infinite shear modulus is increasing when increasing temperature, whereas the plateau value is decreasing with increasing temperature.

As seen on figure 2.10 the $t = 0$ infinite frequency and the plateau value is increasing and decreasing respectively with increasing temperature, consistent with [Yoshino 2010] who did the same calculation for a soft sphere system. The decreasing behavior makes the plateau value a candidate for the Shoving model [Dyre 2012]. See section 2.3 for investigation of this question.

2.2.7 Results for Isomorphs and Isochores

The invariance of the stress autocorrelation function in reduced units should according to the theory be true for isomorphs where it should fail for isochores and isotherms. This is, to a good approximation, also the case as seen in figure 2.11 where the isomorphs is seen to collapse on one master curve. The autocorrelation function changes its shape on an isochore as a function of temperature. The plateau value increases and becomes more stretched. The autocorrelation function is calculated in two different ways. One where the output from the simulation is sampled logarithmic and the autocorrelation is calculated by brute force. This method resolves the short time behavior well, but is heavy due to the vast amount of data that are saved. Another method takes advantage of the Wiener–Khinchin theorem [Wiener 1930, Khinchin 1934] and Fourier transforms the data, calculates the power spectrum and transform them back. The two methods gives the same results, but the statistic for the plateau value is better if the method where the stress is Fourier transformed forth and back is used. Unfortunately this method does not resolve the short time behavior because linear saving is needed to transform the data. The other way of calculating the shear modulus has been inserted for completeness at selected temperatures. For all state points, 10 independent simulations with different initial configurations was run and for each simulation, the three off diagonal elements was averaged, resulting in an average of 30 points for each point displayed for the transient elastic modulus.

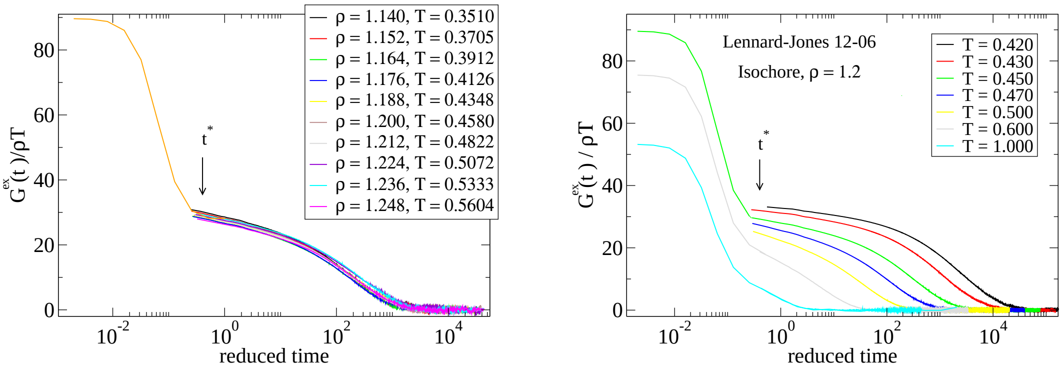

Figure 2.11: Left: Isomorph. Right: Isochore $\rho = 1.2$. The autocorrelation function is invariant on an isomorph when expressed in reduced units.

Extracting the G_∞^{ex} for the isomorphs and isochores on the examined potentials shows that the plateau values are invariant on isomorphs and not on isochores.

2.2.8 Predicting G_∞^{ex} on isochores

Rosenfeld and Tarazona [Rosenfeld 1998] derived from density functional theory an expression for the potential energy on an isochore:

$$U(T) = U_0 + \alpha T^{3/5} \tag{2.18}$$

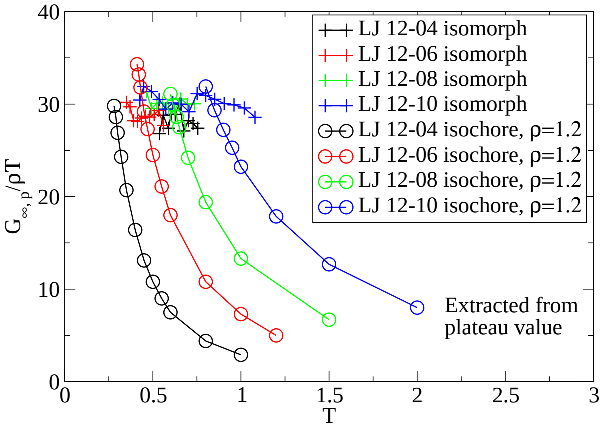

Figure 2.12: Invariance of the plateau value on the isomorphs and variations on the isochores. From this figure it is concluded that the plateau value is invariant on isomorphs and not on isochores.

with the somewhat strange temperature dependence with an exponent of $3/5$.

Because the potential energy and virial can be computed as an integral over the radial distribution function $g(r)$ [Hansen 1986] it is possible to express the excess shear modulus as a linear combination of the potential energy (per particle) and the virial (per particle). The potential and virial energy per particle is

$$\begin{aligned}\frac{U}{N} &= 2\pi\rho\int_0^\infty g(r)r^2v(r)\mathrm{d}r\\ \frac{W}{N} &= \frac{2}{3}\pi\rho\int_0^\infty g(r)r^3\frac{\mathrm{d}v(r)}{\mathrm{d}r}\mathrm{d}r\end{aligned} \tag{2.19}$$

which means we can write

$$G_\infty^{ex} = C_1\frac{W}{N}\rho + C_2\frac{U}{N}\rho \tag{2.20}$$

C_1 and C_2 are constants depending on the potential. The constants C_1 and C_2 are found by equating the integrands in eq. (2.20)

$$\frac{\mathrm{d}}{\mathrm{d}r}\left(r^4\frac{\mathrm{d}\phi(r)}{\mathrm{d}r}\right) = C_1r^2\phi(r) + C_2r^3\frac{\mathrm{d}\phi(r)}{\mathrm{d}r} \tag{2.21}$$

Let the interaction potential be: $\phi(r) = \mathfrak{a}r^{-m} - \mathfrak{b}r^{-n}$ with $\mathfrak{a}$ and $\mathfrak{b}$ as constants (that can depend on n and m). We recognize this as two coupled equations in r^{-m+2} and r^{-n+2} with two unknowns C_1 and C_2:

$$\begin{aligned}\mathfrak{a}m(m-3)r^{-m+2} &= C_1\mathfrak{a}r^{-m+2} - mC_2\mathfrak{a}r^{-m+2}\\ \mathfrak{b}n(n-3)r^{-n+2} &= C_1\mathfrak{b}r^{-n+2} - nC_2\mathfrak{b}r^{-n+2}\end{aligned} \tag{2.22}$$

dividing with: r^{-m+2}, r^{-n+2}, $\mathfrak{a}$ and $\mathfrak{b}$ in their respective equations and solving for C_1 and C_2, we find:

$$\begin{aligned} C_1 &= \frac{mn[n(n-3)+m(m-3)]}{m-n} \\ C_2 &= \frac{n(n-3)+m(m-3)}{m-n}\,. \end{aligned} \tag{2.23}$$

Combining Rosenfeld–Tarazona scaling $U = U_0 + \alpha T^{3/5}$ with a result for strongly correlating liquids $W = W_0 + \gamma U$ [Bailey 2008b] allow us to insert these expressions for U and W in eq. (2.20) and we find:

$$G_\infty = aT^{3/5} + b\,. \tag{2.24}$$

The constants a and b are then found to be $a = \alpha(C_1\gamma + C_2)$ and $b = C_1(W_0 + \gamma U_0) + C_2U_0$. The linear relation between G_∞ and $T^{3/5}$ is tested for the four glass forming systems on isochores with density $\rho = 1.20$. As can be seen in figure 2.13 this relationship is fulfilled very well. Calculating the constants a and b from the four isochores by calculating α, γ, U_0 and W_0 gives good agreement with the actual values and are plotted as straight lines. The results can be seen in figure 2.13.

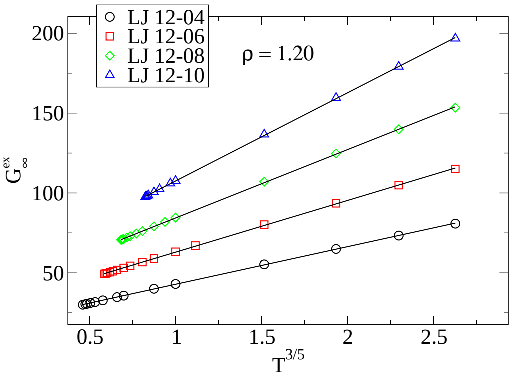

Figure 2.13: Testing the linear relation between the instantaneous shear modulus and $T^{3/5}$. The solid black lines are not fits, but found from U and W data by calculating γ, α, U_0 and W_0. It is seen to follow this prediction for a large temperature range.

2.3 Testing the shoving model

The Shoving model explain the non–Arrhenius dependence on temperature of the structural (α) relaxation time τ. It predicts

$$\tau_\alpha(T) = \tau_0 \exp\left(\frac{G_{\infty,p}(T)V_c}{k_B T}\right) \tag{2.25}$$

where the characteristic volume V_c is independent of temperature. Structure changes very little when a liquid approaches the glass transition temperature. Plotting $G_{\infty,p}(T)/T$, where the subscript p indicates that it is the plateau value (including the ideal $\rho k_B T$ term) against relaxation time should then result in a straight line. Results of simulations of four isochores, one for each different system is shown in figure 2.14.

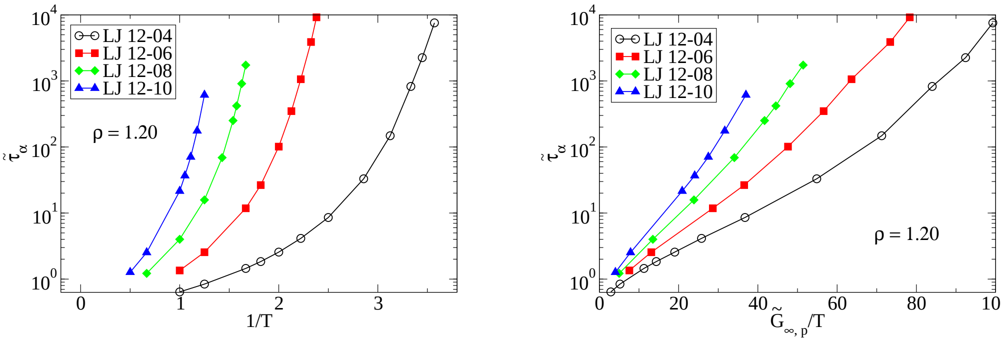

Figure 2.14: Left: An Arrhenius plot: Structural relaxation time in reduced units versus inverse temperature. Right: Testing the Shoving model for four isochores. The instantaneous shear modulus is seen to be responsible for most of the non Arrhenius behavior. The deviation from a straight line is not big. The LJ 12-4 potential does not have filled symbols to emphasize it has negative pressure and the physics is different. See figure 2.2.

Figure 2.14 shows the reduced relaxation time plotted against $\tilde{G}_{\infty,p}/T$ also in reduced units and including the ideal $\rho k_B T$ term (right) and $1/T$ (left). The reduced relaxation time $\tilde{\tau}_\alpha$ is defined as where the incoherent part of the self intermediate scattering function for the large A particles has decayed to e^{-1}, see figures 2.3 and 2.4 from where the relaxation times has been extracted.

Since we are dealing with four different systems with four different temperature scales, we scale the temperatures with a system dependent factor T_n in order to compare data to the standard 12-6 LJ potential. This is done in the left side of figure 2.15 where it is seen that the curves to a good approximation collapse onto the 12-6 potential. The 12-4 potential is seen to deviate significantly, we attribute this deviation to the negative pressure. The fastest state points for the other systems are deviating little for the fastest relaxations. It can be difficult to define a plateau value at these fast relaxations as seen in figures 2.3 and 2.4.

Right side of figure 2.15 is the main result for this section. It shows that the non Arrhenius behavior of relaxation time can, to a good approximation, be described by the plateau value of the instantaneous shear modulus. The scaling is done by using the temperature dependent factor T_n from the Arrhenius plot and multiply it with a system dependent volume V_n. There is no temperature dependence in this characteristic volume $V_n = \text{constant}$, it is simply an overall factor close to one reflecting that the characteristic volume is different for every system. The V_n scaling factor is seen to follow the volume of the first peak in the radial distribution function (the cage). Figure 2.23 display the radial distribution function for the exact same relaxation time and it is seen that they are very similar, but: $V_{c,12-10} > V_{c,12-8} > V_{c,12-6} > V_{c,12-4}$, with subscript c referring to the cage = Volume of the first peak in the radial distribution function, consistent with our V_n's decreasing with increasing n. Again the 12-4 potential sticks out, probably due to the negative pressure.

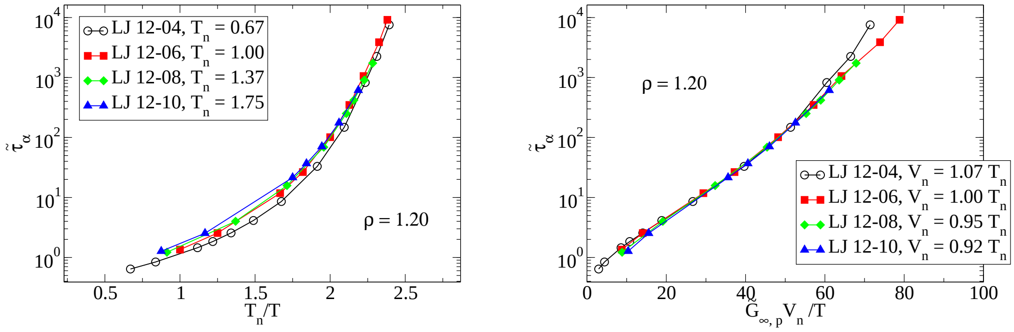

Figure 2.15: Left: An Arrhenius plot. Relaxation time versus T_n/T. The temperatures has been scaled with T_n, as indicated in the legend, to compare with the 12-6 potential. Right: Testing the Shoving model for four isochores. The scaling factor V_n is decreasing with increasing n, consistent with the increasing volume of the first peak in the radial distribution function with increasing n. See text for discussion. The LJ 12-4 potential does not have filled symbols to emphasize it has negative pressure and the physics is different. See figure 2.2.

2.4 Comparing fitting functions

The purpose of this section is to compare two different fitting functions with different physical interpretations. We first give a short introduction to these functions and fit them to the transient elastic modulus for the 12-6 LJ potential. There is practically no difference for these functions, so we perform the same procedure for the self part of the incoherent intermediate scattering function, where we have better statistics. Here we observe a small difference in the tail, but there is not drawn any decisive conclusions, except that it should be investigated in more detail.

There exist several different functions describing the evolution of correlation functions.

One of them is suggested by Niels Boye Olsen:

$$f_B(t) = a\exp\left(-\frac{t}{\tau} - k\left(\frac{t}{\tau}\right)^{1/2}\right) \tag{2.26}$$

and is physically fundamentally different from the widely used Kohlrausch [Kohlrausch 1854] or stretched exponential fitting function:

$$f_K(t) = b\exp\left(-\left(\frac{t}{\tau}\right)^{\beta}\right)\,. \tag{2.27}$$

The difference lie in the long time behavior of the relaxation rate of the functions. Differentiating $f_B(t)$ and $f_K(t)$ we see that the stretched exponential has vanishing relaxation rate:

$$\lim_{t\to\infty}\left(\frac{\mathrm{d}\log f_K}{\mathrm{d}t}\right) \propto \lim_{t\to\infty}\left(\frac{t}{\tau}\right)^{\beta-1} = 0\,, \qquad \text{for } \beta < 1\,. \tag{2.28}$$

Meaning that the relaxation becomes slower and slower and never reaches equilibrium. The long time behavior for the Boye fitting function is not vanishing, but finite:

$$\lim_{t\to\infty}\left(\frac{\mathrm{d}\log f_B}{\mathrm{d}t}\right) \propto \lim_{t\to\infty}\left(\frac{1}{\tau} + \frac{1}{2}\left(\frac{t}{\tau}\right)^{-1/2}\right) = \frac{1}{\tau}\,, \tag{2.29}$$

due to the linear term in the argument of the exponential function. Unlike the stretched exponential, this function relaxes at a finite rate for long times and will eventually reach equilibrium if you are patient enough.

The fitting has been performed in xmgrace. The performance of each fit is quantified by the correlation coefficient defined as

$$r = \sqrt{1 - \frac{SSE}{SST}} \tag{2.30}$$

with SSE equal to the Sum of Squared Errors and SST equal to the Sum of Squared Totals. Denoting the error by $f(t) - f_{fit}(t)$ the SSE and SST are

$$\begin{aligned} SSE &= \sum_i^N \left(f(i) - f_{fit}(i)\right)^2 \\ SST &= \sum_i^N \left(f(i)\right)^2\,. \end{aligned} \tag{2.31}$$

Time t is discretized in i with N being the total number of points in the data set.

2.4.1 Fitting shear data

In this section we test the two different fitting functions on the transient elastic modulus for the 12-6 LJ potential.

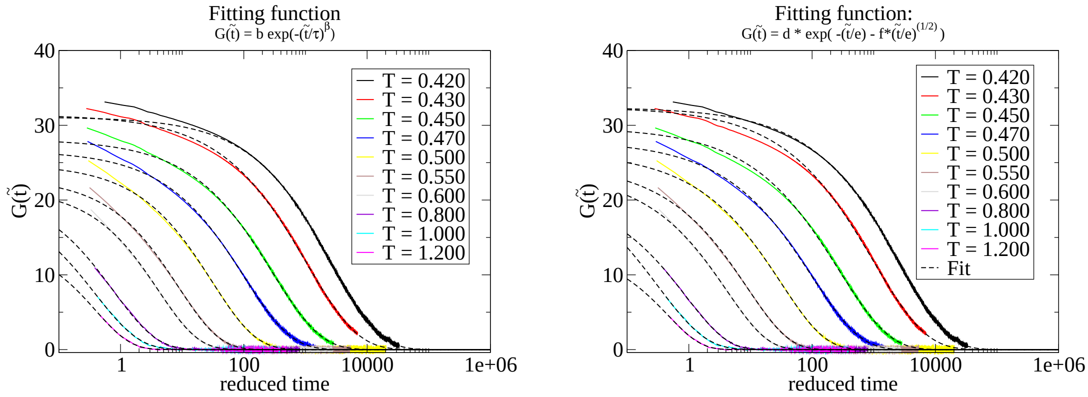

Figure 2.16: Fitting. Left is the stretched exponential and right is the Boye function. The broken lines are fits to the data. There is no qualitative difference between the two fitting functions.

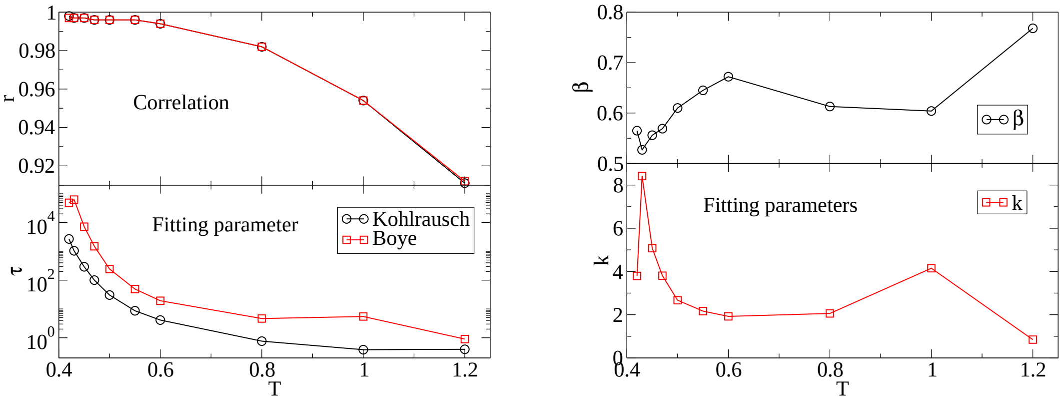

Figure 2.17: Correlation of fit and fitting parameters. Left is the relaxation time and correlation as function of temperature. Right is the exponent β and k from the fitting functions. There is no quantitative difference between the two fitting functions.

On figure 2.16 and 2.17 we see that the correlation is practically the same for both fitting functions. Figure 2.16 show the actual data together with the fitted functions. Left is the Boye function and right is the stretched exponential. The fitting parameters from equation (2.26) and (2.27) can be seen in figure 2.17. These parameters are expected to behave monotonically and it is clear from figure 2.17 that it is not the case for either fitting functions. The stretching parameter β are seen to decrease from $\sim$0.75 to $\sim$0.52 at low temperature. k is increasing with decreasing temperature. In experiments the value of k is between 2 and 3 (personal communication with Niels Boye Olsen), fairly consistent with our findings. These two fitting functions have the same number of fitting parameters and can thus be compared. Despite the hard work to achieve good statistics on these data, it is not the easiest quantity to compute. An attempt to investigate the long time behavior of the fitted functions and compare them to data was was made, but unsuccesfull. We have better statistics on the self part of the incoherent Intermediate Scattering Function (ISF) which we will fit to in the next subsection.

2.4.2 Fitting the self part of the incoherent intermediate scattering function $F_s(q,t)$

The self part of the incoherent intermediate scattering function $F_s(q,t)$ is defined as [Hansen 1986]:

$$F_s(q,t) = \frac{1}{N}\sum_{j=1}^{N}\Big\langle \exp\Big(- i\mathbf{q}\cdot[\mathbf{r}_j(t) - \mathbf{r}_j(0)]\Big)\Big\rangle \tag{2.32}$$

with N being the number of particles, $\mathbf{q}$ being the scattering wave vector and $\mathbf{r}_j(t) - \mathbf{r}_j(0)$ as the displacement for the j'th particle and angled brackets denote time and ensemble average. We choose the wave vector $q = 7.25$, close to the wave vector corresponding to the first peak in the structure factor. We fit to all the systems, but only display the 12-6 results. The data for the 12-8 and 12-10 are very similar, as seen in 2.21 where the fitting parameters are displayed. The 12-4 potential deviates significantly due to the negative pressure and will not be included here. The q vector for the other systems are slightly different, but are chosen so it also corresponds to the first peak in the structure factor.

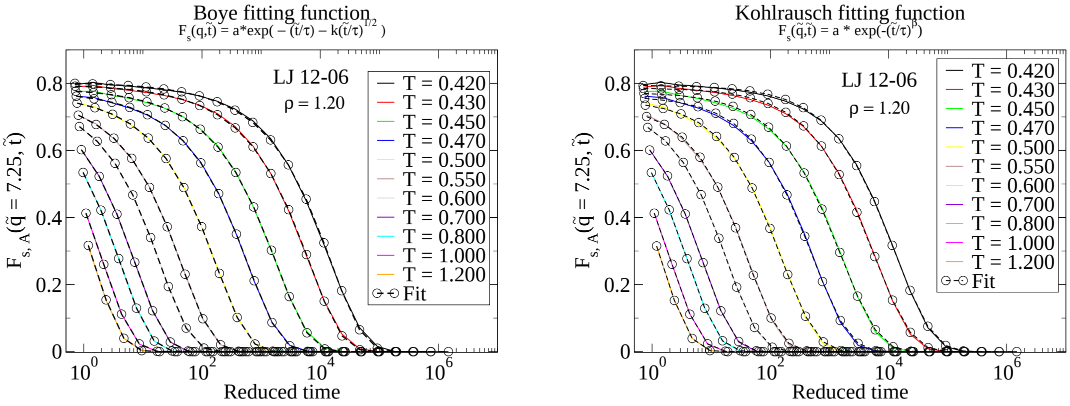

Figure 2.18: Left: Boye fitting function. Right: Kohlrausch fitting function. Showing the $F_s(q = 7.25, t)$ in reduced units (for the A particles) and the respective fits for the 12-6 LJ potential. Axes are $(\log, \text{lin})$. There does not seem to be any difference between the two functions. The correlation for all fits is above 99% and can be seen in figure 2.19. Fitting parameters can be seen in section 2.5.

By visulation inspection of figure 2.18, there is no qualitative difference between the two fitting functions, but quantitative there is. Computing the correlation r it is clear from figure 2.19 that the Boye fitting function is slightly better. This is apparent in the way it decays to zero and by zooming in at the tail and changing axes from (log,lin) to (lin,log) it is seen how the data and fitting functions relax to zero. As seen in figure 2.20 there is a visual difference when we focus on the tail.

Plotting the intermediate scattering function and the two fits in the same figure makes it possible to compare them directly. In the following figures, we include two temperatures

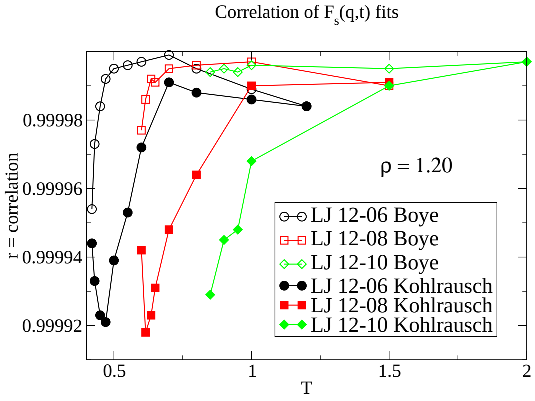

Figure 2.19: Correlation of fits. The fitting function suggested by Boye is slightly better than the stretched exponential. The high correlation for both functions is due to the relatively small number of points for the $F_{s,A}(q,t)$.

and look at how they decay to zero. In these figures, it can be seen that the statistics becomes too poor at values $F_{s,A}(q,t) \sim 10^{-3}$. The data fluctuates around 0 and some of the points are negative. From these figures it is seen that the Boye fitting function (circles in figure 2.20) follow the data better than the stretched exponential. The stretched exponential "bends off" at longer times where the Boye function follow the data in a linear way, until it has decayed to $\sim 10^{-3}$. Whether or not this is close enough to zero can be discussed, better statistics is always welcome. Remember these $F_s(q,t)$ are averaged over 10 independent runs, where all simulations have been running $\sim 100\tau_\alpha$. All temperatures show this tendency except the $T = 0.43$ $F_s(q,t)$ for unknown reasons. We are working on methods to achieve better statistic.

These findings are first indications that the long time behavior of relaxation functions have a finite relaxation rate. This is consistent with experimental findings for relaxation of the intermediate scattering function (personal communication with Niels Boye Olsen). More simulations with better statistics are required to determine this issue. Obviously it is more convincing to plot the rate itself, but the statistical errors increase dramatically when data is differentiated.

2.5 Quasi universality for generalized Lennard–Jones systems

The collapse of the relaxation times (see figure 2.15) for the systems investigated indicates there exist some sort of universality for the generalized Lennard–Jones systems. In this subsection we look at the structure and functional form of the self part of the incoherent intermediate scattering function to pursue the idea of quasi universality.

By plotting the fitting parameters for both fitting functions of the $F_s(q,t)$ we see that these parameters are very similar indicating some sort of quasi universality [Dyre 2013].

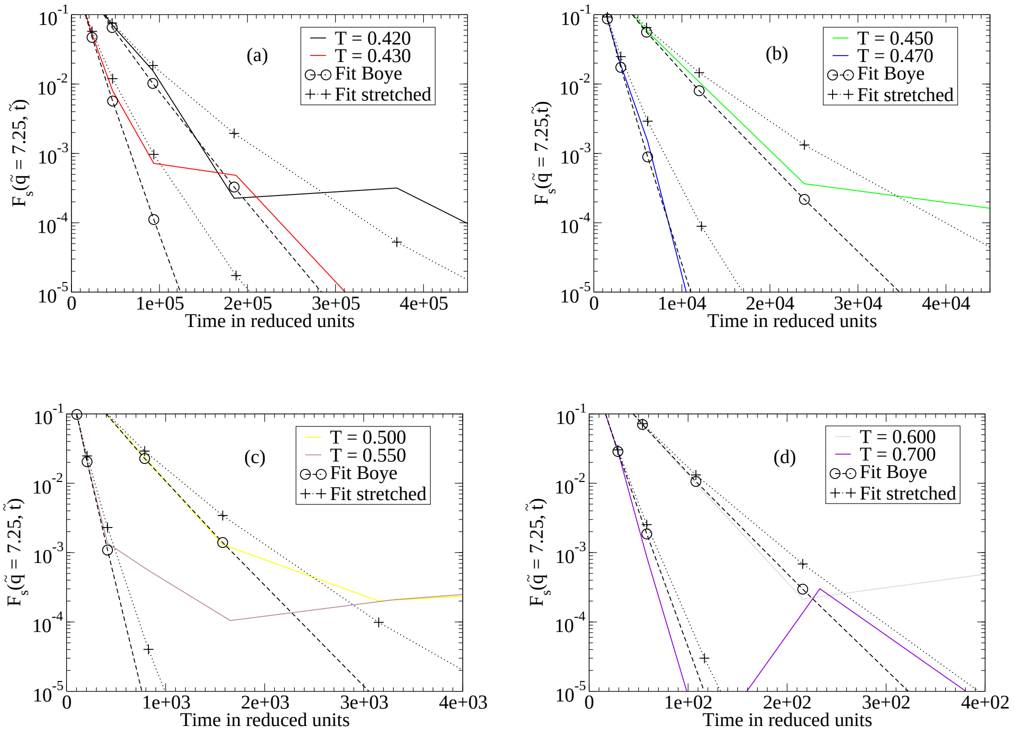

Figure 2.20: Tail of the $F_s(q,t)$ in reduced units for the 12-6 LJ potential at the 8 lowest temperatures together with the stretched exponential and Boye fits. The solid lines are $F_s(q,t)$ data and the broken lines are Boyes fitting function with circles. Dotted lines with plusses are the stretched exponential fit. We have shifted to logarithmic y-axis from 10^{-1} to 10^{-5} and linear time axis in order to zoom in on the tail. (a) is the lowest temperatures with longest time up to $4.5 \cdot 10^5$, (b) has times up to $4.5 \cdot 10^4$, (c) has times up to $4 \cdot 10^3$ and (d) has times up to $4 \cdot 10^2$, thereby going one decade down for every window.

Due to the negative pressure for the 12-4 potential, we will exclude this system for the discussion and in the plots.

Figure 2.21 show the fitting parameters for the 12-6, 12-8 and 12-10 LJ potentials. All these fits are more than 99 % correlated. Indicating that these parameters describe the actual data well. Left is the stretched exponential β and τ parameters plotted and right is k and τ for Boyes fit plotted. It is seen that both set of fitting parameters are almost falling on a master curve. For unknown reasons is the second fastest state point for the 12-10 potential deviating significantly from the master curves.

The invariance of structure is probed at one state point for all the systems with the same relaxation time. The $F_s(q,t)$ in reduced units for these four state points are shown in figure 2.22 and are seen to be very similar in shape as expected from figure 2.21. There seem to be a small difference in the slope. We look into this by computing the diffusion coefficient for all state points and compare them in section 2.5.1.

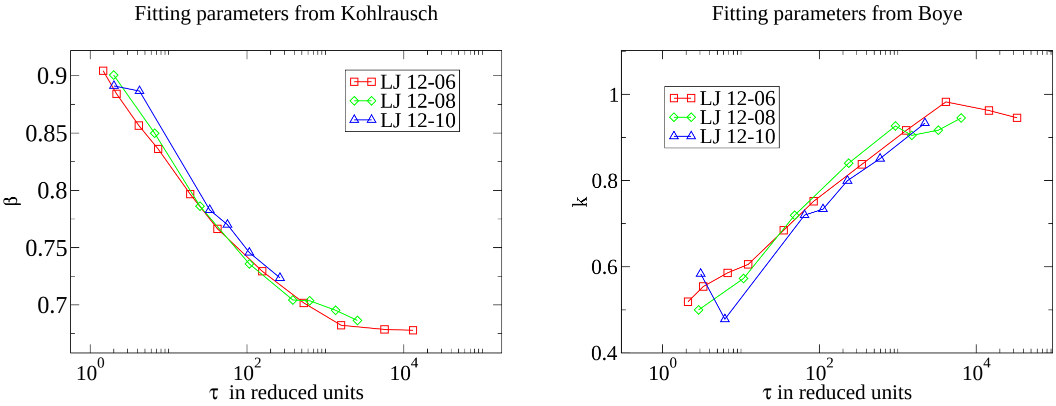

Figure 2.21: Fitting parameters extracted from fits to the $F_s(q, t)$ in reduced units for the three potentials with positive pressure on the isochore $\rho = 1.20$. Left is the stretching parameter β as a function of the reduced relaxation time from eq. (2.27). Right is the k parameter plotted against the reduced relaxation time from eq. (2.26). The relaxation times are also fitting parameters from the respective function.

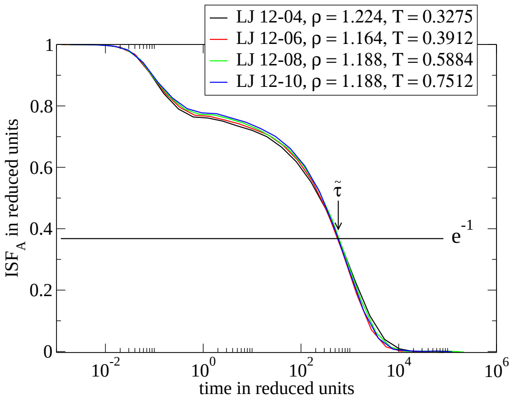

Figure 2.22: Self part of the incoherent Intermediate Scattering Function for four different potentials at same relaxation time. Displayed is the big A particles and the horizontal line indicates when it has decayed to exp(−1).

The structure for these state points are shown in figure 2.23 where all the radial distribution functions are displayed.

It is seen that the structure for all the distribution functions are more or less invariant when going from one system to another system. There seem to be small deviations in the top of the first peak for the big AA particles. The 12-10 potential is higher implying that the volume of the first peak for this system is larger and so on: $V_{c,12-10} > V_{c,12-8} > V_{c,12-6} > V_{c,12-4}$ with V_c indicating the volume of the first peak. There seem to be small differences for the AB and BB radial distributions as well, they are not significant and it is concluded that there exist quasi universality for KABLJ generalized Lennard-Jones

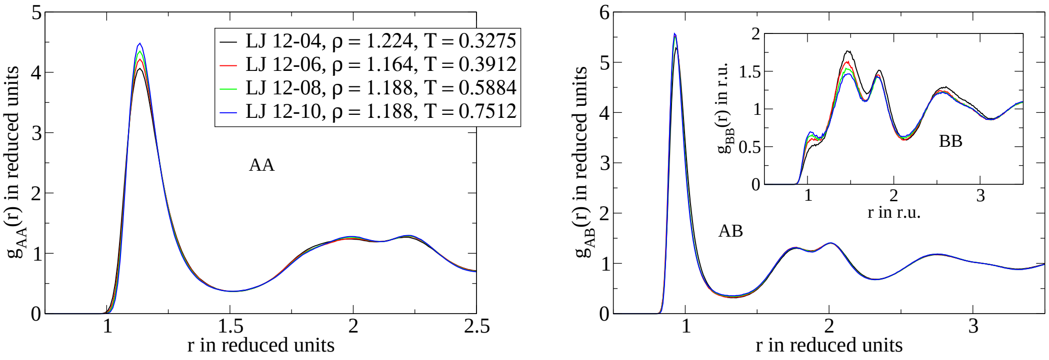

Figure 2.23: The radial distribution functions. Left: the AA distribution functions are shown. Right: AB and BB

potentials.

2.5.1 Comparing dynamics with soft spheres

Soft spheres are purely repulsive Inverse Power Law potentials with a correlation coefficient $= 100\%$:

$$\phi(r) = \varepsilon \left(\frac{\sigma}{r} \right)^n \tag{2.33}$$

and have been studied extensively, among others De Michele et al. [Michele 2004]. Instead of looking at the relaxation time we calculate the diffusion coefficient in reduced units and obtain a similar plot as De Michele et al. [Michele 2004]. They studied the purely repulsive IPL (soft spheres) with different exponents $n = \{6, 8, 12, 18\}$ on the binary Kob–Andersen mixture and showed that they all collapsed to a master curve. This means that there exist quasi universality inside the Kob - Andersen Binary IPL (KABIPL) systems. Here we investigate whether or not there exist quasi universality between the KABIPL and KABLJ systems. Figure 2.24 show the diffusion coefficients for the KABLJ systems. Left is unscaled and right is a scaled version where the temperatures for the 12 -4, -8 and -10 potentials have been scaled to collapse the 12-6 potential. The temperature scaling factor T_n is the one we found when scaling the relaxation times in section 2.3.

Fitting the different systems except the 12-4 to the VFT [Vogel 1921, Fulcher 1925, Tamman 1926] fitting function, it is possible to compare them to the soft sphere pendant from [Michele 2004] because they fit all their data to the VFT and find a good collapse with the VFT describing the data well. Figure 2.25 show all the data points together with the VFT fitted to KABLJ and KABIPL. The VFT fitting function is defined as:

$$D(T/T_n) = a \exp \left(\frac{b}{T/T_n - c} \right) . \tag{2.34}$$

The VFT fitting function describes the data quite well in figure 2.25 the fit is performed for viscous state points $T/T_n < 0.78$. It is seen that the VFT from KABIPL seem to be better for viscous state points and worse for faster diffusion coefficients. However, by

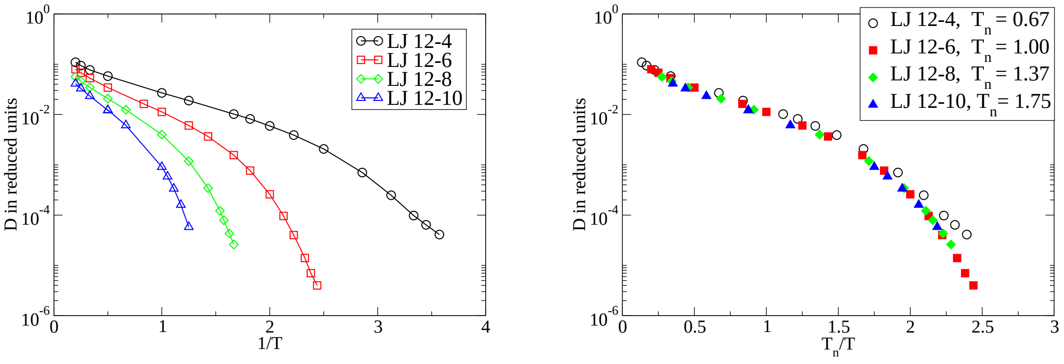

Figure 2.24: Diffusion coefficients in reduced units for the different potentials. Left the unscaled version. Right: The inverse temperature axis scaled by an n dependent temperature T_n extracted from figure 2.15. The 12-4 potential is seen to deviate for slow diffusion coefficient where the pressure is negative.

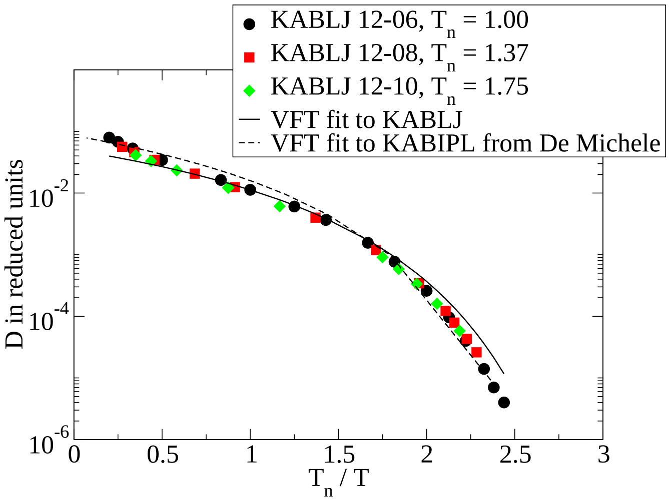

Figure 2.25: Solid black line is the Vogel–Fulcher–Tamman VFT equation $D(x) = a * \exp[b/(x - c)]$, with $x = T/T_n$. The fit is performed for viscous state points, in this case $x < 0.78$. The fitting parameters are $a = 0.0532$, $b = -1.17$ and $c = 0.277$. Broken line is the Soft Sphere (SS) De Michele VFT fitting function with all temperatures scaled by 1.39: $(T = 1.39 * T_{SS})$.

changing the region where the fit is performed we can mimic the fast or slow diffusion. Here the region $T/T_n < 0.78$ was chosen to give a good overall fit.

From figure 2.25 it is concluded that the dynamics for the KABIPL and the KABLJ inherit quasi universality.

2.6 Generalized Lennard-Jones conclusions

The generalized Lennard-Jones systems are all strongly correlating in most part of the phase diagram and therefore they have isomorphs. The excess infinite frequency shear modulus G_{∞}^{ex} and the bulk $K_{\infty}^{ex} - K_0$ was, to a good approximation, found to be invariant. A prediction for the temperature dependence on isochores for $G_{\infty}^{ex} \propto T^{3/5}$ was tested and verified. The isomorph invariance for the plateau value of the transient elastic modulus $G_{\infty,p}^{ex}$ was found to be better than the truly instantaneous G_{∞}^{ex}. The plateau value of the transient elastic modulus $G_{\infty,p}^{ex}$ enters the Shoving model and it was found that it can explain most of the non Arrhenius dependence of the KABLJ systems. We tested two fitting functions and found indications that the relaxation rate for the incoherent intermediate scattering function $F_{s,A}(q,t)$ is finite opposite to the widely used stretched exponential. Quasi universality in the generalized Kob Andersen Binary Lennard Jones (KABLJ) systems was established and we find the dynamics (diffusion coefficient) between the KABLJ and the generalized Kob Andersen Binary Inverse Power Law systems belonging to the same quasi universality class.

CHAPTER 3

Generic density scaling

We derive a generic form of density scaling $h(\rho)$ (the long density jump formula), enabling us to explore big parts of the phase diagram, with unrealistic high pressures and densities. For systems interacting via a sum of Inverse Power Law (IPL) potentials: $v(r) = \sum_n \varepsilon_n r^{-n}$, the scaling function $h(\rho)$ is found analytically. The rest of the chapter are devoted testing this form of scaling. First we use the standard Kob Andersen Binary Lennard Jones ($n = 12, 6$). At viscous state points, dynamics is highly sensitive to small temperature changes and the slightest uncertainty in the density scaling exponent γ entering $h(\rho)$ leads to unsatisfactory scaling of dynamics. We explore different ways of determining γ. Using the density scaling function $h(\rho)$, we generate isomorphs for liquids interacting with three IPL terms in the potential on the binary Kob Andersen system. In section 3.4 we present a new interpretation of the role of attractive versus repulsive forces.

3.1 Derivation of *the long density jump formula*

The long density jump formula gives us the relation between different state points with density and temperature (ρ, T) and state points isomorphic to these. Power law density scaling is a special case of this more general form of scaling. The density scaling exponent is defined:

$$\gamma = \left.\frac{\mathrm{d}\ln T}{\mathrm{d}\ln \rho}\right|_{S_{ex}} . \tag{3.1}$$

If γ is constant it is shown in equation (1.12) that integrating this equation leads to power law density scaling:

$$\frac{\rho^\gamma}{T} = const\,. \tag{3.2}$$

In the previous chapter we have seen that this form of scaling works well if density is changed $\sim 1\%$, but we did not see that if density was changed $\sim 5\%$, between a neighboring state point, the scaling became poor due to the density dependence on γ. The power law density scaling implies that the reduced relaxation time can be written:

$$\tilde{\tau} = F\left(\frac{\rho^\gamma}{T}\right) . \tag{3.3}$$

With F being a generic function. This form of density scaling was first suggested by [Tolle 2001] based on experimental studies on a strongly correlating liquid (OTP).

Our starting point for the general density scaling is the definition of two isomorphic state points. **First:** that pairs of scaled micro configurations have proportional canonical

Boltzmann factors. Denoting state point (1) with potential energy, density and temperature: $U_1 = U\left(\mathbf{r}_1^{(1)}, ..., \mathbf{r}_N^{(1)}\right)$, ρ_1 and T_1 and state point (2) with: $U_2 = U\left(\mathbf{r}_1^{(2)}, ..., \mathbf{r}_N^{(2)}\right)$, ρ_2 and T_2. **Second:** that the reduced coordinates must (trivially) scale onto each other $\rho_1^{1/3}\mathbf{r}_i^{(1)} = \rho_2^{1/3}\mathbf{r}_i^{(2)}$. The definition of proportional Boltzmann factors is:

$$\exp\left(-\frac{U_1}{k_B T_1}\right) = C_{12}\exp\left(-\frac{U_2}{k_B T_2}\right) . \tag{3.4}$$

Where C_{12} being the same proportionality constant for all micro configurations. We exploit the direct isomorph check [Gnan 2009] that directly test the proportionality between the Boltzmann factors. By taking the logarithm of eq. (3.4) and expressing coordinates in reduced units we find:

$$\frac{U\big(\rho_2^{-1/3}(\mathbf{r}_1^{(2)}, ..., \mathbf{r}_N^{(2)})\big)}{U\big(\rho_1^{-1/3}(\mathbf{r}_1^{(1)}, ..., \mathbf{r}_N^{(1)})\big)} = \frac{T_2}{T_1} + K_{12} \tag{3.5}$$

with K_{12} being a constant only dependent on state point (1) and (2), but the same for all micro configurations. We perform the direct isomorph check by simulating a time sequence at one state point (1) and save the micro configuration every Δt time step. From all these micro configurations at different times, we calculate the scaled potential energies at state point (1): $U\big(\rho_1^{-1/3}(\mathbf{r}_1^{(1)}, ..., \mathbf{r}_N^{(1)})\big)$ and (2): $U\big(\rho_2^{-1/3}(\mathbf{r}_1^{(2)}, ..., \mathbf{r}_N^{(2)})\big)$. The scaled potential energies are plotted against each other in a scatter plot, like the one in figure 1.1, and if there exist an isomorphic temperature at state point (2), it is found by calculating the linear regression slope. A schematic drawing can be seen in figure 3.1. This only works if the system is strongly correlating and the slope is well defined.

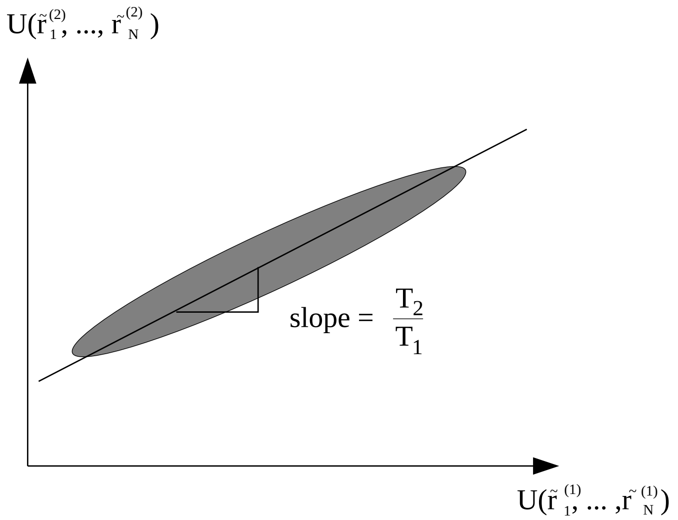

Figure 3.1: Sketch of the direct isomorph check. A simulation is performed at state point (1) with density and temperature (ρ_1, T_1). An ensemble of micro configurations from state point (1) is plotted as scaled potential energies: $U_1 = U\big(\tilde{\mathbf{r}}_1^{(1)}, ..., \tilde{\mathbf{r}}_N^{(1)}\big)$ vs $U_2 = U\big(\tilde{\mathbf{r}}_1^{(1)}, ..., \tilde{\mathbf{r}}_N^{(1)}\big)$. The slope is found by linear regression and is the ratio of the two temperatures: $\langle \Delta U_2 \Delta U_1\rangle / \langle (\Delta U_1)^2\rangle = T_2/T_1$. See text for a thorough explanation.

The generic density scaling function $h(\tilde{\rho})$, with $\tilde{\rho}$ being the ratio of the densities $\tilde{\rho} = \rho_2/\rho_1$, is found as the linear regression slope in this plot:

$$h(\tilde{\rho}) = \frac{T_2}{T_1} = \frac{\langle \Delta U_2 \Delta U_1 \rangle}{\langle (\Delta U_1)^2 \rangle} \, . \tag{3.6}$$

As usual denotes angled brackets ensemble averages and Δ is the fluctuation away from mean.

We now turn to the class of systems interacting via a sum of inverse power laws. The pair interaction potential is defined as

$$v(r_{ij}) = \sum_n \varepsilon_n \left(\frac{\sigma_{ij}}{r_{ij}} \right)^n \, , \tag{3.7}$$

with n being the number of terms present in the potential. The potential energy of a single term n is:

$$U_n\big(\mathbf{r}_1, ..., \mathbf{r}_N\big) = \sum_{i>j} \varepsilon_n \left(\frac{\sigma_{ij}}{r_{ij}} \right)^n \, . \tag{3.8}$$

Switching to reduced units means replacing r with $\rho^{-1/3}\tilde{r}$, so the n'th term in scaled coordinates are

$$U_n\big(\tilde{\mathbf{r}}_1, ..., \tilde{\mathbf{r}}_N\big) = \rho^{n/3} \sum_{i>j} \varepsilon_n \left(\frac{\sigma_{ij}}{\tilde{r}_{ij}} \right)^n \tag{3.9}$$

and because $U_1\big(\tilde{\mathbf{r}}_1^{(1)}, ..., \tilde{\mathbf{r}}_N^{(1)}\big) = U_2\big(\tilde{\mathbf{r}}_1^{(2)}, ..., \tilde{\mathbf{r}}_N^{(2)}\big)$ we can express the potential energy at state point (2) in terms of the potential energy at state point (1):

$$U_2 = \sum_n \tilde{\rho}^{\,n/3} U_{n,1} \, . \tag{3.10}$$

Inserting this in eq. (3.6) leads to an expression given in terms of the reduced density and potential energies at state point (1):

$$h(\tilde{\rho}) = \sum_n \tilde{\rho}^{n/3} \frac{\langle \Delta U_{n,1} \Delta U_1 \rangle}{\langle (\Delta U_1)^2 \rangle} \, . \tag{3.11}$$

This is our generic density scaling function. It can be rewritten in terms of heat capacities. Recall Einsteins fluctuation formula for the total heat capacity at constant volume is (the subscript 1 is discarded for notation clarity. It is implied that the quantities on the right hand side depends on the starting state point)

$$C_V = \left. \frac{\partial \langle U \rangle}{\partial T} \right|_V = \frac{\langle (\Delta U)^2 \rangle}{k_B T^2} \tag{3.12}$$

and the partial derivative with respect to temperature of observable A in the Boltzmann ensemble average:

$$\left. \frac{\partial \langle A \rangle}{\partial T} \right|_V = \frac{\langle \Delta A \Delta U \rangle}{k_B T^2} \, . \tag{3.13}$$

We recognize our generic density scaling function as a sum of weighted heat capacities:

$$h(\tilde{\rho}) = \sum_n \tilde{\rho}^{n/3} \frac{C_{V,n}}{C_V} \,. \tag{3.14}$$

Since $C_V = \sum_n C_{V,n}$, the number of constants: $C_{V,n}/C_V$ entering the density scaling function eq. (3.14) is $n-1$. For the single IPL potential we see that this has has power law density scaling ρ^γ/T with $\gamma = n/3$ and there is no parameter entering the scaling function. For the generalized LJ potential with two terms m and n as defined in equation 2.1, The partial potential energies U_m and U_n can be written as

$$U_m = \frac{3W - nU}{m-n} \qquad \text{and} \qquad U_n = \frac{-3W + mU}{m-n} \,, \tag{3.15}$$

where U and W is the total potential energy and virial, respectively. Inserting these expressions in eq. (3.11) and recognizing the density scaling exponent γ's fluctuation formula, we find:

$$h(\tilde{\rho}) = \rho^{m/3} \left(\frac{3\gamma - n}{m-n} \right) + \rho^{n/3} \left(\frac{-3\gamma + m}{m-n} \right) \,. \tag{3.16}$$

Especially for the standard 12-6 LJ it is:

$$h(\tilde{\rho}) = \tilde{\rho}^4(\gamma/2 - 1) + \tilde{\rho}^2(2 - \gamma/2) \,. \tag{3.17}$$

All this suggests the more general form of density scaling:

$$\tilde{\tau} = G\left(\frac{h(\tilde{\rho})}{T} \right) \,, \tag{3.18}$$

with $h(\tilde{\rho}) = \tilde{\rho}^{n/3}$ for systems interacting with a single IPL term. We are not the first suggesting this form of density scaling. [Alba-Simionesco 2002, Tarjus 2004, Alba-Simionesco 2004], are some of the density scaling pioneers. However, their considerations and arguments are very different than ours. They used the symbol $e(\rho)$, instead of $h(\rho)$ indicating that it is a form of activation energy function.

Changing notation by referring to the starting state point with subscript 0, our scaling function reads: $h(\tilde{\rho}) = T/T_0 \Rightarrow T = h(\tilde{\rho})T_0$. From our density scaling function and the definition of γ in eq. (3.1) we find the density dependence of γ by inserting T:

$$\gamma(\tilde{\rho}) = \frac{\mathrm{d}\ln T}{\mathrm{d}\ln \rho} = \frac{\mathrm{d}\ln[h(\tilde{\rho})T_0]}{\mathrm{d}\ln \rho} = \frac{\mathrm{d}\ln h(\tilde{\rho})}{\mathrm{d}\ln \rho} \,, \tag{3.19}$$

inserting our density scaling function for potentials interacting with sum of IPL terms, we arrive at:

$$\gamma(\tilde{\rho}) = \frac{\mathrm{d}\ln h(\tilde{\rho})}{\mathrm{d}\ln \rho} = \frac{\sum_n \frac{n}{3} \tilde{\rho}^{n/3} C_{V,n}}{\sum_n \tilde{\rho}^{n/3} C_{V,n}} \tag{3.20}$$

The results/predictions for γ and $h(\tilde{\rho})$ will be studied for a number of systems and is the main result of this part of the thesis.

3.1.1 Intermezzo: the Grüneisen parameter

Eduard Grüneisen derived in 1912 a model describing the effect a density change of a mono atomic crystal lattice has on the phonon frequencies in the lattice. This is comparable to our investigations of density changes influence on liquid dynamics and structure.

The equation for $\gamma(\tilde{\rho})$ (3.20) resembles the Grüneisen parameter γ_G from its microscopic definition in the way that it is also a sum of weighted heat capacities:

$$\gamma_G = \frac{\sum_i \gamma_i c_{V,i}}{\sum_i c_{V,i}} \,. \tag{3.21}$$

But the physics is completely different and it is derived on totally different grounds. Here the sum over i is that of phonon frequencies in the solid crystal. The γ_i's are defined as the volume dependence of the ith mode of vibration in the crystal lattice:

$$\gamma_i = \frac{\partial \ln \omega_i}{\partial \ln \rho} \tag{3.22}$$

ω_i being the frequency of the i'th mode and the $c_{V,i}$'s are the partial vibrational contributions the the heat capacity: $c_V = \sum_i c_{V,i}$.

It can be showed that this microscopic definition is related to a macroscopic (or thermodynamic) definition by summing over all the γ_is in the first Brillouin zone. See e.g. [Ashcroft 1976, Barron 1957].

$$\gamma_G = \frac{\alpha_p K_T}{c_V} \tag{3.23}$$

where α_p is the isobaric thermal expansion and K_T is the isothermal bulk modulus defined by

$$\alpha_p = \frac{1}{V}\frac{\partial V}{\partial T}\bigg|_P \quad \text{and} \quad K_T = -V\frac{\partial P}{\partial V}\bigg|_T \,. \tag{3.24}$$

The thermal expansion α_p and the bulk modulus K_T is related to the isochoric thermal pressure coefficient β_V [Gnan 2009, Schrøder 2011]

$$\beta_V \equiv \frac{\partial P}{\partial T}\bigg|_V = -\frac{\partial V}{\partial T}\bigg|_P \frac{\partial P}{\partial V}\bigg|_T = -\alpha_p K_T \,. \tag{3.25}$$

Substituting the isochoric thermal pressure from (3.25) into equation (3.23) we find:

$$\gamma_G = -\frac{\beta_V}{c_V} \tag{3.26}$$

which is almost our definition of γ from equation (1.6), except that our γ is governing the configurational contribution:

$$\gamma = -\frac{\beta_V^{ex}}{c_V^{ex}} \tag{3.27}$$

In condensed matter, the ideal term is usually much smaller than the configurational contribution and so the two γ's will be much the same. See also section IV paragraph A in [Schrøder 2009] and [Paper IV] for a discussion of the Grüneisen parameter and a Grüneisen equation of state respectively.

3.2 Scaling of the Kob-Andersen Binary Lennard-Jones system

This system has been used extensively since Kob and Andersen introduced it in 1994 [Kob 1994] and is one of the most studied system in viscous liquids because of its reluctance to crystallize due to its strong interaction between the big and small particles [Toxvaerd 2009]. It consists of 80 % big A particles and 20% small B particles. The potentials look as follows:

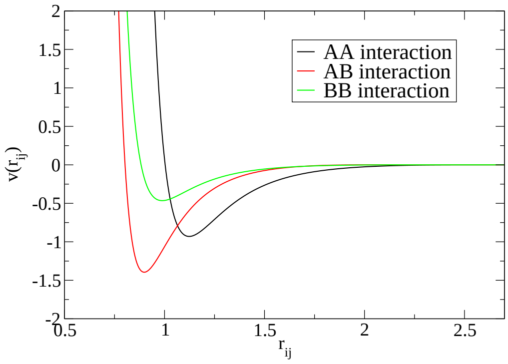

Figure 3.2: Kob-Anderson Binary Lennard-Jones potentials. The black line is the AA interaction, AB is red and the BB interaction is green. The strong interaction between A and B: $\varepsilon_{AB} = 1.5\varepsilon_{AA}$, makes this system reluctant to crystallization.

In section 3.1 we derived the long density jump formula from the isomorph definition. In this scaling equation, relating density and temperature at one state point to isomorphic state points, the density scaling exponent γ_0 is entering. At viscous state points, dynamics is highly sensitive to small temperature changes. It is therefore important to have a reliable way of determining γ_0. In this section we investigate different ways of estimating/calculating γ_0 and observe the quality of the scaling when going to viscous state points.

The scaling function $h(\tilde{\rho})$ is displayed in equation (3.17) and written here again for completeness:

$$h(\tilde{\rho}) = (\gamma_0/2 - 1)\tilde{\rho}^4 + (2 - \gamma_0/2)\tilde{\rho}^2 \,. \tag{3.28}$$

We investigate three different ways of determining γ_0 where the subscript 0 is included to emphasize that it is a constant parameter. The first is from the UW fluctuations at the starting state point (ρ_0, T_0):

$$\gamma_0 = \frac{\langle \Delta W \Delta U \rangle}{\langle (\Delta U)^2 \rangle} \,. \tag{3.29}$$

The second method used to find γ_0 is done by calculating the slope of isochoric UW data:

$$\gamma_0 = \left. \frac{\partial W}{\partial U} \right|_V \tag{3.30}$$

and the third method is by collapsing two isochores using power law density scaling: ρ_0^γ/T with γ_0 as fitting parameter.

3.2.1 Using $h(\tilde{\rho})$ with γ_0 from one state point

Calculating γ_0 at state point $(\rho_0, T_0) = (1.20, 0.55)$, the $U - W$ fluctuations (3.29) gives $\gamma_0 = 5.17 \pm 0.01$ (the subscript 0 indicates a reference to the starting state point and the uncertainty represents one standard deviation calculated from 10 independent runs). Inserting this in eq. (3.28) and calculating the corresponding temperatures for densities $\rho = 1.20$ up to $\rho = 10.0$ gives temperatures from 0.55 up to 4200. As already shown in figure 2.2 the correlation coefficient decreases when going to lower densities and increases going to higher densities.

In what follows, the simulations are performed in reduced units. It is a technical issue and has a physical interpretation. See section 3.4 on how it is done and why it is not a problem simulating liquids with densities $\rho = 10.0$.

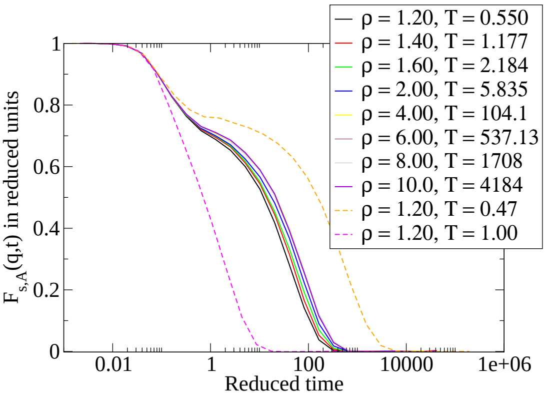

Figure 3.3: Intermediate incoherent scattering function on an isomorph in reduced units. The relaxation time is defined as where $F_{s,A}(q,t) = 1/e$. The q values are chosen to lie close to the first peak of the structure factor in reduced units $\tilde{q} = 7.25 * (\rho/1.2)^{1/3}$. For comparison two state points with $\rho = 1.20$ and different temperatures than the starting state points is displayed with broken lines.

For this isomorph and in the following we quantify the invariance of the dynamics by calculating the reduced relaxation time. The reduced relaxation time, defined as where the incoherent intermediate scattering function has decayed to $1/e$, is 26 in reduced units for $\rho_0 = 1.20$ and increases slowly to 48 for the highest density. See figure 3.3.

At each state point γ is calculated from the fluctuations of potential energy and virial eq. (3.29) and the corresponding prediction for $\gamma(\tilde{\rho})$ from (3.19) is calculated to observe the quality of the prediction. The partial heat capacities contribution to the total heat capacity is interpreted as a weighting factors of how much each term in the potential is contributing to the physics at the corresponding state point. Since the attractive term is negative, the contribution from this term is also negative implying the repulsive term is larger than 1. For the starting state point with $\gamma_0 = 5.17 \pm 0.01$ we find the following weighted heat capacities:

$$\frac{C_{V,12}}{C_V} = \left(\frac{\gamma_0}{2} - 1\right) = 1.59 \quad \text{and} \quad \frac{C_{V,6}}{C_V} = 1 - \frac{C_{V,12}}{C_V} = -0.59 \tag{3.31}$$

The prediction of $\gamma(\tilde{\rho})$ and the calculated γ's at the state points simulated on the isomorph is shown in figure 3.4. It is seen to follow the prediction very well. It is seen that the state point at $\rho = 10.0$ have $\gamma \simeq 4.00$. At this state point all the physics is dominated by the repulsive term since $C_{V,6}/C_V \simeq 0$ consistent with our physical intuition that repulsions dominate at high densities and pressures.

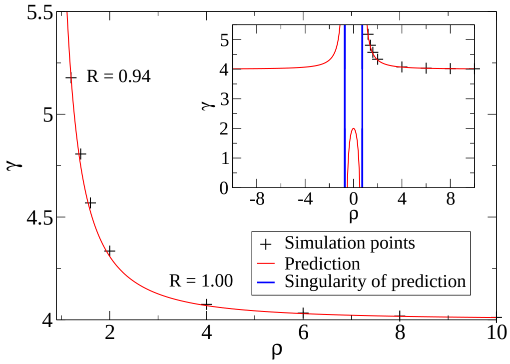

Figure 3.4: Prediction of γ and simulated points. The inset show the prediction of γ for densities -10 to 10 which is rather unphysical with negative densities. The prediction is symmetric and has a singularity shown with blue. The correlation coefficient is written for $\rho = 1.20$ and 4.00 it increases with density. At a density of $\rho \sim 1.00$ the simulations crystallize, phase separate and the correlation is so low that the isomorph theory breaks down. This corresponds to approaching the triple point and entering the coexistence phase in the (ρ, T) phase diagram.

Choosing a more viscous state point $(\rho_0, T_0) = (1.20, 0.47)$ as starting state point, we find $\gamma_0 = 5.16 \pm 0.02$ and simulate the same density range as the previous isomorph. On figure 3.5 we display the results for the incoherent intermediate scattering function. As can be seen, the reduced relaxation time for the starting state point is $\tilde{\tau} \sim 335$. Going up in density produces dynamics that are much slower than this. The relaxation times for the highest density is $\tilde{\tau} \sim 2500$. Jumping to $(\rho = 2.00, 4.97)$ has $\tilde{\tau} \sim 1360$ more than 4 times as slow as the starting state point.

Since the deviation from the perfect isomorph is systematic - the reduced relaxation time increases with density - we expect that we can produce a better isomorph by estimating γ_0 differently. Note since the dynamics does not change significantly from

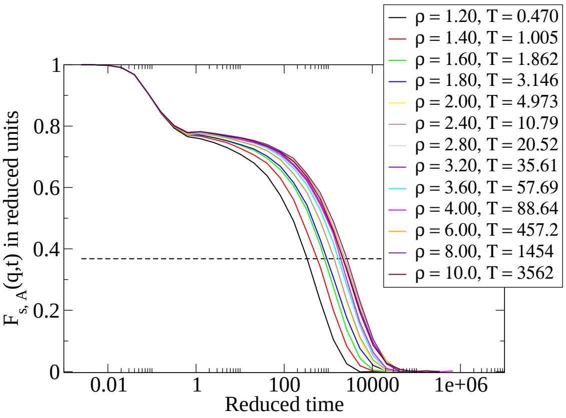

Figure 3.5: A "bad" isomorph with starting state point $(\rho_0, T_0) = (1.20, 0.47)$ and $\gamma_0 = 5.16 \pm 0.02$ having $\tilde{\tau} \sim 335$. These relaxation times increase with density up to $\tilde{\tau} \sim 2500$ for $\rho = 10$.

densities $\rho = 2$ and up, we focus on jumps up to $\rho = 2$.

3.2.2 Using $h(\tilde{\rho})$ with γ_0 from UW isochore slope

As seen in equation (3.30) γ_0 is the slope of the (U, W) energies at constant density. Because γ_0 is state point dependent: $\gamma_0 = \gamma_0(\rho, T)$ it may be possible to generate viscous isomorphs by estimating γ_0 as the mean γ_0 on an isochore. In this subsection we are calculating γ_0 by fitting a straight line to the UW energies on an isochore. Choosing the $\rho_0 = 1.60$ isochore and fitting to all energies results in a slope with $\gamma_0 = 4.52$. See figure 3.6. Since it is the viscous region with the slowest relaxation times we are interested in, we argue that it should be the most viscous state points to perform the fit on. This is the same as [Pedersen 2010] did estimating γ_0 for the single KABIPL potential describing the physics of KABLJ. Performing the fit for the 6 most viscous state points, we obtain a slightly higher $\gamma_0 = 4.58$. Using this value in the density scaling formula, we calculate isomorphs with a longer relaxation time than earlier. See figure 3.6 for UW data, fit and dynamics of these state points.

We generated four isomorphs using $\gamma_0 = 4.58$ with reduced relaxation times: $\tau_0 \approx (4.5, 40, 430, 3300)$, significantly slower than previously studied isomorphs. The results for dynamics and $\gamma(\rho)$ are displayed in figure 3.7. We see that they are all to a good approximation invariant, but the reduced relaxation times for the slowest isomorph are going from $\tilde{\tau} \simeq 2500$ for the lowest density up to $\tilde{\tau} \simeq 4700$ for the highest densities.

3.2.3 Using $h(\tilde{\rho})$ with γ_0 from isochore collapse

Three isochores with densities $\rho = 1.20$, $\rho = 1.60$ and $\rho = 2.00$ were simulated at different temperatures, starting from a high temperature and cooled down to a viscous state point. The structural relaxation time τ_α is defined here as the time where the self part of the

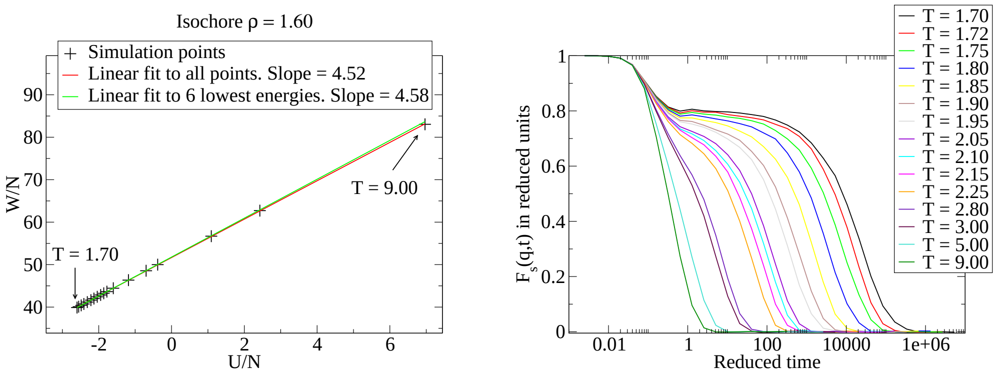

Figure 3.6: Left: Potential energy vs. Virial on the $\rho = 1.60$ isochore. The slope gives γ_0. We perform two fits: To all the state points with $\gamma_0 = 4.52$ and to the 6 lowest energies with $\gamma_0 = 4.58$. Right: Self part of the incoherent intermediate scattering function for the state points on this isochore.

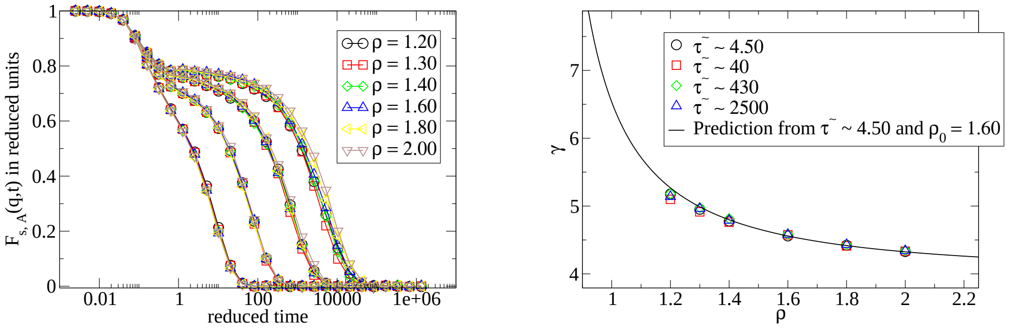

Figure 3.7: Four different isomorphs with reduced relaxation times $\tilde{\tau} \approx 4.5$, 40, 430 and 3300. Left: the incoherent intermediate scattering function in reduced units. Right: γ and the prediction plotted against density. The slowest isomorph have reduced relaxation times from $\tau \simeq 2500$ up to $\tau \simeq 4700$.

incoherent intermediate scattering function for the A particles has decayed to a value of $1/e$.

The three different isochoric relaxation times is plotted in figure 3.8 as a function of $f(\rho^{\gamma}/T)$. It is known [Coslovich 2008, Pedersen 2010] that power law density scaling with a fixed exponent γ makes the relaxation times (or diffusion coefficients) scale in reduced units for small density changes. Here we show that power law density scaling breaks down for large density variations.

The three different isochores are plotted against the power law density scaling variable ρ^{γ_0}/T, by changing γ_0 two of the isochores collapse, but no single γ_0 collapse all the isochores. The fact that power law density scaling with exponent $\gamma_0 = 4.90$ makes the

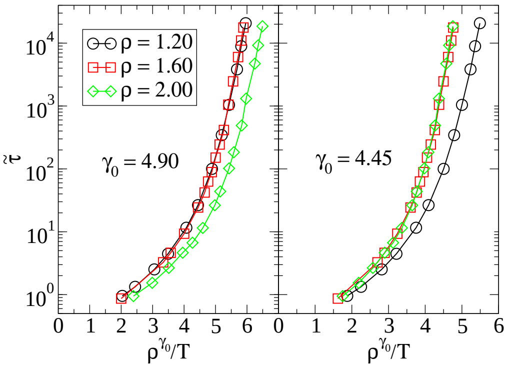

Figure 3.8: Break down of power-law density scaling. The reduced structural relaxation time $\tilde{\tau}_\alpha$ for three isochores at densities $\rho = 1.20$, $\rho = 1.60$ and $\rho = 2.00$ are plotted as a function of the density scaling variable ρ_0^γ/T. Left $\gamma_0 = 4.90$. Right: $\gamma_0 = 4.45$. It is impossible to find a single exponent γ_0 that makes all the isochores coincide.

$\rho = 1.20$ and 1.60 isochores scale onto each uniquely determines what the power law γ_0 collapsing the $\rho = 1.60$ and 2.00 should be. This can be seen in the following way. Power law density scaling imply that going from $\rho_0 = 1.60$ to $\rho = 1.20$, temperatures are scaled by:

$$\left(\frac{1.20}{1.60}\right)^{4.90} = 0.244\,. \tag{3.32}$$

Equating the density scaling function $h(\tilde{\rho} = 1.2/1.6)$ with 0.244 and solving for γ_0 in $h(1.2/1.6)$ we find:

$$\gamma_0 = \frac{2(1.2/1.6)^{4.90} + 2((1.2/1.6)^2 - 4(1.2/1.6)^4)}{(1.2/1.6)^4 - (1.2/1.6)^2} = 4.59\,. \tag{3.33}$$

Using this γ_0 in the density scaling function $h(\tilde{\rho})$ means:

$$\begin{aligned} h(\tilde{\rho}) &= (4.59/2 - 1)\tilde{\rho}^4 + (2 - 4.59/2)\tilde{\rho}^2 \\ &= 1.30\,\tilde{\rho}^4 - 0.30\,\tilde{\rho}^2\,. \end{aligned} \tag{3.34}$$

Especially $h(\tilde{\rho} = 2.0/1.6) = 2.70 = (2.0/1.6)^{4.45}$. Consistent with figure 3.8.

Recalling the constants in front of the density terms is the partial heat capacities:

$$\frac{C_{V,12}}{C_V} = 1.30 \quad \text{and} \quad \frac{C_{V,6}}{C_V} = -0.30 \tag{3.35}$$

Comparing this to the values at $\rho = 1.20$ with exponent 5.17 we had: $C_{V,12}/C_V = 1.59$ and $C_{V,6}/C_V = -0.59$. This reflects the fact that the repulsive term is more dominating here than at lower densities. The absolute value of the attractive term indicates this term contribution. Going to the limit with pure $r^{-12} \Rightarrow \gamma = 4$ repulsion we get $C_{V,12}/C_V = 1.0$ and $C_{V,6}/C_V = 0.0$. Plotting the three isochores using $h(\tilde{\rho})/T$ with $\gamma_0 = 4.59$ as a scaling parameter all three isochores scale nicely on top of each other as seen in figure 3.9.

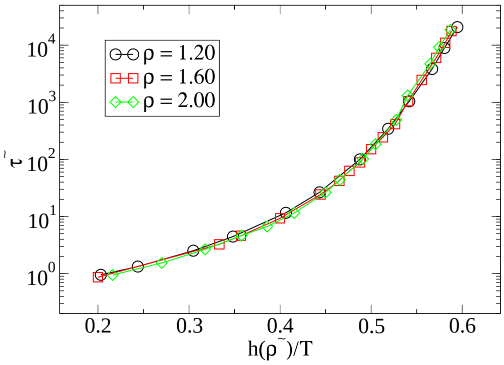

Figure 3.9: Generic density scaling. The isochores $\rho = 1.20$ and $\rho = 1.60$ are scaled to collapse onto the $\rho = 1.60$ isochore. The temperatures are scaled with: $h(1.2/1.6) = 0.244$ and $h(2.0/1.6) = 2.70$, for the $\rho = 1.20$ and 2.00 isochores respectively.

From this $h(\tilde{\rho})$ we decide to trace out four isomorphs with $h(\tilde{\rho})/T = 0.25$, 0.40, 0.50 and 0.55 for a density change of $1.2 - 2.0$ using $\rho_0 = 1.60$ and $\gamma_0 = 4.59$. Figure 3.10 beautifully show how structure and dynamics are invariant for these isomorphs. This is the isomorphs shown in paper [Paper II]. The dynamics is quantified by the self part of the incoherent intermediate scattering function and the structure by the radial distribution functions. Two fairly fast isomorphs was also simulated from densities $\rho = 1.20$ up to $\rho = 10.0$ to investigate the density dependence of γ. Plotting all isomorphs and the three isochores γ against density we see that the prediction holds well. There is some temperature

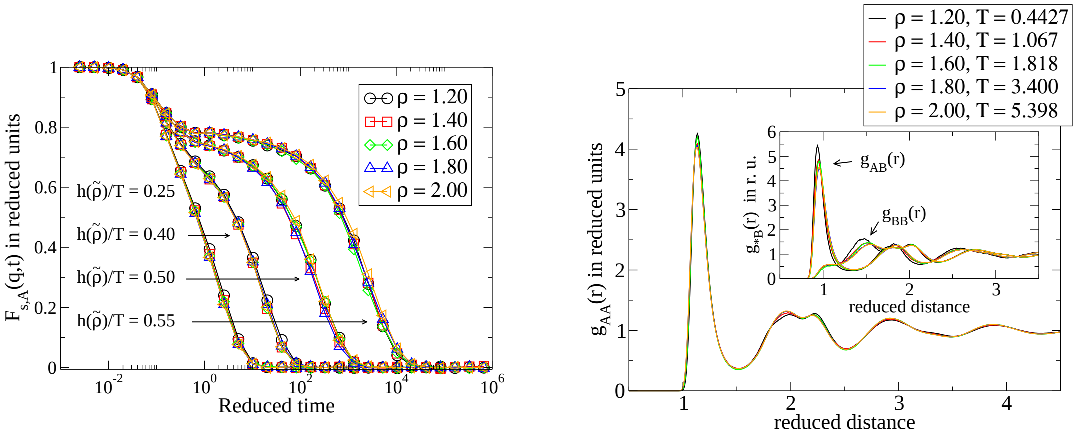

Figure 3.10: 4 isomorphs with relaxation times spanning almost 4 decades. $\gamma_0 = 4.59$ for $\rho_0 = 1.60$. Each isomorph is chosen so $h(\tilde{\rho}) = const.$ See figure for the values. Left is the dynamics probed by the self part of the incoherent intermediate scattering function for the big A particles and right is the structure quantified for the most viscous isomorph with $h(\tilde{\rho}) = 0.55$ by the radial distribution function. All distribution functions are shown.

dependence on γ for the isochores and between the different isomorphs as seen in figure 3.11.

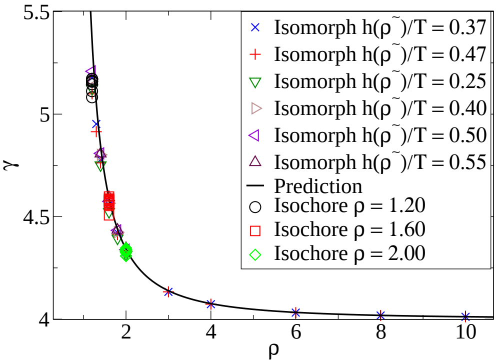

Figure 3.11: γ as a function of density for different isochores and isomorphs. The solid line is the prediction and seen to follow the simulated points well.

Structure and dynamics for the two isomorphs going up to 10 in density is shown in figure 3.12, and has $h(\tilde{\rho})/T = 0.37$ and $h(\tilde{\rho})/T = 0.47$. The reduced relaxation time for the fast isomorph is $\tilde{\tau} \sim 4.2$ and for the slower $\tilde{\tau} \sim 45$. It is seen that structure does not change much when dynamics becomes 10 times as slow.

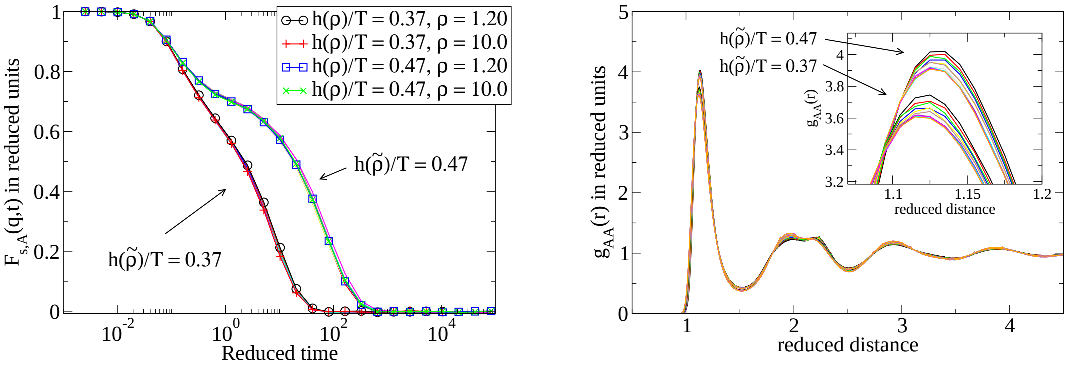

Figure 3.12: Two isomorphs with $h(\tilde{\rho})/T = 0.37$ and $h(\tilde{\rho})/T = 0.47$. Left dynamics for the big A particles. Right: structure, also for the A particles. The inset shows a zoom in of the top of the first peak.

3.2.4 KABLJ scaling conclusions

In this section we have tested the generic density scaling equation $h(\tilde{\rho})$ for the KABLJ liquid. The density scaling parameter γ_0 entering $h(\tilde{\rho})$ have been calculated in three different ways. First from a single state point with $\gamma_0 = \langle \Delta W \Delta U \rangle / \langle (\Delta U)^2 \rangle$. This method gave reasonable isomorphs if the state point is not too viscous. Secondly by calculating the scaling exponent γ_0 from a single isochore by fitting to UW energies: $\gamma_0 = \partial W/\partial U|_V$, the isomorphs produced are more invariant at viscous state points, compared to γ_0 from a single state point. Last we simulated different isochores and used power law density scaling ρ^{γ_0}/T in order to collapse two isochores by fitting γ_0. Using this γ_0 to calculate $h(\tilde{\rho})$ generated the best isomorphs at the most viscous state points.

3.3 Scaling of potentials with three terms

We test the robustness of the density scaling function by including an extra term in the potential. When 3 terms are present it is not sufficient to calculate the density scaling parameter γ_0. We need two constants and they are calculated directly as partial heat capacities via the fluctuations from a single state point. By including an extra term in the pair potential, it is possible to include an extra feature, like a local maxima after the minima. See figure 3.13. This feature with a bump is an effective potential for the ion-ion potential of liquid potassium [Sullivan 1981]. See also figure 1.4 in [Hansen 1986].

The potential is a sum of inverse power laws and defined as:

$$v_{m,n,k}(r) = a\left(\frac{\sigma}{r}\right)^m + b\left(\frac{\sigma}{r}\right)^n + c\left(\frac{\sigma}{r}\right)^k . \tag{3.36}$$

In order to have full control over the position of the minima, it is redefined in terms of the parameter α and the generalized Lennard-Jones potentials. The generalized LJ potential is defined as:

$$v_{m,n}(r) = \frac{\varepsilon}{m-n}\left\{n\left(\frac{\sigma}{r}\right)^m - m\left(\frac{\sigma}{r}\right)^n\right\} \tag{3.37}$$

and the $v_{m,n,k}$ potential is then redefined as:

$$v_{m,n,k}(r) = (1-\alpha)v_{m,n}(r) + \alpha v_{m,k}(r) . \tag{3.38}$$

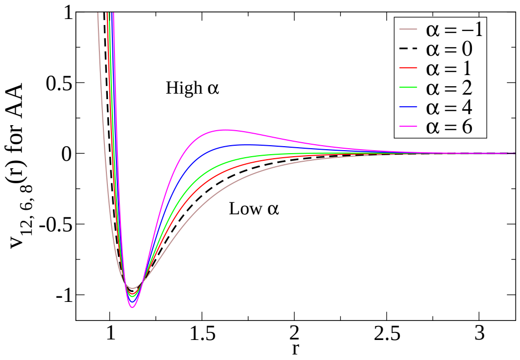

Figure 3.13: Different potentials. Going to higher α's increases the steepness of the potential. The $\alpha = 0$ potential is the normal LJ 12-6. Only potentials with $\alpha = 2$ and higher has contributions from all three terms in eq. (3.36). All the potentials are cut and shifted at $r_{c,ij} = 3.00\sigma_{ij}$ in the forces [Toxvaerd 2011].

In this study, the exponents are chosen as follows: $m = 12$, $n = 6$, $k = 8$ and $\alpha = \{-1, 0, 1, 2, 4, 6\}$. $\alpha = -1$ is the generalized Lennard-Jones potential with repulsive exponent 8 and attractive exponent 6. The standard L-J potential has $\alpha = 0$ and $\alpha = 1$ is the generalized L-J with repulsive exponent 12 and attractive exponent 8, this potential was also studied in chapter 2. Higher α's include a combination of all three terms. The simulations are performed with the Kob-Andersen mixture.

For three IPL terms, the density scaling function is:

$$h(\tilde{\rho}) = \tilde{\rho}^{m/3}\frac{C_{V,m}}{C_V} + \tilde{\rho}^{n/3}\frac{C_{V,n}}{C_V} + \tilde{\rho}^{k/3}\frac{C_{V,k}}{C_V}\,. \tag{3.39}$$

In the following we compute $h(\tilde{\rho})$ by calculating the partial heat capacities directly from the fluctuations. At each state point we also calculate the density scaling parameter γ from eq. (1.6) and compare it to the prediction:

$$\gamma(\tilde{\rho}) = \frac{\mathrm{d}\ln h(\tilde{\rho})}{\mathrm{d}\ln\tilde{\rho}} = \frac{m/3\tilde{\rho}^{m/3}C_{V,m} + n/3\tilde{\rho}^{n/3}C_{V,n} + k/3\tilde{\rho}^{k/3}C_{V,k}}{\tilde{\rho}^{m/3}C_{V,m} + \tilde{\rho}^{n/3}C_{V,n} + \tilde{\rho}^{k/3}C_{V,k}} \tag{3.40}$$

For all the systems we jump from density $\rho = 1.20$ to $\rho = 8.00$ and probe the structure as well as the dynamics for the big A particles. We restrict ourself to fairly fast state points because we calculate the parameters from one state point.

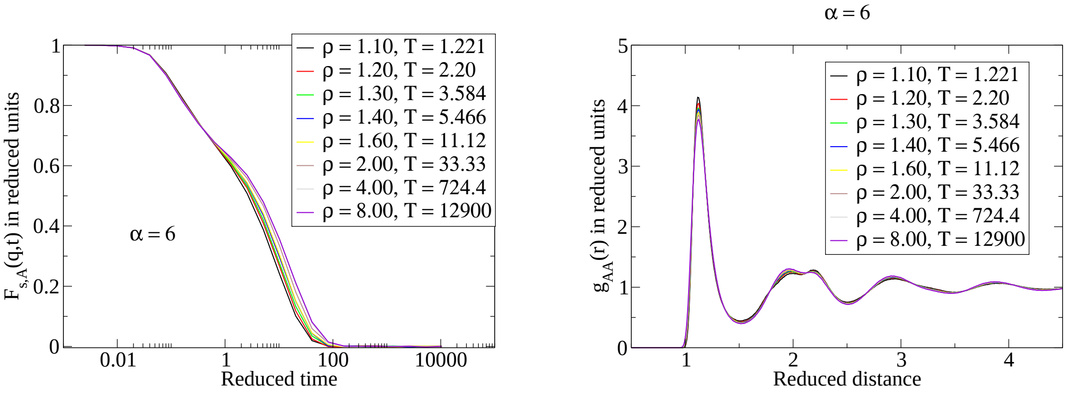

Figure 3.14: Left: Self part of incoherent intermediate scattering function in reduced units for the A particles with $\tilde{q} = 7.25(\rho/1.20)^{1/3}$. Right: The AA radial distribution function. Legend show the isomorphic state points densities and temperatures.

Choosing $\alpha = 6$ gives constants from eq. (3.36): $a = 28$, $b = -45$ and $c = 20$. An isomorph is created from density $\rho = 1.20$ and $T = 2.25$ using equation (3.39). At this state point $\gamma = 6.37$ and the partial heat capacities is $C_{V,12}/C_V = 3.21$, $C_{V,6}/C_V = 0.86$ and $C_{V,8}/C_V = -3.07$. The negative partial heat for the term with exponent 8 reflect the fact that this term is the attractive term and is therefore negative like the constant c in the potential eq. (3.36).

Figure 3.14 show the dynamics and structure for this isomorph. It can be seen that the isomorph is invariant to a good approximation. Dynamics is seen to be slower at higher densities and faster at $\rho = 1.10$. Since this is an isomorph created from knowledge of one state point $(\rho, T) = (1.20,\ 2.20)$ and the deviation from perfect collapse is systematic, it is

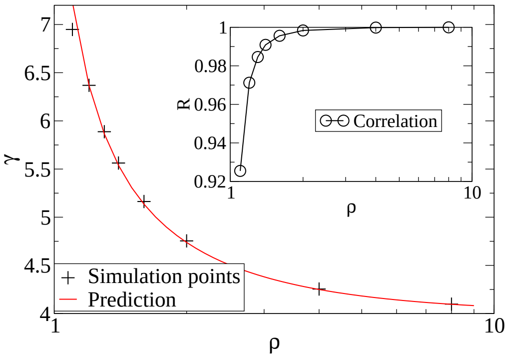

Figure 3.15: γ as a function of density. The prediction is calculated from the starting state point $(\rho, T) = (1.20, 2.20)$. Inset shows the correlation coefficient eq. 1.5 as function of density. Notice both density axes is plotted on a log scale.

expected that the procedure used in section 3.2.3 can produce better isomorphs.

The prediction of γ from eq. 3.40 is seen to work well for all the densities. The correlation decreases when density decreases and the $\rho = 1.10$ γ is seen to fall outside the prediction. It is still impressive how good this isomorph is, taken into account we have three terms, density has been increased by a factor $8/1.2 \sim 7$ and temperature by a factor $12900/2.2 \sim 6000$. Figures showing dynamics and the prediction of γ for the potentials with $\alpha = -1, 0, 2$ and 4 are shown in appendix B and are very similar to the ones for $\alpha = 6$.

3.4 A new perspective

In this section we give a new perspective on the question regarding whether or not attractive forces play an important role. We show by simulations of a single component Lennard Jones liquid that it is impossible to separate repulsive and attractive forces and the important quantity is the reduced force.

When we perform simulations at high densities, it is done by running the simulation in reduced units. Running all simulations in reduced units means we are changing the potential and keeping the state point fixed. By running in reduced units at state point $(\rho, T) = (1,\ 1)$ simply imply that the potential are expressed in reduced units. Remember reduced units are denoted by a tilde and length and energy are measured in units of $\rho^{-1/3}$ and k_BT our reduced LJ potential is written:

$$\phi(\tilde{r}) = \frac{4\varepsilon}{k_BT}\left\{\left(\frac{\sigma\rho^{1/3}}{\tilde{r}}\right)^{12} - \left(\frac{\sigma\rho^{1/3}}{\tilde{r}}\right)^{6}\right\}. \tag{3.41}$$

We simulate one state point for a single component LJ system at $(\rho_0, T_0) = (0.85, 0.80)$, from the fluctuations we calculate $\gamma_0 = 5.71$. Using the density scaling function $h(\tilde{\rho})$ we generate a set of isomorphic state points and plot the reduced potentials corresponding to these state points in figure 3.16.

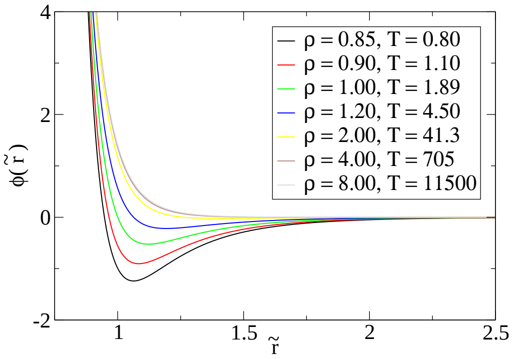

Figure 3.16: Reduced potentials for an isomorph. $\phi(\tilde{r})$ written in eq. (3.41) with densities and temperatures indicated in the legend.

These potentials are constructed to give same structure and dynamics when all potentials are simulated at $(\rho, T) = (1,\ 1)$ which is certainly the case as seen in figure 3.17. Choosing a different state point leads to same isomorphic invariance. See figures in [Paper IV]. This picture shed light on an old debate regarding the role of repulsive versus attractive forces [Paper IV]. In traditional understanding of liquid theory, repulsive and attractive forces play distinct roles for the physics. Figures 3.16 and 3.17 are not consistent with this picture where some of the potentials have insignificant attraction and are almost purely repulsive. It is well accepted in liquid theory that attractions can be regarded as a perturbation to the repulsive core. Weeks-Chandler-Anderson (WCA) [Weeks 1971] proposed cutting and shifting the Lennard-Jones potential in the minima so it is purely repulsive. This potential have shown to reproduce the Lennard-Jones potential well for the structure, but are known to be too fast in the dynamics [Berthier 2009].

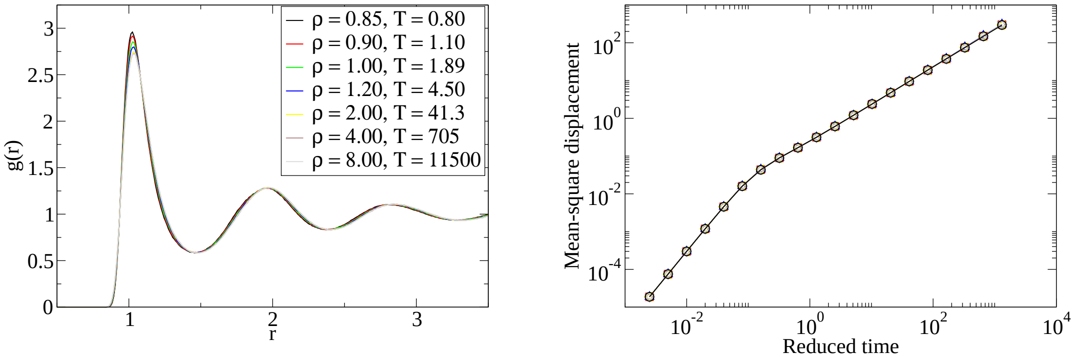

Figure 3.17: Left: Structure for the potentials showed in figure 3.16 and the dynamics probed by the mean-squared displacement.

Performing the same simulations for the WCA version of the potentials in figure 3.16 lead to similar, but less invariant, structure than the LJ isomorph. The dynamics is as expected faster than the full LJ potentials. Figure 3.18 shows the reduced WCA potentials of the same potentials shown in figure 3.16.

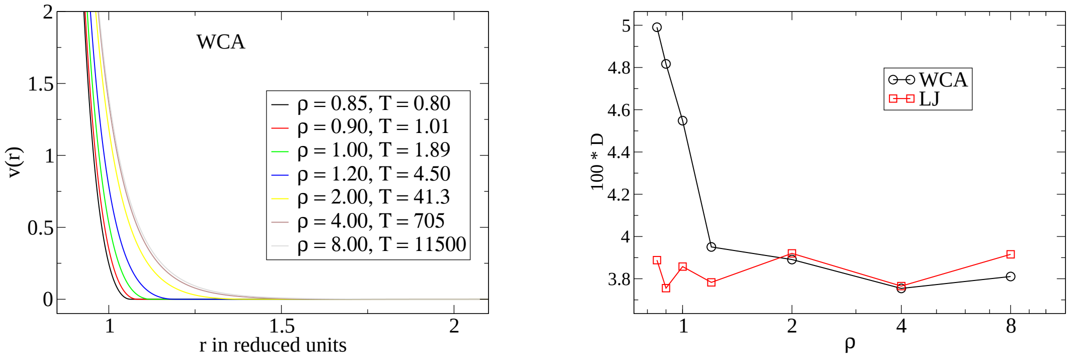

Figure 3.18: Left: WCA versions of the potentials in figure 3.16. Right: The diffusion coefficient for both the LJ potentials and the WCA counterparts.

The state points with the three lowest densities for the WCA potentials deviates significantly when calculating the diffusion coefficient. These state points are the ones in the LJ potentials that have significantly attractive contribution. For $\rho \geq 1.20$ the attraction for the LJ potentials are vanishing as seen in figure 3.16.

The reason dynamics and structure are invariant in reduced units along a LJ isomorph is not that they posses the same repulsion nor attraction, but because the reduced force is virtually the same for all the potentials.

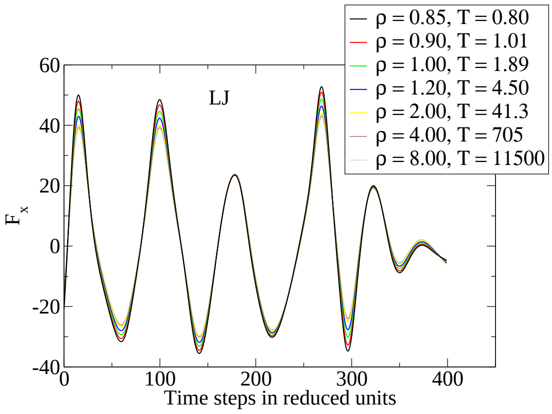

Figure 3.19: The reduced force as function of time.

In figure 3.19 we plot the reduced force in the x direction as a function of time. They are almost identical except at the extremas.

3.5 Conclusions

In this chapter we have derived a general form of density scaling relating density and temperature at isomorphic state points. The scaling have been investigated thoroughly for the KABLJ system and a family of potentials interacting with three IPL terms. The scaling is found to work very well for large density changes ($\rho = 1.2 \to \rho = 10$). From the density scaling function, the effective exponent γ is predicted and seen to hold well for all systems investigated. A new perspective is given where we show that it is impossible to separate attractive and repulsive forces from each other. The important quantity is the reduced force.

Chapter 4

Relating $h(\rho)$ directly to the potential

In this chapter we compute the effective exponent of the potential $n(r)$ and compare it to the density scaling exponent $\gamma(\rho)$. By relating the potential directly to the density scaling exponent, we convert densities to lengths and find that there is an overall length scale entering the expression for the effective exponent. We use four different single component systems and argue that this length scale is to a good approximation the distance to the top of the first peak in the radial distribution function.

4.1 Introduction

From simulations of LJ like systems we have a good understanding on the density dependence on the scaling exponent. For all these systems we have seen that $\gamma > n/3$ with n being the exponent for the repulsive term in the potential and at high densities the scaling exponent γ approached $n/3$. That is: γ goes down when density goes up.

However, from experiments on a strongly correlating liquid (van der Waals) it is the other way around. Here it is seen that γ goes up when density goes up. It is not straight forward to measure the density scaling exponent γ directly in experiments [Gundermann 2011].

In [Paper II] experimental isochrones (constant relaxation time) is extracted for a real van der Waals liquid (DHIQ) under high pressure. The procedure used to extract these points can be found in [Paper II]. From these experimental data, different relaxation times are scaled to collapse onto one master curve in a (ρ, T) plot. Thereby extracting the density scaling exponent γ as:

$$\gamma(\rho) = \frac{\mathrm{d}\ln T}{\mathrm{d}\ln \rho} \tag{4.1}$$

In figure 4.1 it can be seen that this curve is not a straight line. Implying that there exist is a density dependence on $\gamma = \gamma(\rho)$. Furthermore, the curvature of the isochrones is positive meaning γ goes up as density goes up.

We try to understand this apparent mismatch and the idea is very simple and straight forward. We examine different interatomic potentials, or more precisely the effective slope of it. We want to relate $\gamma(\rho)$ to the potential, so we convert densities to lengths by simple dimensional analysis

$$r = \rho^{-1/3}\,. \tag{4.2}$$

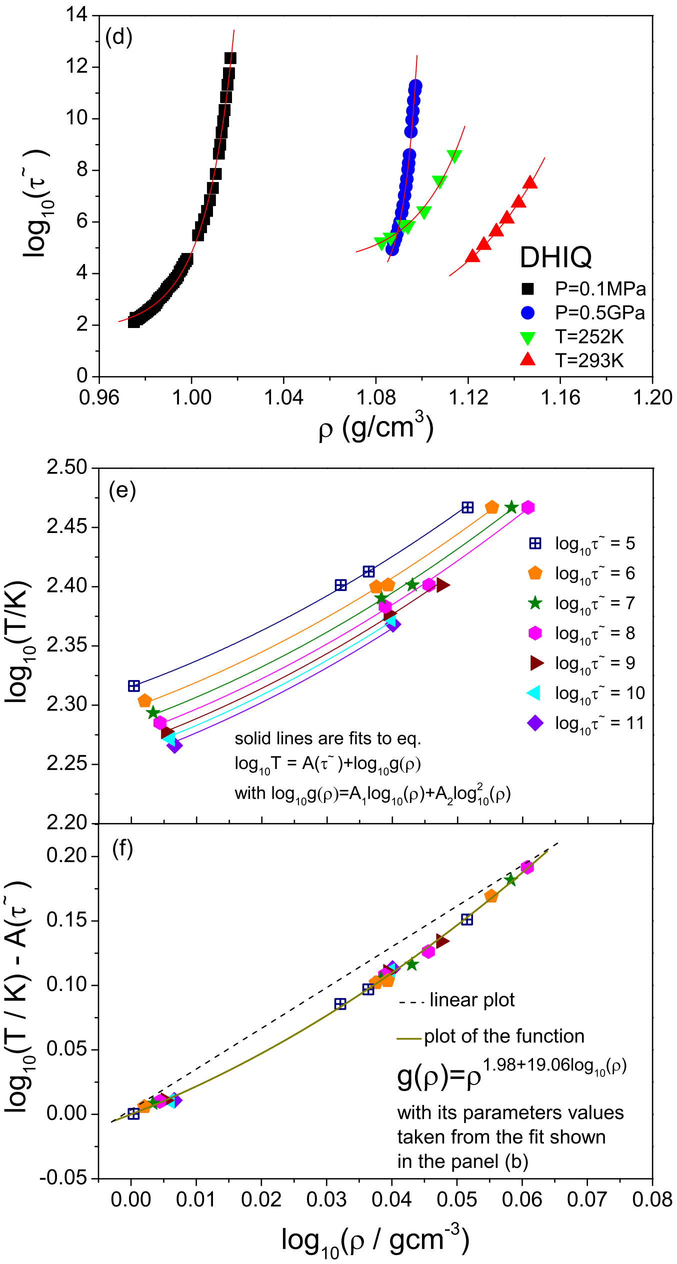

Figure 4.1: Figure taken from [Paper II]. Experimental isomorphs. (d) shows isobaric (black and blue) and isothermal (green and red) relaxation times $\tilde{\tau}$ in reduced units. (e) show isochronal dependence $\log_{10}(T)$ versus $\log_{10}(\rho)$ determined for a given reduced relaxation time $\tilde{\tau}$. (f) curves from (e) shifted to collapse. See text in figure. It is seen that the curvature in the (ρ, T) phase diagram for these isochrones is positive implying γ goes up when density goes up.

In [Bailey 2008b] it is shown that by computing successive ratios of the potential differentiated it is possible to extract an effective IPL exponent n of order p:

$$n^{(p)}(r) = -\frac{rv(r)^{(p+1)}(r)}{v(r)^{(p)}} - p\,. \tag{4.3}$$

We need at least $p+1$ differentiations to get the p'th order n and we show in section 4.4 and 4.5 that it is most likely the $n^{(2)}(r)$ effective exponent to use when describing $\gamma(r)$. This is consistent with a low temperature analysis of a crystal made in [Bailey 2008b] concluding we should use $n^{(2)}$ or higher orders of n. Replacing density with distance using (4.2) in $\gamma(\rho)$ and equating it to the effective exponent $n^{(2)}(r)$ leads to:

$$n^{(2)}(r) = 3\gamma(\rho^{-1/3}) = 3\gamma(r)\,. \tag{4.4}$$

We know that γ is state point dependent and it is also a function of temperature $\gamma = \gamma(\rho, T)$. In [Paper IV] we state that γ is only a function of density. This is the zeroth order approximation and works well. Going to next order we seek to incorporate the temperature dependence in the prediction of γ. The temperature dependence is built in by introducing a length parameter Λ which is temperature dependent $\Lambda = \Lambda(T)$.

$$n^{(2)}(r) = 3\gamma(r \cdot \Lambda). \tag{4.5}$$

The exact temperature dependence of Λ is not fully understood, but we shall see how it connects to the top of the first peak in the radial distribution function in the following sections. The position of the first peak in the radial distribution function is defined as the distance where the volumetric maximum is located:

$$\Lambda_{top} = \max(4\pi r^2 g(r))_{top}\,. \tag{4.6}$$

The subscript *top* denotes top of first peak and it is understood that Λ_{top} is a length from zero to the distance where the maximum of the position of the first peak is located. An example of how Λ_{top} is extracted for four different state points can be seen in figure 4.2. The unscaled radial distribution functions (without the volumetric factor $4\pi r^2$) are seen in left part of figure 4.4.

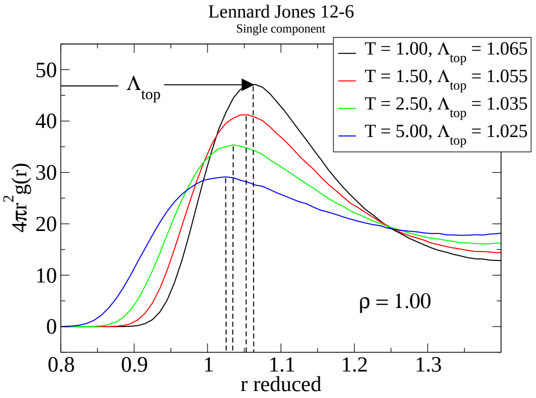

Figure 4.2: Radial distribution function times $4\pi r^2$ with the position of the maximum of the first peak Λ_{top} indicated by vertical broken lines. These are the starting state points for the LJ isomorph. The densities is 1.00 for all and the temperatures together with Λ_{top} can be seen in the legend.

Beside using Λ_{top} in equation (4.5) we also use it as a free fitting parameter Λ_{fit}. The distance to the center of mass for the first peak was investigated as a parameter, but with poor scaling.

4.1.1 The systems

In this chapter four potentials are investigated for an effective exponent of the potential. By changing density and keeping the relaxation time constant (tracing out an isomorph) it is possible to probe the potential at different distances. By doing this we have a direct measure of how much each term in the potential are contributing to the dynamics and structure. In this way we have a specific procedure of how to relate the interatomic potential directly to the dynamics. To simplify things we focus purely on single component systems and choose 4 fundamentally different potentials as seen in figure 4.3.

The four systems investigated are:

$$v_1(r) = 4\varepsilon\left\{\left(\frac{\sigma}{r}\right)^{12} - \left(\frac{\sigma}{r}\right)^{6}\right\} \tag{4.7}$$

$$v_2(r) = \frac{\varepsilon}{2}\left\{\left(\frac{\sigma}{r}\right)^{12} + \left(\frac{\sigma}{r}\right)^{6}\right\} \tag{4.8}$$

$$v_3(r) = \varepsilon\left\{\left(\frac{\sigma}{r}\right)^{18} - \left(\frac{\sigma}{r}\right)^{12} + \left(\frac{\sigma}{r}\right)^{6}\right\} \tag{4.9}$$

$$v_4(r) = \varepsilon\left\{\left(\frac{\sigma}{r}\right)^{18} - 2\left(\frac{\sigma}{r}\right)^{12} + \left(\frac{\sigma}{r}\right)^{6}\right\} \tag{4.10}$$

Model system $v_1(r)$ (4.7) is the standard Lennard-Jones potential. $v_2(r)$ (4.8) is the purely repulsive version of the Lennard-Jones potential. Model system $v_3(r)$ (4.9) is similar to the purely repulsive Lennard-Jones because it is decreasing monotonically despite the fact that a negative term is present. Potential v_4 (4.10) is similar to the normal Lennard-Jones because it has a potential well with a minima (and maxima). The potentials are plotted

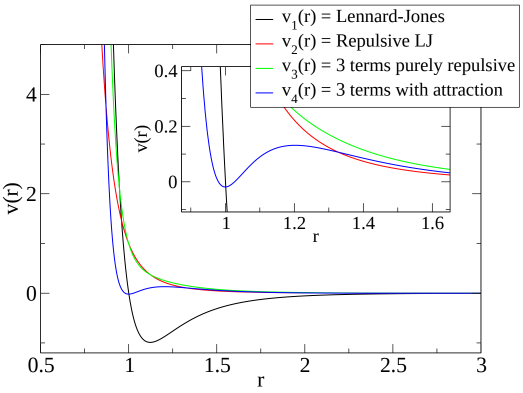

Figure 4.3: Potentials studied in this chapter. Inset zoom in on the local maxima for the potential with three terms and attraction.

in figure 4.3 were the inset show a zoom of the local maxima of system (4.10). For all model systems we simulate four isomorphs at different temperatures. These four systems behaves very different. Because single component systems crystallize easily, dynamics for all these systems is fast and does not change significantly. In the following sections we will focus on structure.

4.2 Lennard-Jones

Four state points with density = 1.00 and temperatures = {1.00, 1.50, 2.50, 5.00} was used as starting state points for different isomorphs. The LJ system undergoes a phase transition at low densities close to the triple point [Hansen 1986] so we stick to densities above 0.85. In all of the four isomorphs, we simulated a density range from 0.85 up to 8.00. In this way we are sure to visit low density state points and high density state points. The triple point for a single component Lennard-Jones liquid is $(\rho, T) = (0.85,\ 0.66)$ [Ahmed 2009] and since an isomorph have invariant structure and dynamics it means that it also describes the freezing and melting curves. Lindemanns criterion for melting line relates the mean vibrational thermal energy in the crystal to an interatomic distance. It is independent of pressure and therefore fulfills the isomorph theory. [Khrapak 2011] and Morfill actually found that the freezing and melting curves for the 12-6 LJ system must have the functional form:

$$T = A\rho^4 + B\rho^2 \,. \tag{4.11}$$

Which is seen to be the generalized density scaling function of the isomorph theory.

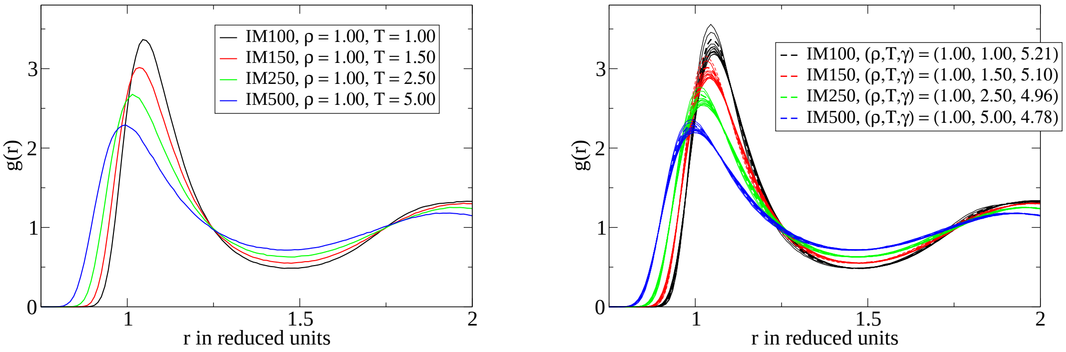

Figure 4.4: Left: Initial conditions for the isomorphs. Right: Isomorphs simulated from the state point shown to the left. Densities range from 0.85 up to 8 for all of them. Legend indicate the starting state point from where the isomorph was generated.

From [Ingebrigtsen 2012] we know that the physics for strongly correlating liquids is described by the interactions of the nearest neighbors. We believe that the reason for γ changing on an isochore is that the first peak of the radial distribution function changes. As temperature is increased the radial distribution function $g(r)$ decreases in height and the first peak moves to shorter distances. As seen on figure 4.4 it also broadens.

We used the density scaling function $h(\rho)$ to generate the isomorphs:

$$h(\rho) = \rho^4(\gamma/2 - 1) + \rho^2(-\gamma/2 + 2)\,. \tag{4.12}$$

The starting state points and their respective γ's can be seen in the legend of figure 4.4. From these state points and the γ from the starting state point, we generate isomorphs with density from 0.85 up to 8.00. At each state point we calculate γ from the fluctuations and compare them to the prediction. Because of different γ's at each isomorph we get different predictions (γ is not just a function of density). The results can be seen in figure 4.5 where a sketch of a LJ (ρ, T) phase diagram is drawn together with the isomorphs.

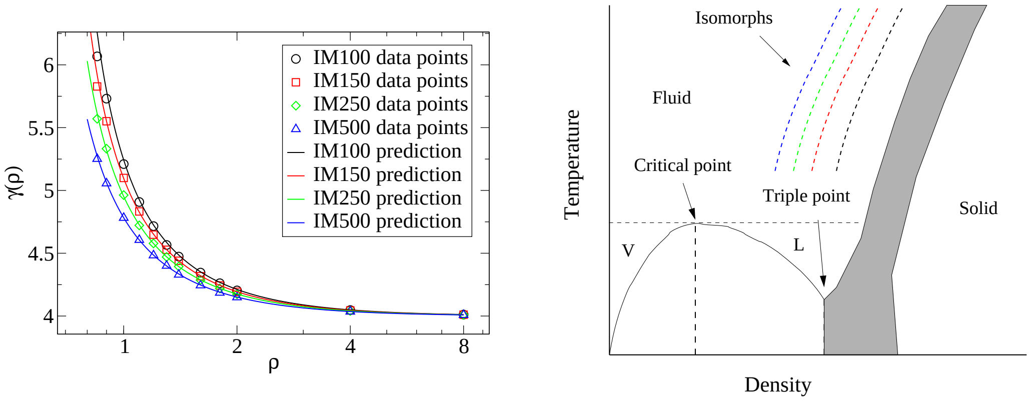

Figure 4.5: Left: γ as a function of density for the four isomorphs shown in figure 4.4 together with the prediction. Each isomorph follow their respective prediction well, but all the points does not collapse. Right: A sketch of the LJ phase diagram with the four isomorphs sketched as broken lines. The grey area is the coexistence region between solid and liquid. V and L is abbreviations for liquid and vapour.

From the starting state point we calculate Λ_{top} and Λ_{fit} and compare $n^{(2)}(r) = 3\gamma(r \cdot \Lambda)$ with the respective Lambdas on figure 4.6. From this figure it is clearly seen that the prediction agrees well with the simulated state points. The fitting gives obviously better agreement than following the first peak, but the result is fairly good. See figure 4.15 where the two Λ's are plotted against each other along with the other systems.

4.3 Purely repulsive Lennard-Jones

Because the exponents in the potential are the same as the standard Lennard-Jones potential, the same scaling function hold for this system. The biggest difference is that γ is restricted to lie between 2 and 4. 2 and 4 is the low and high density limits for γ. This potential is highly correlated as seen in figure 4.7 together with the structure for isomorphic state points. This system is also prone to crystallization if temperatures

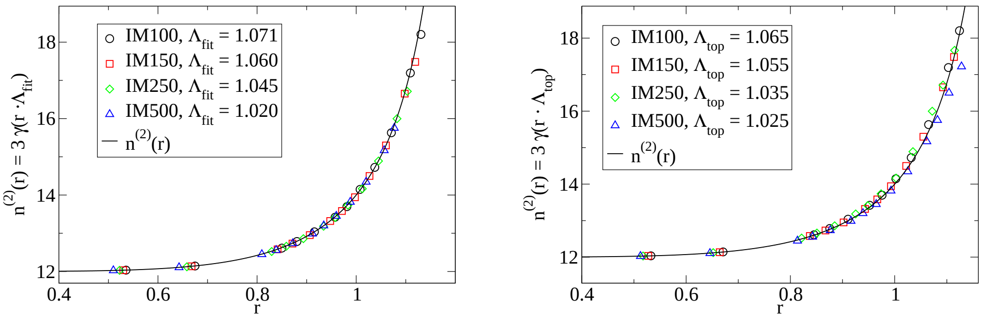

Figure 4.6: The effective exponent $n^{(2)}(r) = 3\gamma(r\Lambda)$. Left with Λ equal to a fitting parameter (shifting points horizontal to collapse on $n^{(2)}(r)$). Right with Λ equal to the position of maxima of first peak in the radial distribution function in reduced units with volume taking into account. Max of $4\pi r^2 rdf(r)|_{top}$ where the subscript *top* denote the top of the first peak. See text and figure 4.2.

or densities exceed certain values. The isomorph describe the freezing and melting curves. The height of the first peak can reach the same value as the Lennard-Jones potential before crystallizing. The (ρ, T) phase diagram does not have critical point as seen in the standard LJ (fig. 4.5), there is no coexistence region separating liquid from vapour. Figure 4.16 display one isomorph for all the systems in the (ρ, T) phase diagram. See caption and text in that figure for a discussion of potentials and phase diagrams.

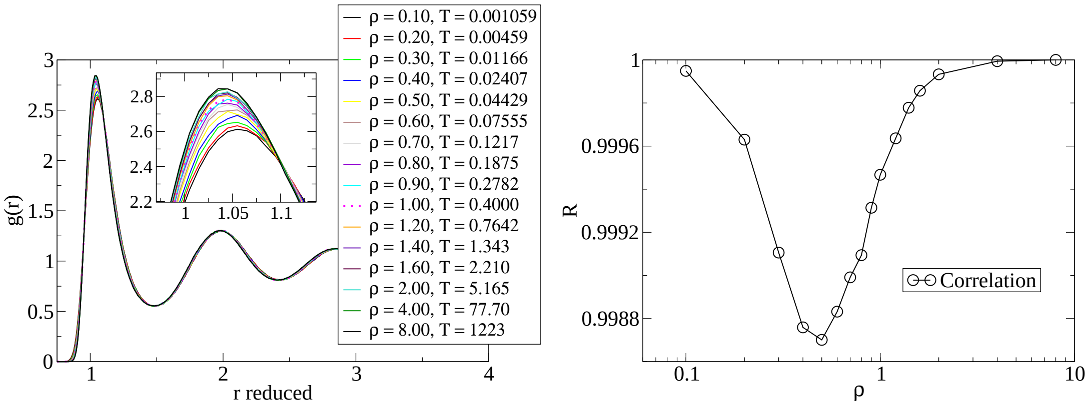

Figure 4.7: The radial distribution function for the entire isomorph plotted in reduced units. Inset show a zoom on the first peak. Structure is to a good approximation invariant in reduced units on the isomorph.

Figure 4.7 show how invariant the structure is on one isomorph (the most viscous one, closest to the freezing line). The isomorphs for the other state points are very similar. It is seen that the lowest densities first peak moves to shorter distances. The starting state point is at $(\rho, T, \gamma) = (1.0, 1.0, 3.49)$. The density scaling function at this density and temperature is

$$h(\rho) = \frac{C_{V,12}}{C_V}\rho^4 + \frac{C_{V,6}}{C_V}\rho^2 = (\gamma/2-1)\rho^4 + (-\gamma/2-2)\rho^2 \simeq 0.75\rho^4 + 0.25\rho^2 \tag{4.13}$$

where it can be seen that the ρ^4 term contributes with 75% and the ρ^2 contributes with 25% to the total heat capacity. The low and high density regimes bundle into two regions separated by intermediate densities. Overall the structure is to a good approximation constant on the isomorph. Notice that density is changed by a factor of 80 and temperature is changed approximately with a factor of 10^6. Also plotted is the correlation coefficient R which is very high for all state points. It has a dip at intermediate densities and is approaching 1 at very low and very high densities. This is consistent with just one IPL term, with 100% correlation, dominating at these limiting state points.

Again we test the isomorph prediction of equation (3.20). Following the procedure of the Lennard-Jones system we arrive at figure 4.8. The legend indicate the starting state points temperature. All starting state points have $\rho_0 = 1$ and IM040 means $T_0 = 0.40$ and IM250 means $T_0 = 2.50$ and so on.

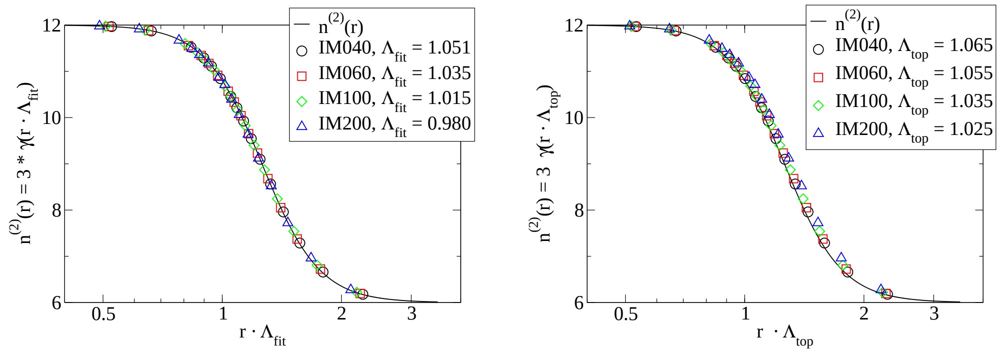

Figure 4.8: The effective exponent plotted against distance in reduced units: $r = \rho^{-1/3}$. Left with Λ_{fit} and right with Λ_{top}.

It is seen on figure 4.8 that the prediction agrees well with simulated state points. The Λ_{top} is seen to be too high compared to the fitted value, but is definitely comparable.

4.4 Three terms, but purely repulsive

We use the same procedure as the two preceding systems and generate 4 isomorphs with different structure. The structure is comparable to the Lennard-Jones isomorphs.

It is seen on figure 4.9 that the structure is not as invariant as the previous systems. The tendency here is the same as the previous purely repulsive LJ potential that the low and high densities bundle together with a gap in between them. Shown is the isomorph with the highest temperature $T = 9.00$ on the $\rho = 1.00$ isochore.

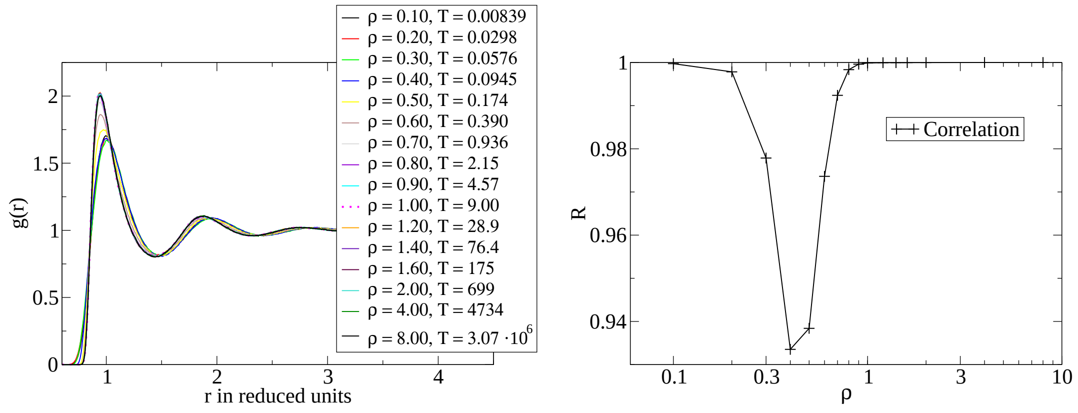

Figure 4.9: Left: The structure on this isomorph bundle into a high density structure and a low density structure. Right: The correlation coefficient as a function of density.

The intermediate densities between the two bundles are the densities between the $n = 18$ and $n = 6$ term in the potential. See figure 4.10 where the effective exponent $n^{(2)}(r)$ is plotted together with the γ's scaled with Λ_{fit} and Λ_{top}.

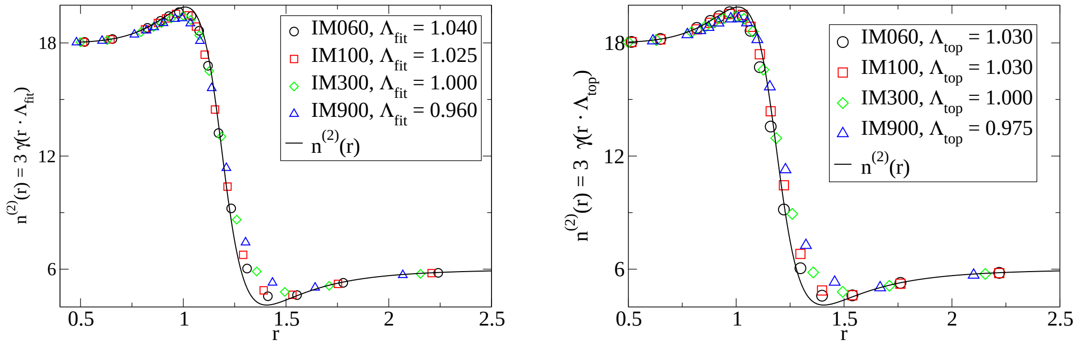

Figure 4.10: Effective exponent $n^{(2)}(r)$ together with $3\gamma(r \cdot \Lambda)$. Left with Λ as fitting parameter and right with position of first peak.

For the LJ and purely repulsive LJ systems it will always be possible to scale $\gamma(r \cdot \Lambda)$ on any order of $n^{(p)}(r)$ because it merely shifts the effective exponents left if $\Lambda < 1$ and right if $\Lambda > 1$. Having three terms in the potential, like this one and the next, it is not sufficient to scale the potential horizontally due to the maximum and minimum. To see what order of the effective exponent $n^{(p)}$ that does the best job we plot the first 5 ($p = 0 \rightarrow 4$) orders of n in figure 4.11 together with the prediction of γ from eq. (3.40) and data points from one isomorph.

The higher the order of $n^{(p)}$ is, the higher and lower the maximum and minimum gets. The prediction of γ is seen to lie in between the $n^{(1)}$ and $n^{(2)}$ effective IPL exponent.

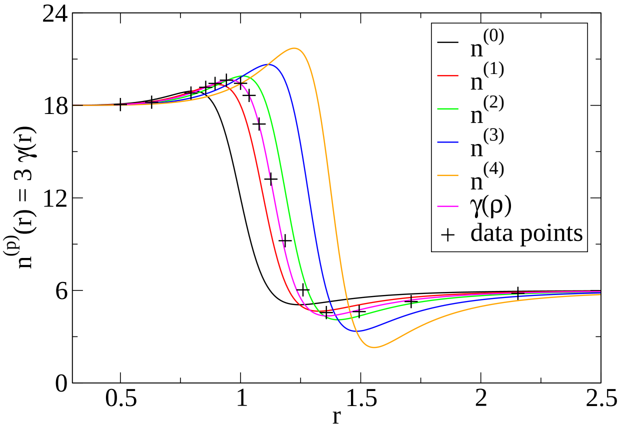

Figure 4.11: Different orders of the effective exponent $n^{(p)}$ together with γ (black plusses) and $\gamma(\rho)$ (magenta) for one isomorph. No scaling involved ($\Lambda = 1.00$). The prediction of $\gamma(\rho)$ from eq. (3.40) is seen to fall between the $n^{(1)}$ (red) and $n^{(2)}$ (green) effective IPL exponents.

4.5 Three terms, but with attraction

Because this potential has a well with a minima, the prediction of γ as a function of density has a singularity. Just like the normal Lennard-Jones. But since it also has a local maxima it has two singularities. The prediction of γ as function of density is

$$\gamma(\rho) = \frac{\mathrm{d}\ln h(\rho)}{\mathrm{d}\ln\rho} = \frac{\sum_n n/3\rho^{n/3}C_{V,n}}{\sum_n \rho^{n/3}C_{V,n}} \tag{4.14}$$

which mean that there is a singularity whenever the denominator of $\gamma(\rho)$ is zero

$$\sum_n \rho^{n/3}C_{V,n} = 0\,. \tag{4.15}$$

Close to these singularities, the simulations become unphysical and we need to stay away from these to have meaningful equilibrium simulations. The correlation coefficient drops rapidly when the critical point is approached and temperature is predicted to be negative between these singularities. See LJ phase diagram in figure 4.5. This implies that the state points where the isomorph is physical are limited to densities from 0.90 and above, like the normal LJ system, but also at very low densities where the potential is repulsive again. In right of figure 4.12 the correlation for all state points in the isomorph is shown. Left side of figure 4.12 show the radial distribution function for state points with a correlation above 90%. At the lowest density = 0.10, the structure is, as seen before, shifted to longer distances.

Figure 4.13 show the effective exponent $n^{(2)}(r)$ like the three other systems with Λ equal to a fitting parameter and the top of the first peak. At short and long distances (high and low densities) we see the the state points follow the prediction fairly well. The

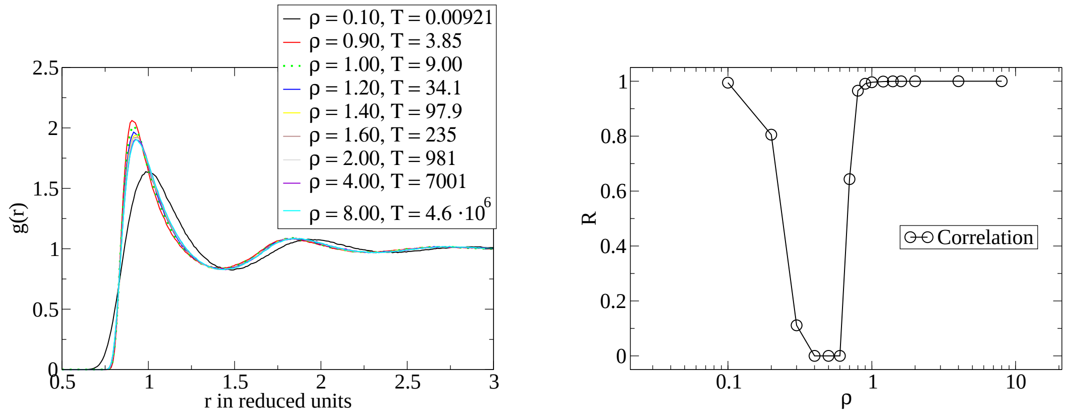

Figure 4.12: Left: Structure on the isomorph. Only strongly correlating state points is included. Right: The correlation coefficient for all densities. At intermediate densities the correlation disappears.

state points in between the two singularities are predicted to have negative temperatures. Only the lowest density (largest distance $r \simeq 2$) is strongly correlating and densities above 0.9 (distances smaller than ~ 1.04).

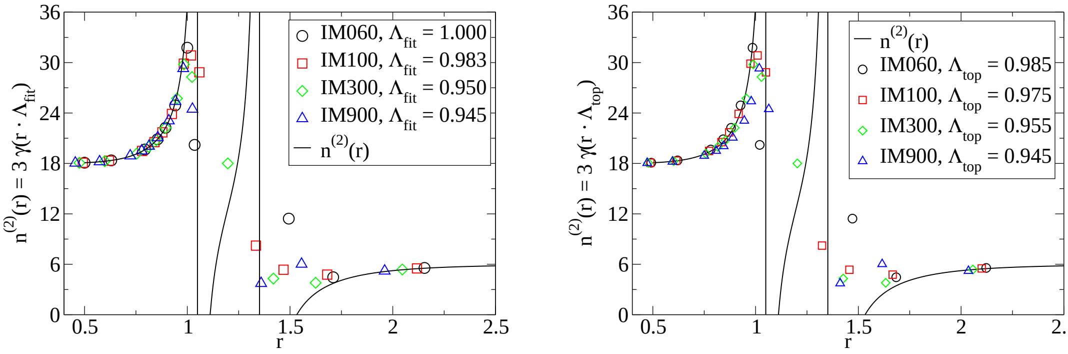

Figure 4.13: The effective exponent $n^{(2)}$ as a function of distance together with the calculated γ for all state points. Left the scaling factor Λ is fitted. Right: The position of the first peak is used as scaling factor Λ.

It is seen that away from the singularities the prediction match the simulation results well. Between the two singularities, the predicted temperature is negative. Further support for using $n^{(2)}$ as the effective exponent is given in figure 4.14 where the first 5 orders of n is plotted together with γ just as was done in the previous system.

There is a lot of things going on on figure 4.14. The message of this figure is that the width of the forbidden area between the two singularities where temperature is predicted to be negative is for $\gamma(r)$ almost identical for $n^{(2)}(r)$. Lower orders of $n^{(p)}$ are too narrow

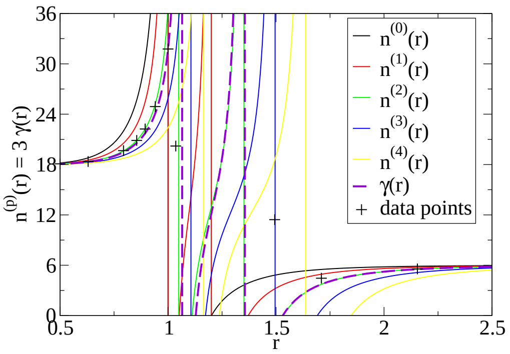

Figure 4.14: Different orders of the effective exponent $n^{(p)}$ is plotted together with simulation points and the prediction γ. Purple broken line is the prediction for γ and green line is $n^{(2)}$ almost coinciding with each other.

and higher orders of $n^{(p)}$ are too wide.

4.6 Conclusions and discussion

It is possible to approximate the effective exponent γ derived from the isomorph theory to an effective IPL exponent $n^{(p)}$ derived purely from the interaction potential. The right order of n seems to be 2. Plotting the fitted values of Λ against the position of the first peak results in almost a straight line. See figure 4.15 where a guide to the eye with $\Lambda_{fit} = \Lambda_{top}$ also is plotted.

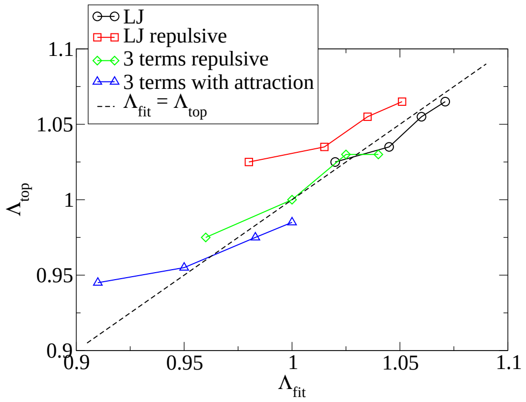

Figure 4.15: Plotting Λ_{fit} against Λ_{top} shows there is a correlation between the position of the first peak and the effective exponent γ.

On figure 4.16 density and temperature is plotted against each other in a log-log plot. These curves indicate freezing and melting lines in the (ρ, T) phase diagram. The density

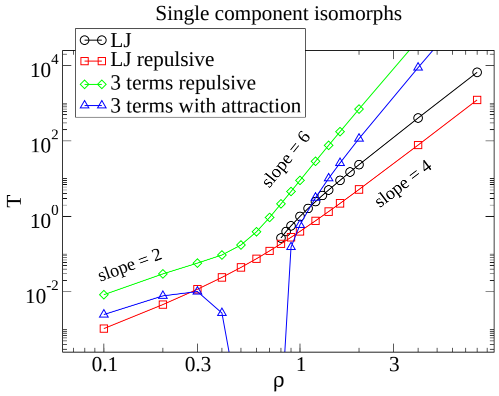

Figure 4.16: log-log plot of density and temperature for isomorphic state points, one isomorph for each system. These lines indicate freezing and melting curves for their respective systems.

scaling exponent γ is given by:

$$\gamma(\rho) = \frac{n^{(2)}(\rho)}{3} = \frac{\mathrm{d}\ln T}{\mathrm{d}\ln \rho}\,. \tag{4.16}$$

The curvature of these plots, $\mathrm{d}^2 \ln T/\mathrm{d}(\ln \rho)^2$, are seen to have different signs, depending on whether or not attraction is present. The standard LJ and the three terms with attraction have negative curvatures where the purely repulsive systems LJ and three terms have positive curvature. If the curvature is positive then γ increases as density increases and if it is negative it decreases when increasing density.

Part II

The Rolypoly - a Solid of Constant Width

Chapter 5

Introduction

In this chapter we introduce the rolypoly and motivate our work.

5.1 Motivation

Great progress in particle synthesis have created a massive interest in designing nano particles with the aim of producing materials bottom up [Whitesides 2002, Glotzer 2007]. By customizing the particle it is possible to achieve desired material properties for targeting specific crystal structures. These nano particles are predicted to become the building blocks of tomorrows materials and are found in a variety of anisotropic shapes. Studies with truncation or rounding of corners on polyhedra particles, reveals many different thermodynamically stable crystal phases, [Damasceno 2012a, Ni 2012] including quasi-crystals. Understanding these self assembly phenomena is complex and it is natural to simplify the problem by eliminating interactions. These hard particle models are not only of interest to the material scientists, but raises fundamental problems in mathematics and computer science [Chen 2010] and serves as a stepping stone towards understanding self assembly.

By eliminating Van der Waals, electrostatic and magnetic interactions the system consists of hard impenetrable particles. These systems are subject to phase transitions, and are driven into equilibrium by entropic forces. The free energy of the system depends on translational and orientational degrees of freedom and the system will eventually fall into equilibrium when the free energy is minimized. The most studied hard particle is the hard sphere and it is well known that this particle will form a stable face centered cubic (fcc) [Bolhuis 1997a]. The difference in free energy between the (fcc) lattice and hexagonal close packed (hcp) is small but present. Hard rod or disc like particles form liquid crystals if they are sufficiently anisotropic [Bolhuis 1997b, Marechal 2011] and particles with shapes that are close to spherical order into plastic crystals known as rotator phases [Vega 1997, Bolhuis 1997b]. The goal is to relate the shape of the particle directly to the target structure [Damasceno 2012b, de Graaf 2012].

In this chapter we perform Monte Carlo simulations of solids with constant width. Solids of constant width are sometimes referred to as *spheroforms*. The simulated particle is a two parameter object that are varied continuously from a sphere to a regular rotated Reuleaux triangle[1]. Shapes in between can rightfully be termed a **non regular rotated Reuleaux triangle**. Instead of calling it a non regular rotated Reuleaux triangle we

---

[1] See e.g. `http://en.wikipedia.org/wiki/Reuleaux_triangle`.

provide it with a short name: the **Rolypoly** meaning round shaped.

The purpose of the simulations is two fold. For the Rolypoly we will study:

- How dense the particles can be packed
- The glass forming ability (nucleation rate)

The densest packing of a solid is a mathematical challenge that keeps fascinating mathematicians. Aristotle mistakenly thought the regular tetrahedrons could fill space completely. It took many years before someone argued against him and the arrangements for densest packing of tetrahedrons is a record that keeps getting beat [Chen 2010].

The glass forming ability is a measure of the ability to crystallize and is proportional to the nucleation time. It has recently been discovered that single component ellipsoids are good glass formers [Letz 2000] which helped motivating this study. We calculate the glass forming ability of a selected number of rolypolys.

5.2 Introducing the rolypoly

The rolypoly is a solid of constant width, which means that the measured distance between two parallel plates is constant irrespective of the direction in space. To the best of our knowledge no one has simulated this particle/geometry before. It is a family of two parameters which can be changed continuously from a sphere to a regular rotated Reuleaux triangle.

The rolypoly is defined as 6 circular arcs with varying radii, choosing an overall length for the constant width (we choose 2 for convenience) the particle can be uniquely determined by two parameters. Draw an isosceles triangle and extend the lines, these three lines intersect at three vertices used as centers for the circular arcs. See figure 5.1. The two parameters a_1 and a_2 in the rolypoly are defined as the radii of the top and lowest side region. See figure 5.1. In two dimensions, the extremes are a circle and a Reuleaux triangle. The three dimensional rolypoly is simply rotated around its center of axis.

We define the constant width c to be 2 in all our simulations. The two parameters are then restricted to the interval

$$0 \leq a_1 \leq c/2 = 1 \quad \text{and} \quad 0 \leq a_2 \leq c/2 = 1\,. \tag{5.1}$$

A plot of the Rolypolys can be seen in figure 5.2 where a_1 and a_2 are varied in steps of 0.2 from 0 to 1.[2]

---

[2] Elizabeth R Chen has kindly provided me with a mathematica script to generate the Rolypolys in figure 5.2.

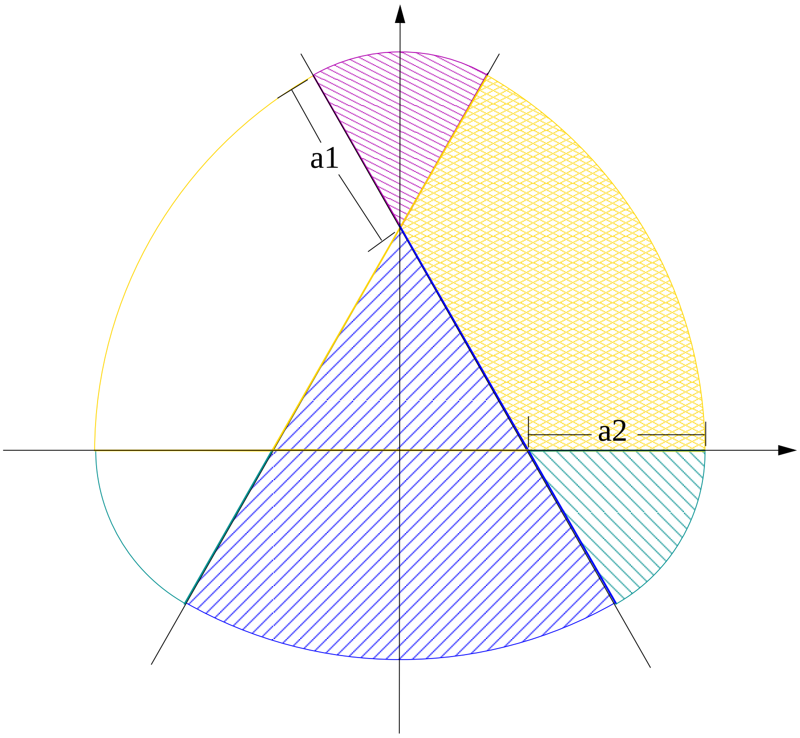

Figure 5.1: Rolypoly in 2D, the different colors represent different domains of the rolypoly shape. The colors are approximate the same as in figure 5.2 where a 3 dimensional version is displayed for a selected number of parameters.

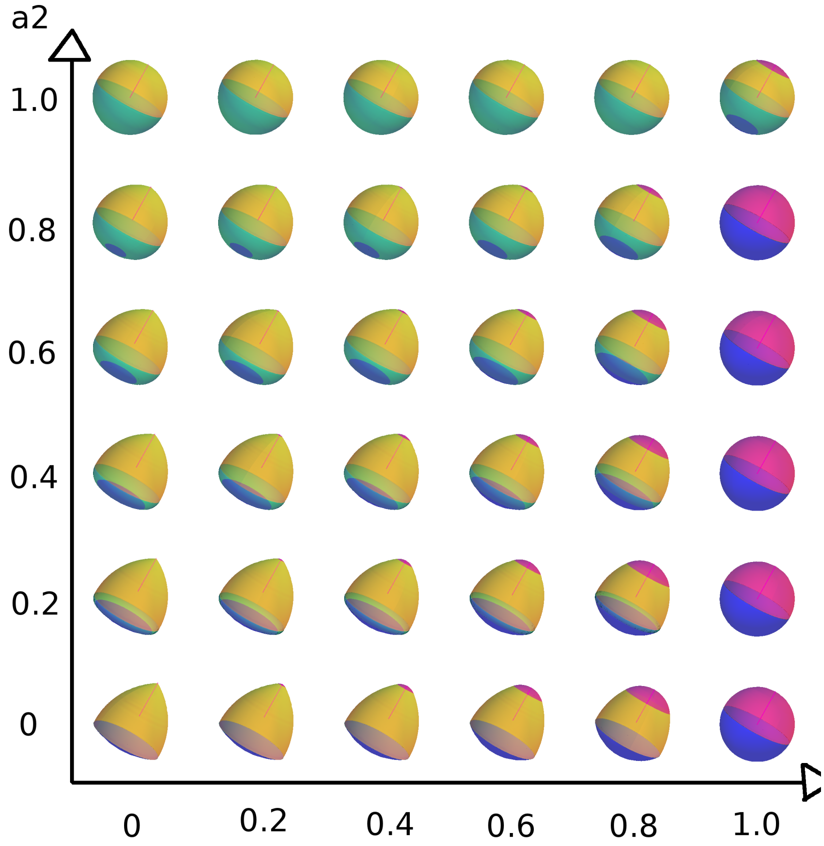

Figure 5.2: The family of Rolypolys. a_1 and a_2 are varied in steps of 0.2. If both of them are zero, the most anisotropic shape - a rotated Reuleaux triangle - is obtained. If one of a_1 or a_2 is one the shape is a sphere. Different colors represent different regions of the Rolypoly. Approximate the same color coding as figure 5.1.

CHAPTER 6

Densest packing

We calculate the densest packing of rolypolys by simulating 1, 2, 3 and 4 particles in the unit cell. The numerical results for one particle in the unit cell is confirmed by an analytical expression. We discover different topological domains for two particles in the unit cell. The densest packing is not achieved for the most anisotropic particle, but has a global maximum for $(a_1, a_2) = (0.00, 0.07)$ with two particles in the unit cell. Simulations with three and four particles did not reach higher packing fractions than for two particles.

Packing of solids have intrigued mathematicians since the ancient Greeks. It is of academic interest to see how these geometries should be arranged in order to fill most possible of space. We attack this problem by performing Monte Carlo simulations using the code Incsim (INteractive C SIMulation) and the visualization program Injavis (INteractive JAva VISualization) both developed by Michael Engel at the University of Michigan.

The procedure is simple and consists of an algorithm compressing the simulation box in the NPT ensemble and allowing shear deformations. Starting from a low pressure (a dilute system) the simulation box is slowly compressed and sheared until an unreasonable high pressure ensure that the packing fraction does not change significantly (going to the fifth significant figure). Iterating this procedure by keeping the highest packing fraction and the configuration we obtain the densest packing. This algorithm does not guarantee that the densest packing is found. The procedure was used with one, two and three particles in the unit cell. In what follows, we only consider mono disperse simulations.

The validity of the program was done by visual inspection to see if any overlap occurred and by recovering literature data from the hard sphere model. The densest packing of hard spheres was proofed by Gauss in 1831 to be

$$\phi_{\text{sphere}} = \frac{\pi}{\sqrt{18}} \simeq 0.74048... \tag{6.1}$$

There exist two different arrangements for the sphere that achieve this packing fraction. It is the fcc and hcp arrangements and due to the slightly lower free energy for the fcc [Bolhuis 1997a], this configuration is obtained in simulations and experiments. Our densest packing for two particles in the unit cell does not distinguish between fcc and hcp since there is only two layers and the third layer determines if it is the fcc or hcp lattice.

6.1 One particle in the unit cell

For one particle in the unit cell, the densest packing is found to have a lower packing fraction than the sphere. Figure 6.1 show the results of the simulations where it is seen that increasing anisotropy (decreasing a_1 and a_2) implies decreasing packing fraction.

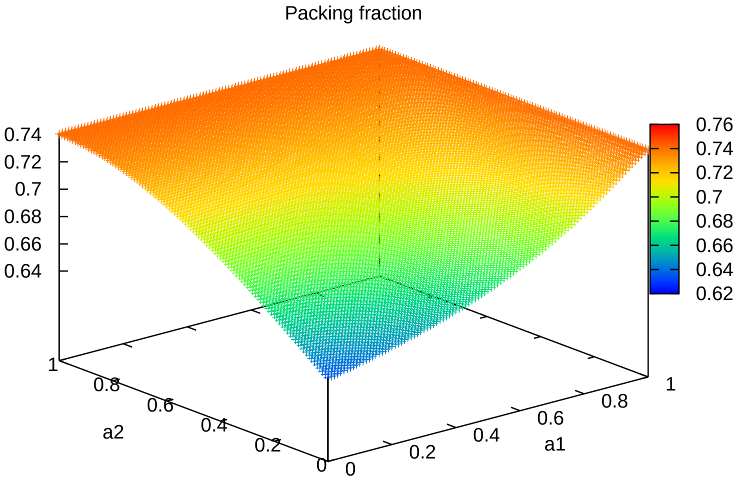

Figure 6.1: Densest packing with one particle in the unit cell. This result was achieved by numerical simulations. Shown is $101^2 - 200 + 1 = 10002$ different geometries. a_1 and a_2 is varied in steps of 0.01 from 0 to 1. These results are confirmed analytically by Elizabeth R Chen via eq. (6.2).

The densest packing configuration for three different shapes, the sphere $(a_1, a_2) = (1, 1)$ an intermediate shape $(a_1, a_2) = (0.5, 0.5)$ and the rotated Reuleaux triangle $(a_1, a_2) = (0, 0)$, is shown in figure 6.2. Here 4 particles are shown to visualize how they arrange for densest packing if there is one particle in the unit cell.

The packing fraction for the most anisotropic shape ($a_1 = a_2 = 0$) is found numerically to be 0.63563 and for the sphere 0.74048. These results are consistent with the analytical solution found by Elizabeth R Chen:

$$\begin{aligned}\phi(b_1, b_2) =& \frac{\pi}{\sqrt{18}}\Bigg[1 + 3(b_2 - b_1)\sqrt{b_1(b_1 + 2b_2)} \\ &+ 3b_1^2 - 3b_2^2 \arcsin\left(\frac{\sqrt{b_1(b_1 + 2b_2)}}{b_1 + b_2}\right)\Bigg]\end{aligned} \tag{6.2}$$

where b_1 and b_2 is defined as: $b_1 = 1 - a_1$ and $b_2 = 1 - a_2$. The $a_1 = a_2 = 0$ shape is seen to be[1]:

$$\phi(1, 1) = \frac{\pi(4 - \pi)}{\sqrt{18}} \simeq 0.63563... \tag{6.3}$$

Consistent with our numerical finding.

---

[1] Recall: $\pi = 3 \arcsin(\sqrt{3}/2)$.

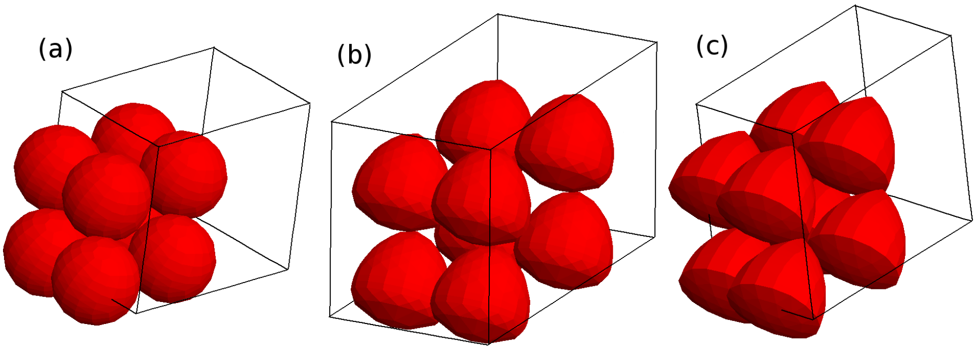

Figure 6.2: Configurations for densest packing with one particle in the unit cell. (a) is the sphere with parameters and packing fractions: $a_1 = a_2 = 1, \phi \simeq 0.74$, (b) is an intermediate shape with parameters: $a_1 = a_2 = 0.5, \phi \simeq 0.71$ and (c) is the most anisotropic shape with parameters $a_1 = a_2 = 0, \phi \simeq 0.64$.

6.2 Two particles in the unit cell

Having more than one particle in the unit cell increases the densest packing. This is expected because it resembles a tetrahedra which is known to fill more than 85 % of space if packed well [Chen 2010].

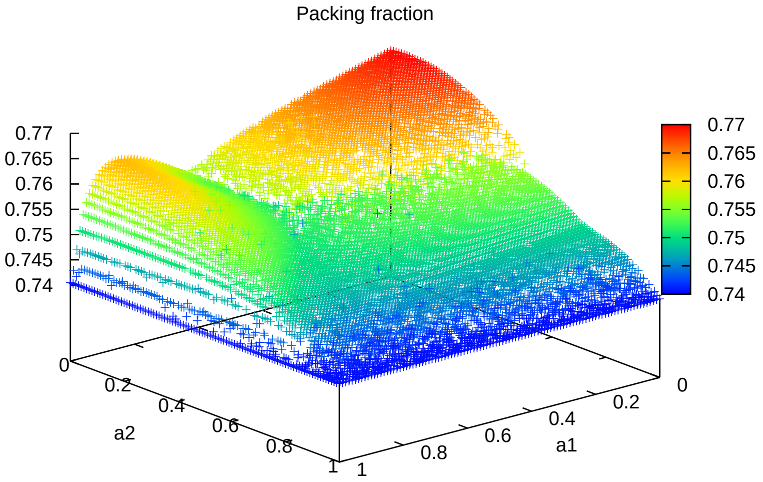

Figure 6.3: Densest packing for two particles in the unit cell. Topologically different domains are clearly visible, a_1 and a_2 are varied in steps of 0.01 from 0 to 1 giving 10002 different geometries. The packing fraction clearly exceeds the densest packing for spheres.

In figure 6.3 the densest packing for two particles in the unit cell is plotted. It seems as the $a_1 = a_2 = 0$ particle is the most space filling particle, but a closer look reveals that it is the $(a_1, a_2) = (0.00, 0.07)$ with a packing fraction $= 0.7698...$ compared to the 0.7696... for the most anisotropic (0, 0) particle. We plot the two borders of figure 6.3 with $a_1 = 0$ and $a_2 = 0$ in figure 6.4 where a maximum is present for the (0.00, 0.07) particle. We also notice that the algorithm does not always find the densest arrangement. It is clear that there are different topological domains and it happens that the algorithm finds an arrangement at a domain with lower packing fraction. On figure 6.4 the particle $(a_1, a_2) = (0.00, 0.27)$ has a packing fraction of ~ 0.755 equal to the green domain in figure 6.3, but it is expected to be in the yellow-orange domain. Longer simulations with more iterations could potentially solve this problem.

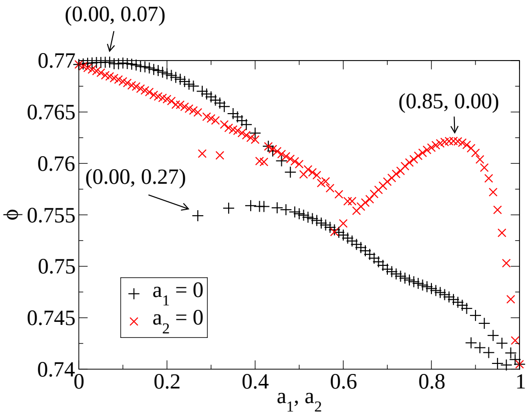

Figure 6.4: Packing fraction lines for $a_1 = 0$ and $a_2 = 0$. The densest packing is not $a_1 = a_2 = 0$, but $a_1 = 0$ and $a_2 = 0.07$ as indicated in the figure. This arrangement and the $(a_1, a_2) =$ (0.85, 0.00) together with (0.20, 0.60) is shown in figure 6.5.

Three different configurations: $(a_1, a_2) = \{(0.85, 0.00); (0.20, 0.60); (0.00, 0.07)\}$, belonging to three different topological domains are shown in figure 6.5. For ease of visualization, particles pointing up are colored blue and particles pointing down are colored red. Two adjacent layers, in the (0.85, 0.00) particle densest packing arrangement, are separated vertically and horizontally by approximate one particle diameter whereas the (0.00, 0.07) particle arrangement is separated close to half a particle diameter. The layers in the (0.20, 0.60) particle arrangement are mixed between the two other arrangements. The packing fractions are written in the figure caption. A more detailed analysis is required to understand these different domains.

Simulations with three and four particles in the simulation box was performed, but did not reach higher packing fractions. Furthermore the algorithm had difficulties finding the optimal packing for all the particles. Three and four particles in the simulation box led to a mix between the one and two versions with no higher packing fraction. See appendix C.1.

6.3 Conclusions for densest packing

Densest packing for the rolypoly with one and two particles in the unit cell is reported in figure 6.1 and 6.3. For one particle in the unit cell we found an analytical solution

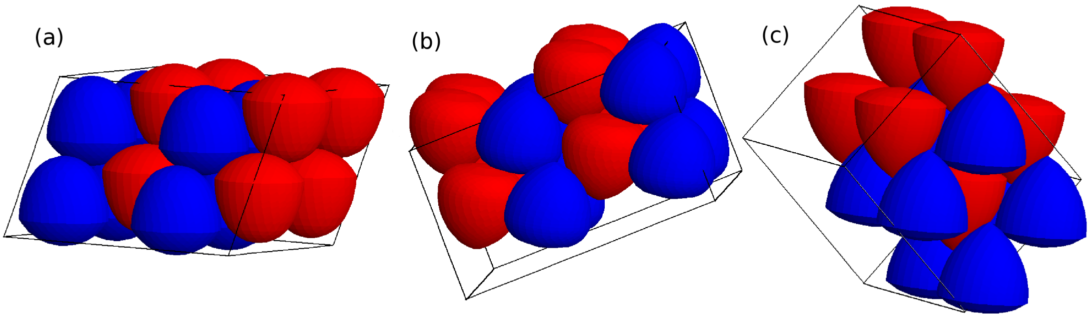

Figure 6.5: Densest particle arrangements for two particles in the unit cell. (a) is the $(a_1, a_2) = (0.85, 0.00)$ particle with a packing fraction of 0.7621, (b) is the $(a_1, a_2) = (0.20, 0.60)$ particle with a packing fraction of 0.7521 and (c) is the $(a_1, a_2) = (0.00, 0.07)$ particle with a packing fraction of 0.7698. These configurations represent different topological domains. All particles are identical, but the particles pointing up are colored blue and the particles pointing down are colored red.

confirming our numerical results. The densest packing is less dense for one particle in the unit cell and more dense for two particles in the unit cell. The highest density achieved for two particles in the unit cell is the $(a_1, a_2) = (0.00, 0.07)$ particle with a packing fraction $\simeq 0.7698...$ Densest packing for two particles in the unit cell displayed a variety of different topological domains. Three and four particles in the unit cell did not display higher packing fractions than two particles in the unit cell.

Chapter 7

The glass-forming ability

The mean nucleation time $\langle\tau\rangle$ is calculated from NPT simulations by averaging over 20-50 independent runs. We find that these nucleation time curves display a minima $\langle\tau^*\rangle$ when plotted as a function of pressure and corresponds to the glass forming ability of the particle. The glass forming ability increases with increasing anisotropy. The high pressure part of the nucleation time curves are dominated by the self diffusion coefficient consistent with classical nucleation theory. An estimation of the crystallization packing fraction ϕ_{cryst} is made and compared to the isoperimetric quotient (iq) (asphericity). From simulations for the crystallization packing fraction ϕ_{cryst}, the glass forming ability $\langle\tau^*\rangle$ and densest packing for one particle in the simulation box, we suggest the rolypoly can, to a first approximation, be reduced to depend on one parameter: the iq.

The glass forming ability is a measure of a particles abilities to crystallize. We define it as the minimum of the nucleation time τ, the time before a nucleation start and grows. We use the NPT ensemble and adopt the same procedure as [Pedersen 2011], performing 20-50 simulations at each state point and record a mean crystallization time $\langle\tau\rangle$. The order parameter used to detect crystallization is a volume change of the simulation box. A critical packing fraction ϕ_c was chosen as a boundary between liquid and solid phases and the nucleation time is defined to be the time when the packing fraction $\phi(t)$ equals the critical packing fraction ϕ_c: $\phi(\tau) = \phi_c$. In figure 7.1 we plot an example of how the nucleation time was determined where the packing fraction as a function of time steps is shown for 20 identical simulations with different initial conditions. All simulations are performed with 1000 particles and the critical packing fraction between liquid and solid was in this case: $\phi_c \sim 0.56$.

We investigate finite size effects by simulating the sphere with 100, 500, 1000, 2000, 4000 and 8000 particles, and extract the mean nucleation time $\langle\tau\rangle$. The system should be large enough to have several nucleation sites during the simulation. For systems with less than 1000 particles the mean nucleation was considerable smaller than simulations with more than 1000 particles. See figure C.2 in appendix C.2 for system size dependence on $\langle\tau\rangle$. [Pusey 2009] et al. also studied finite size dependence of the hard sphere and found that there was no difference in the nucleation time for systems with 2000 and 100 000 particles. The absolute values of the glass forming ability is not important as long as we are consistent in all our simulations.

We produced consistency simulations with 1000 particles at low pressure to confirm the pressure – packing fraction liquid line of the hard sphere phase diagram [Mulero 2008].

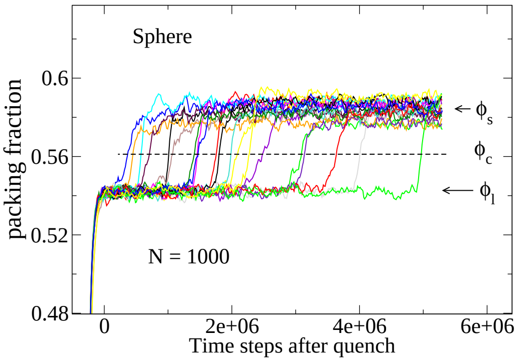

Figure 7.1: Detection of crystallization. 20 independent simulations with different initial conditions was quenched from a dilute system with low pressure to the desired pressure. The liquid and solid packing fractions are denoted with ϕ_l and ϕ_s respectively and the critical packing fraction is denoted ϕ_c .

See section C.3 in appendix C.

All shapes crystallize into a rotator fcc structure (plastic crystal) consistent with e.g. the hard ellipsoids [Letz 2000]. It therefore makes sense to compare the crystallization times for different particles. See figure 7.6 for an example of a simulation that crystallized into a rotate fcc lattice.

We select a number of particles on the diagonal $a_1 = a_2$ and some with a_2 equal to zero to study in detail. We perform NPT simulations at different pressures for each shape and plot the mean nucleation time against pressure.

Figure 7.2 show the mean nucleation time as a function of reduced pressure. The pressure is measured in units of $[V_p/k_BT]$ where V_p is the volume of the particle and we use the unit system with $k_BT = 1$. These findings are consistent with [Pusey 2009] where the mean nucleation time is extracted for hard spheres and poly disperse solutions. They study hard spheres and polydisperse systems by molecular dynamics simulations in the NVT ensemble. The main conclusions are that that increasing polydispersity slows down crystal nucleation and above a certain limit of polydispersity, crystallization is completely avoided. In their NVT simulations they find the minima of the nucleation time curve $\langle\tau^*\rangle$ of the hard spheres to have a packing fraction: $\phi(\langle\tau^*\rangle) = 0.56$, consistent with our liquid packing fraction at pressure $p^* = 11.5$ giving $\phi(\langle\tau^*\rangle) = 0.555$.

From figure 7.2 it seem as there exist some universal behavior for the high pressure part of the mean nucleation time curves. At low pressure nucleation is slow and diverges towards the melting pressure. Just above the melting pressure the thermodynamic driving force $(\Delta\mu)$ is small and increases with increasing pressure. The thermodynamic driving

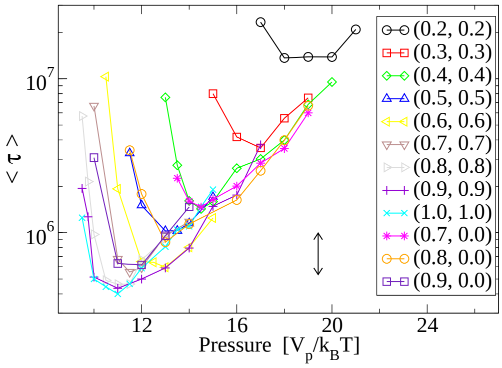

Figure 7.2: Glass forming ability for different shapes, the two numbers in the legend indicate the particle parameters (a_1, a_2). The minimum of the sphere $(a_1, a_2) = (1.0,\ 1.0)$ has pressure $11.5V_p/k_BT$. At this pressure, the liquid packing fraction is ~ 0.555 consistent with [Pusey 2009] who found 0.56 as the minima for their nucleation time. The arrow indicates a typical standard deviation on a datum point. Standard deviations becomes a little smaller for fast crystallization and a little higher for slow crystallization. Time are measured in units of MC sweeps.

force can to a first approximation be written:

$$\Delta\mu \approx -\Delta V(p - p_m)\,, \tag{7.1}$$

where $\Delta V = V_{liquid} - V_{solid}$ is the volume difference between liquid and solid phases p_m is the melting pressure. At high pressure kinetics become slow and starts dominating the nucleation. According to Classical Nucleation Theory (CNT) the nucleation rate k is proportional to the diffusion coefficient. The nucleation rate is given by [Turnbull 1949]:

$$k = A(T)\exp\left\{-\frac{\Delta G^*}{k_BT}\right\}, \tag{7.2}$$

where ΔG^* is the height of the free energy barrier and $A(T)$ is a kinetic prefactor proportional to the diffusion coefficient. Inserting the prefactor $A(T)$ and the Gibbs free energy from CNT [ten Wolde 1996] leads to

$$k = \sqrt{\frac{\Delta\mu}{6\pi k_BTN_c}}\,\frac{24D_sN_c^{2/3}}{v_l\lambda^2}\exp\left\{-\frac{16\pi\gamma^3v_s}{3k_BT(\Delta\mu)^2}\right\}. \tag{7.3}$$

In this expression we have: $\Delta\mu =$ as the chemical potential between the solid and liquid, $N_c = -\frac{32}{3}\pi v_s\gamma^3(\Delta\mu)^{-3}$ is the size of the critical nucleus (expressed in numbers of particles), λ is an atomic length, v_s and v_l is the volume per particle in the solid and liquid respective, γ is the surface tension, T is temperature and last but not least we have D_s as the self-diffusion constant. The nucleation time τ is inversely proportional to the diffusion coefficient $\langle\tau\rangle \propto D_s^{-1}$.

We calculate the diffusion coefficient from the mean squared-displacement of the particles and because we are dealing with NPT simulations where the size of the box fluctuates, length is ill defined and the mean-squared displacement does not make sense. Instead we extract the self diffusion coefficient in the liquid phase from NVT simulations at packing fractions corresponding to pressures lower than the melting pressure. The diffusion coefficient is found by fitting to the mean-squared displacement [Allen 2010] :

$$D_s = \lim_{t\to\infty} \frac{1}{6t} \langle |\mathbf{r}(t) - \mathbf{r}(0)|^2 \rangle \,. \tag{7.4}$$

With units of area per time. We assume the pressure dependence on the diffusion coefficient

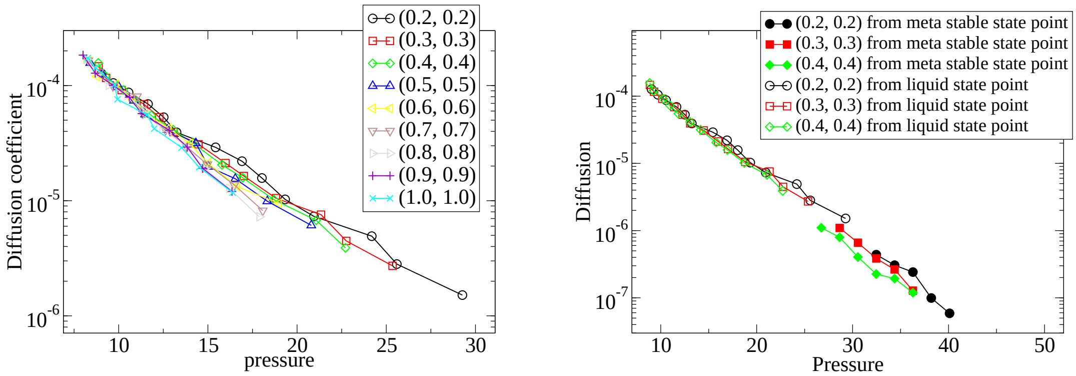

Figure 7.3: Diffusion vs. pressure. Assuming a straight line in this plot means diffusion as a function of pressure is described by an exponential function: $D(p) = c1 \exp\left(-\frac{p}{c_2}\right)$ with c_1 and c_2 being fitting constants. Numbers in the legend refer to the particle parameters (a_1, a_2). Left: From liquid state points. Right: comparing with diffusion calculated from meta-stable state point.

to be exponential (Arrhenius behavior):

$$D_s(p) = c_1 \exp\left(-\frac{p}{c_2}\right) \,, \tag{7.5}$$

where c_1 and c_2 are constants and extrapolated into the meta stable state points. We ensure that particles have moved a minimum of 10 diameters (100 in the mean-squared displacement) in average to ensure long time behavior.

From figure 7.3 we conclude that this relation is obeyed to a good approximation. For some state points in the meta stable regime it was possible to calculate the diffusion coefficient because it did not crystallize and it was possible to simulate long time behavior as seen in figure 7.3.

From CNT we have that diffusion is proportional to the nucleation rate. Our nucleation times $\langle\tau\rangle$ time diffusion are according to CNT then predicted to be constant. In order to check this we define the diffusion length to be:

$$l_{D_s} = \sqrt{\langle\tau\rangle D_s} \,. \tag{7.6}$$

The diffusion length are then plotted as a function of pressure in figure 7.4. At low pressure diffusion is not controlling the nucleation time, the high nucleation time is due to the low thermodynamic driving force, see eq. (7.1). At high pressure, the diffusion lengths are approaching a constant value, indicating diffusion is dominating this part of the curves.

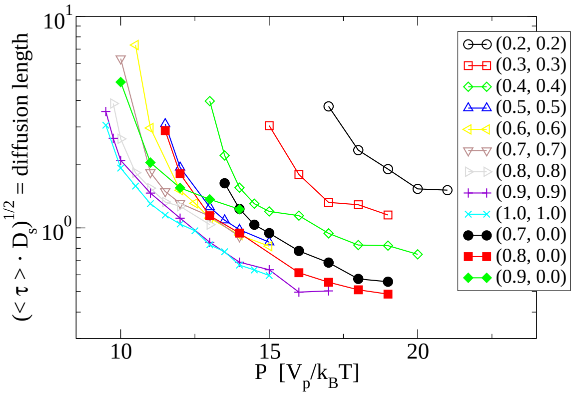

Figure 7.4: Diffusion length = square root of glass forming ability times self diffusion plotted against pressure. The legend indicate the particle with parameters (a_1, a_2). At high pressures the curves seem to approach a constant value indicating diffusion is controlling this regime.

In order to check the universality of these curves we would have liked to subtract the thermodynamic driving force by plotting the diffusion length as $p - p_m$, but since we do not have a good estimate for the melting pressure we can not do this.

[Pusey 2009] et al. discuss three different nucleation regimes. The first regime corresponds to conventional CNT where a nucleus must grow large enough to overcome the free energy barrier and is the steep part of the diffusion length curves. [Auer 2001] calculated this barrier height for the hard spheres and found that it dropped rapidly from packing fractions 0.521 - 0.534. Interpolating their results suggest that this height becomes comparable to k_BT at packing fractions $0.55 - 0.56$ [Pusey 2009] corresponding to pressures 10 - 11 — around the minima of the nucleation time curves $\langle\tau\rangle$ for the hard spheres. CNT assumes homogeneous nucleation where one critical nucleus start the entire crystallization process. We believe that we have heterogeneous nucleation nucleation with several nucleation sites present in the sample.

The second regime is where nucleation only requires to move about one particle diameter. The authors of [Pusey 2009] suggest that we should refer to this regime as spinodal nucleation where the driving force is strong and there is practically no free energy barrier to overcome. The particles just need to rearrange in order to crystallize. This is where our diffusion length is approximate one.

The third regime corresponds to higher pressure and packing fractions. In this regime the nucleation time becomes small compared to the relaxation time. We do not see any evidence of this regime and the authors of [Pusey 2009] does not understand or explain the mechanisms of this regime.

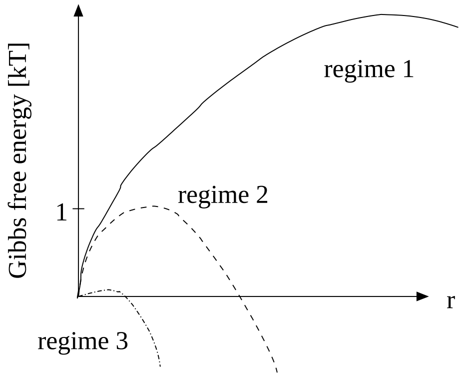

Figure 7.5: Sketch of the three different nucleation regimes. Classical Nucleation Theory predict: $\Delta G \propto r^3 c_{bulk} + r^2 c_{surf}$ with constants $c_{bulk} < 0$ and $c_{surf} > 0$.

A sketch of the free energy barrier in the three different regimes is drawn in figure 7.5. The Gibbs free energy for a spherical nucleation crystallite with radius r is according to CNT given by

$$\Delta G = \frac{4}{3}\pi r^3 \rho_s \Delta\mu + 4\pi r^2 \gamma \tag{7.7}$$

where ρ_s is the number density in the solid $\Delta\mu(< 0)$ is the chemical potential and γ is the surface tension. These two terms represent bulk and surface properties respectively. It is energetically favorable to create crystallites where it is unfavorable to create surface energy.

7.1 Liquid to solid crystallization packing fractions

In the previous section we calculated the nucleation rates. This was done in the NPT ensemble where we found a minimum pressure corresponding to the fastest nucleation time $\langle\tau^*\rangle$. At low pressure these curves are diverging towards the melting pressure. In this section we simulate 1000 particles in the NVT ensemble at different packing fractions and record the lowest packing fraction where crystallization is observed during the simulations. This packing fraction is higher than the freezing packing fraction ($\phi_{freeze} = 0.495$ for hard spheres) and will be named and denoted the crystallization packing fraction: ϕ_{cryst}

The crystallization packing fraction is a measure of how dense a particle need to be packed before it crystallizes. CNT predicts that the energy barrier to be crossed decreases with increasing packing fraction. Assuming CNT holds for the rolypolys the lowest packing fraction where crystallization is observed is a rough measure of the ability to crystallize. High packing fraction means good glass former and bad crystallizer.

Melting packing fractions was calculated for particles with parameters a_1 and a_2 in steps of 0.1 from 0 to 1 making a total of $11^2 - 19 = 102$ different particles[1]. It is done by simulating 1000 particles in the NVT ensemble starting from a liquid configuration

---

[1] Remember -19 comes from a_1 or a_2 equal one is a sphere

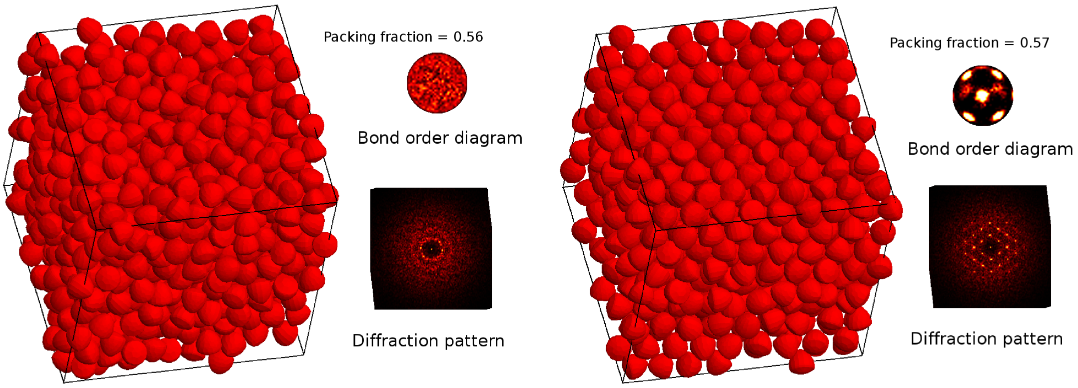

Figure 7.6: Detection of crystallization for the $(a_1, a_2) = (0.4, 0.4)$ particle. Left: is the final configuration together with the diffraction and bond order diagram shown for a simulation of $\sim 10^7$ MC sweeps at packing fraction 0.56. Right: Same simulation parameters, but at packing fraction 0.57. The simulation with $\phi = 0.57$ clearly crystallized where the simulation with $\phi = 0.56$ did not.

with a low packing fraction and increasing it in steps of 0.01 and record the packing fraction when crystallization first occurred. Crystallization was detected by examining the configuration visually, by the diffraction pattern and using the bond order diagram. An example of crystallization with the particle $(a_1, a_2) = (0.4, 0.4)$ can be seen in figure 7.6 where the configuration, diffraction pattern and bond order diagram for the nearest neighbor is shown for the final configuration ($\sim 10^7$ sweeps) for packing fractions 0.56 and 0.57.

Calculating a phase diagram accurately, requires in principle free energy calculations or advanced simulation techniques such as *Umbrella Sampling* or *Transition Path Sampling*. The main hurdle is that nucleation is a rare event and you should in principle wait infinitely time to assure the sample nucleates or melt. Here we simply simulate the different particles at different packing fractions. The more anisotropic it gets, the longer the simulations takes before it crystallizes. It was necessary to run the particle $(0, 0)$ for $\sim 10^8$ MC sweeps before it crystallized where the sphere only need $\sim 10^5$ MC sweeps. The results for the the packing fractions can be seen in figure 7.7.

With this method of determining the crystallization packing fraction, it is not certain, that a lower packing fraction does not crystallizes, if it was simulated longer and or with a different initial condition. It gives a rough estimate for the melting packing fraction. For the hard sphere we get $\phi_{cryst} = 0.53$ consistent being in the meta stable regime for the hard sphere model which has a melting packing fraction of 0.545 and a freezing packing fraction of 0.495 [Rintoul 1996].

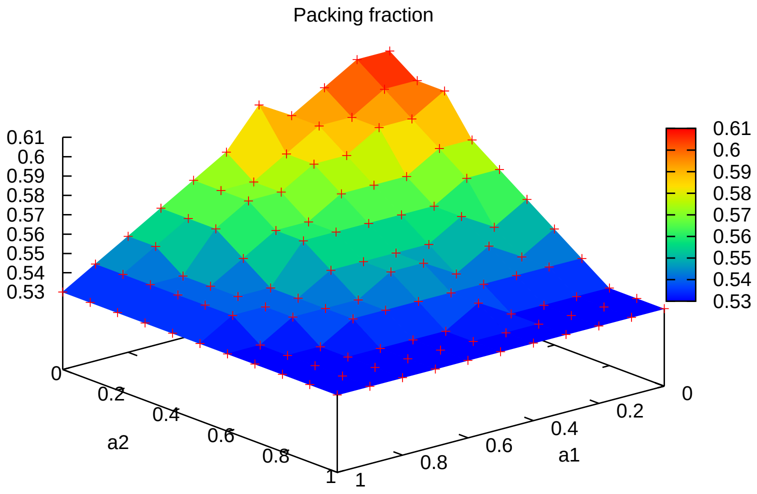

Figure 7.7: The lowest packing fraction where crystallization first was observed ϕ_{cryst}. This is at a higher packing fraction than the freezing packing fraction [Marechal 2011].

7.2 Reducing the rolypoly to one parameter

In this section we will argue that the rolypoly, to a first approximation, can be reduced to depend on one parameter: the **isoperimetric quotient** (iq) defined as

$$iq = 36\pi \frac{V^2}{S^3} , \tag{7.8}$$

where V is the volume and S is the surface of the particle. It is done by comparing the iq to the densest packing for one particle in the unit cell, our crystallizing packing fraction ϕ_{cryst} given in the previous chapter and the glass forming ability. As will become clear, these measures, the densest packing for one particle and the lowest packing fraction where crystallization was observed resembles the iq. For the iq and densest packing, we have analytical solutions and they are not identical, but deviates only little.

The isoperimetric quotient is defined in eq. (7.8) and has a lowest upper bound being one for a sphere. It is a measure of the deviations from a sphere, the lower iq is, the less spherical the particle is.

As can be seen in figure 7.8 the isoperimetric quotient is very similar in shape to the densest packing for one particle in the simulation box, but they are not identical as can be seen by inspection of the densest packing equation (6.2) and the volume and surface of the

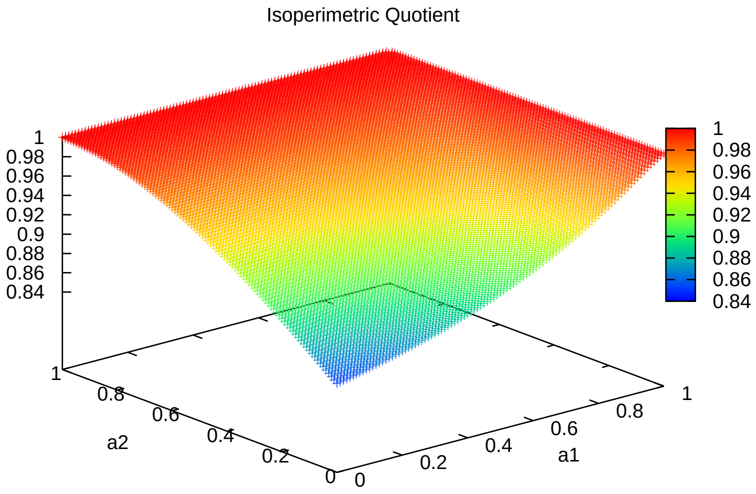

Figure 7.8: Isoperimetric quotient for the rolypoly. The most aspherical particle has a $iq = 0.852...$

rolypoly:

$$\begin{aligned} V(b_1, b_2) =& \frac{4\pi}{3}\Bigg[1 + 3(b_2 - b_1)\sqrt{b_1(b_1 + 2b_2)} \\ &+ 3b_1^2 - 3b_2^2 \arcsin\left(\frac{\sqrt{b_1(b_1+2b_2)}}{b_1+b_2}\right)\Bigg] \\ S(b_1, b_2) =& 2\pi\Bigg[2 + 2(b_2 - b_1)\sqrt{b_1(b_1 + 2b_2)} \\ &+ 2b_1^2 - 2b_2^2 \arcsin\left(\frac{\sqrt{b_1(b_1+2b_2)}}{b_1+b_2}\right)\Bigg] \end{aligned} \tag{7.9}$$

Remember $b_1 = 1 - a_1$ and $b_2 = 1 - a_2$. It is seen that the densest packing is proportional to the volume and not the surface and therefore $iq(a_1, a_2) \neq \Gamma\phi_{\text{dens}}(a_1, a_2)$ with Γ being the same proportionality constant for all particles and the subscript: dens, indicating that it is densest packing.

Likewise it seems as the crystallizing packing fraction $\phi_{cryst}(a_1, a_2)$ is proportional to the iq. We address this question by plotting the densest packing as a function of iq in figure 7.9 where it is seen that the curves to a first approximation is linear.

7.2.1 Comparing this work to hard aspherical spheres

[Miller 2010] et al. study the crystallization of hard aspherical particles by generating a number of random aspherical particles by random perturbations to the sphere. On each particle they perform a set of NPT simulations from low to high pressure and detect whether or not the particles crystallize during the simulation. They divide all their particles

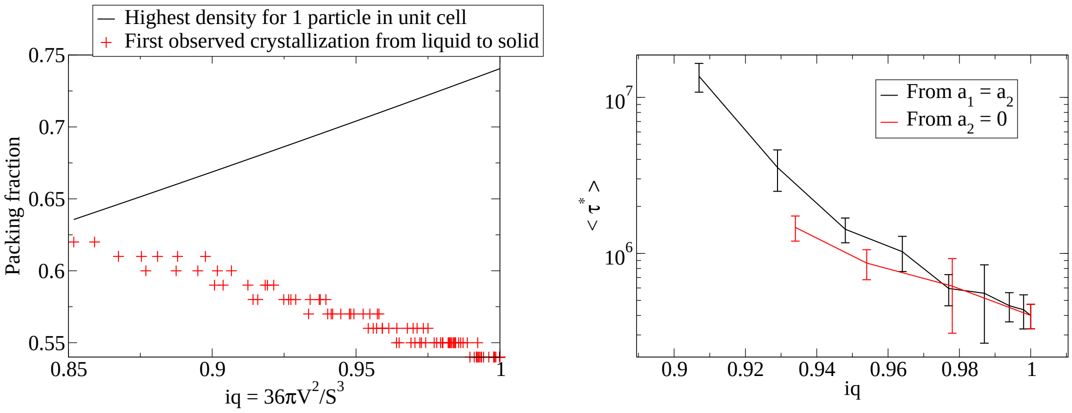

Figure 7.9: Left: The densest packing and crystallization packing fraction $\phi_{cryst}(a_1, a_2)$ as a function of iq. $\phi_{cryst}(a_1, a_2)$ is discretized in steps of 0.01, but is too a first approximation linear. Right: The glass forming ability calculated as the fastest nucleation time: $\langle\tau^*\rangle$. Black line is particles from the diagonal with $(a_1, a_2) = (0.2, 0.2)$ being the most aspherical. The error bars represent one standard deviation.

into two regimes: particles that easily crystallize and particles that does not and find that they need two parameters to describe the boundary between particles that easily crystallize and particles that does not. The first is the asphericity A, defined in terms of volume to surface ratio of a particle $\alpha_p = S_p/V_p$ with respect to that of a sphere $\alpha_s = S_s/V_s$ is:

$$A = 1 - \frac{\alpha_p}{\alpha_s} \tag{7.10}$$

The second parameter is the orientational symmetry q. It is constructed from the eigenvalues of the inertia tensor I_{ij} as

$$q = \frac{({\lambda_1}^2 - {\lambda_2}^2)^2 + ({\lambda_1}^2 - {\lambda_3}^2)^2 + ({\lambda_2}^2 - {\lambda_3}^2)^2}{2(\lambda_1^2 + \lambda_2^2 + \lambda_3^2)^2} \tag{7.11}$$

with λ_1, λ_2 and λ_3 being the three principal eigenvalues. q and A are constructed so they both are 0 for a sphere and increase with increasing asphericity with 1 being the upper bound for extremely aspherical particles. Figure 7.10 show these two parameters for the rolypoly, they are well inside the region that easily crystallize consistent with the conclusion of [Miller 2010] because all the rolypolys crystallize. In [Miller 2010] there is no distinction about how easy (or hard) a particle crystallize. If it crystallized during the simulation, then it crystallized easily and the border between easy and hard to crystallize is only approximate. Here we have tried to answer the question: *how easy does it crystallize, if it crystallize.*

7.3 Glass forming ability conclusions

The mean nucleation time $\langle\tau\rangle$ was calculated at different pressures for a selected number of particles. These curves exhibit a minima corresponding to the fastest mean nucleation time $\langle\tau^*\rangle$ = *glass forming ability*. Right part of figure 7.9 shows that the glass forming

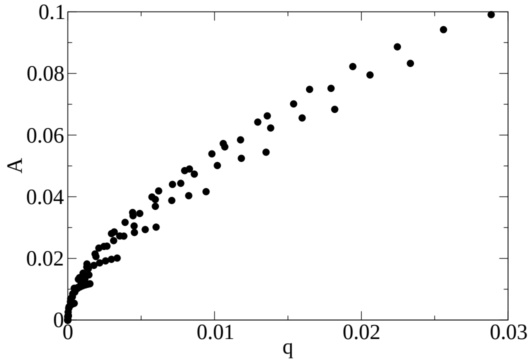

Figure 7.10: The asphericity A and orientational symmetry q as defined in the text for particles with a_1 and a_1 varied from 0 to 1 in steps of 0.1.

ability depends to a first approximation linearly on $\langle \tau^* \rangle$ in a log plot: $\langle \tau^*(iq) \rangle \approx \exp(iq)$. For high pressures the nucleation times are controlled by diffusion consistent with classical nucleation theory.

The densest packing for crystallization $\phi_{cryst}(a_1, a_2)$ (figure 7.7) and the crystallization packing fraction $\phi_{cryst}(a_1, a_2)$ (figure 7.7) clearly resembles the isoperimetric quotient (figure 7.8). The rolypoly can to a first approximation be reduced to depend on one parameter: the isoperimetric quotient iq. These results are consistent with [Miller 2010].

Appendix A

Derivations for shear viscosity and modulus

In this appendix we derive the macro- and micro-scopic definitions of the stress tensor. It is based on: [Hansen 1986] and [Landau 2005].

A.1 Macroscopic description of the stress tensor σ_{ij}

The stress tensor defines the stress at a specific point (x, y, z) in space and can be divided into a normal stress and a shear stress. Where the normal stress is perpendicular to the surface and the shear is tangential. From figure A.1 it is clear that the normal stress will tend to change the volume (bulk) and the shear will change the shape of the volume considered. The volume considered is a small volume inside the liquid and we look at what the stress on that volume is. The average normal and shear stress on the surface is scalar quantities

$$\sigma_n = \frac{F_n}{A}, \qquad \sigma_s = \frac{F_s}{A} \tag{A.1}$$

where it is seen that the normal stress corresponds to the hydrostatic pressure. In general the stress is a second order tensor σ_{ik} representing nine components completely describing the stress at any point in any direction. The normal stress is the diagonal elements and corresponds to the negative pressure:

$$\sigma_{ik} = -p\delta_{ik} \tag{A.2}$$

The shear stress is the off diagonal elements where the first entry describes the plane where the shear acts and the second entry is the direction of the shear on that plane.

If the volume considered in figure A.1 changes its shape due to shear stress it is strained. The amount it is displaced $x_1 - x_0$ due to the deformation of the tangential force on the volume is denoted by Δx.

$$\Delta x = x_1 - x_0 \tag{A.3}$$

The strain is given as the displacement length Δx with respect to the height y_h of the volume. Notice that these directions are perpendicular to each other.

$$\varepsilon = \frac{\Delta x}{y_h} \tag{A.4}$$

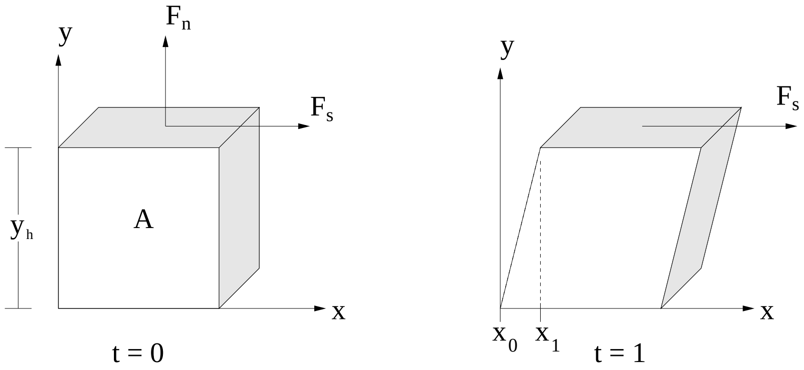

Figure A.1: (a) Normal and shear stress. (b) displacement due to shear stress.

See figure A.1. Considering infinitesimal distances and therefore small deformations, the strain tensor is to a first order approximation given by:

$$\varepsilon_{ij} = \frac{1}{2}\left(\frac{\partial \varepsilon_i}{\partial x_j} + \frac{\partial \varepsilon_j}{\partial x_i}\right) \tag{A.5}$$

and is seen to be symmetric.

Stress and strain tensors are related by a generalized hooks law:

$$\sigma_{ij} = c_{ijkl}\varepsilon_{kl} \tag{A.6}$$

where the fourth order elasticity tensor c_{ijkl} has $4^3 = 81$ entries. Symmetry considerations can reduce this number to two independent quantities representing a pure shear deformation and a bulk (hydrostatic) deformation. These are in material science called the shear and bulk modulus respectively (usually denoted by G and K) and reflects the rigidity and compressibility. In what follows we use G and K as notation for shear and bulk respectively. Notice Hansen and McDonald [Hansen 1986] use the notation η and ζ as shear and bulk. Because we deal with highly viscous liquids one can argue in favor for both a solid and a liquid.

$$\sigma_{ij} = 2G\varepsilon_{ij} + \left(K - \frac{2}{3}G\right)\delta_{ij}\varepsilon_{ll} \tag{A.7}$$

The diagonal elements of the stress $\sigma_{ii} = 3K\varepsilon_{ii}$ is associated with a pure volume change. The hydrostatic pressure is given by $p = -\frac{1}{3}\sigma_{ii}$. The off diagonal elements $(i \neq j)$ represents a volume preserving, but shape changing shear viscosity $\sigma_{ik} = 2G\varepsilon_{ij}$.

A.2 Microscopic description of shear and stress

In computer simulations, the shear viscosity can be calculated using the autocorrelation function of an off diagonal element of the stress tensor (in this case the xy component).

$$G(t) = \frac{N}{\rho k_B T}\left\langle \sigma^{xy}(t)\sigma^{xy}(0)\right\rangle \tag{A.8}$$

This is what we will refer to as the transient elastic moduli. A microscopic expression of the stress tensor can be derived by looking at the particle current

$$\mathbf{j}(\mathbf{r},t) = \sum_{i=1}^{N} \mathbf{u}_i(t)\delta[\mathbf{r} - \mathbf{r}_i(t)] \tag{A.9}$$

where $\mathbf{u}_i(t)$ is the velocity of particle i at time t, $\delta[\mathbf{r} - \mathbf{r}_i(t)]$ gets the local position of the particle i. Taking the Fourier transform of (A.9) and multiplying with mass m one arrives at

$$m\frac{\mathrm{d}\mathbf{j_k}^{\alpha}}{\mathrm{d}t} = m\sum_{i=1}^{N}\left(\frac{\mathrm{d}\mathbf{u}_{i\alpha}}{\mathrm{d}t} - ik_{\beta}\mathbf{u}_{i\alpha}\mathbf{u}_{i\beta}\right)\exp[-i\mathbf{k}\cdot\mathbf{r}_i] \tag{A.10}$$

α denotes any spatial direction x, y or z and β is in the direction of the wave vector k. Recognizing the first term as the force and rewriting it in terms of the potential of the system one can use the continuity equation for particle momenta

$$m\frac{\mathrm{d}\mathbf{j}^{\alpha}_{\mathbf{k}}(t)}{\mathrm{d}t} + ik\sigma_{\mathbf{k}}^{\alpha\beta}(t) = 0 \tag{A.11}$$

to get a microscopic expression for the stress tensor:

$$\sigma_{\mathbf{k}}^{\alpha\beta} = \sum_{i=1}^{N}\left(m\mathbf{u}_{i\alpha}\mathbf{u}_{i\beta} + \frac{1}{2}\sum_{j\neq i}^{N}\frac{r_{ij\alpha}r_{ij\beta}}{r_{ij}^2}\Phi_{\mathbf{k}}(\mathbf{r_{ij}})\right)\exp[-i\mathbf{k}\cdot\mathbf{r}_i], \tag{A.12}$$

where $\Phi_{\mathbf{k}}(\mathbf{r_{ij}})$ is a function containing the potential. Taking the $k \to 0$ limit and inserting the Φ function. The stress tensor becomes

$$\sigma^{\alpha\beta} = \sum_{i=1}^{N}\left(m\mathbf{u}_{i\alpha}\mathbf{u}_{i\beta} - \frac{1}{2}\sum_{j\neq i}^{N}\frac{r_{ij\alpha}r_{ij\beta}}{r_{ij}}\frac{\mathrm{d}v(\mathbf{r}_{ij})}{\mathrm{d}r_{ij}})\right). \tag{A.13}$$

As seen in the general formula for the stress tensor (A.13) it contains two terms. The first one which is associated the particle momenta in the α direction times the velocity in the β direction. This term transfer momentum in the transverse direction, from α to β. The second term is purely configurational, contains only positions, and will be much larger than the kinetic term at normal liquid densities. It is also noted that the stress tensor is symmetric.

For our investigations we will only consider the second term – **the excess shear stress**. This term will dominate at normal liquid densities and is what we want to observe. The isomorph theory is for excess quantities.

Appendix B

Isomorphs for potentials with three terms

Data shown for isomorphs with 3 terms in the potential defined as

$$v_{m,n,k}(r) = a\left(\frac{\sigma}{r}\right)^m + b\left(\frac{\sigma}{r}\right)^n + c\left(\frac{\sigma}{r}\right)^k . \tag{B.1}$$

and redefined in terms of α and the generalized LJ potential eq. (2.1):

$$v_{m,n,k}(r) = (1-\alpha)v_{m,n}(r) + \alpha v_{m,k}(r) . \tag{B.2}$$

with $m = 12$, $n = 6$ and $k = 8$.

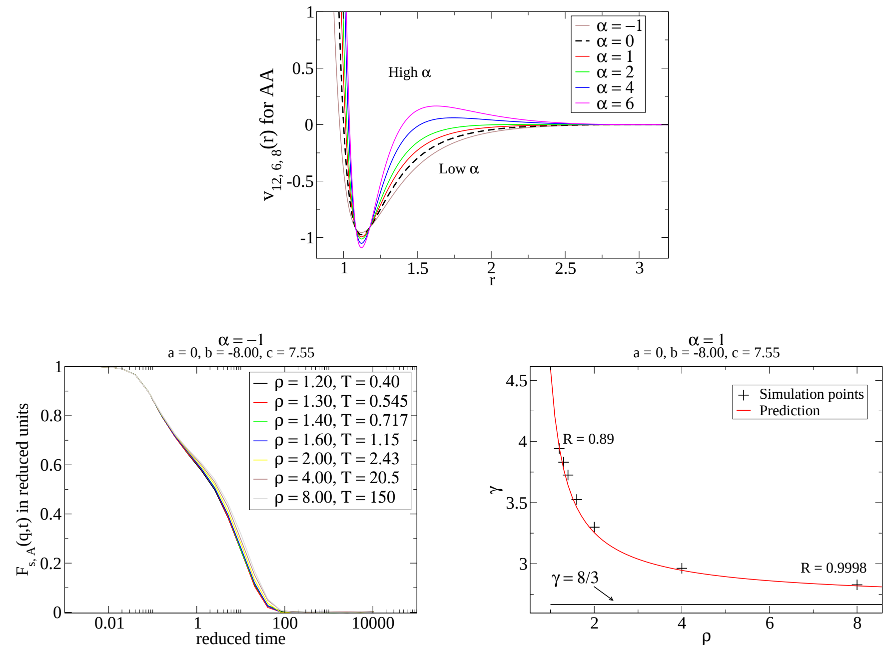

Figure B.1: Top: Potentials for the A interaction plotted. Left: Dynamics is probed by the self part of the incoherent intermediate scattering function $F_s(\tilde{q}, \tilde{t})$ for the A particles with $\tilde{q} = 7.25(\rho/1.20)^{1/3}$. Right: The prediction of $\gamma(\tilde{\rho})$.

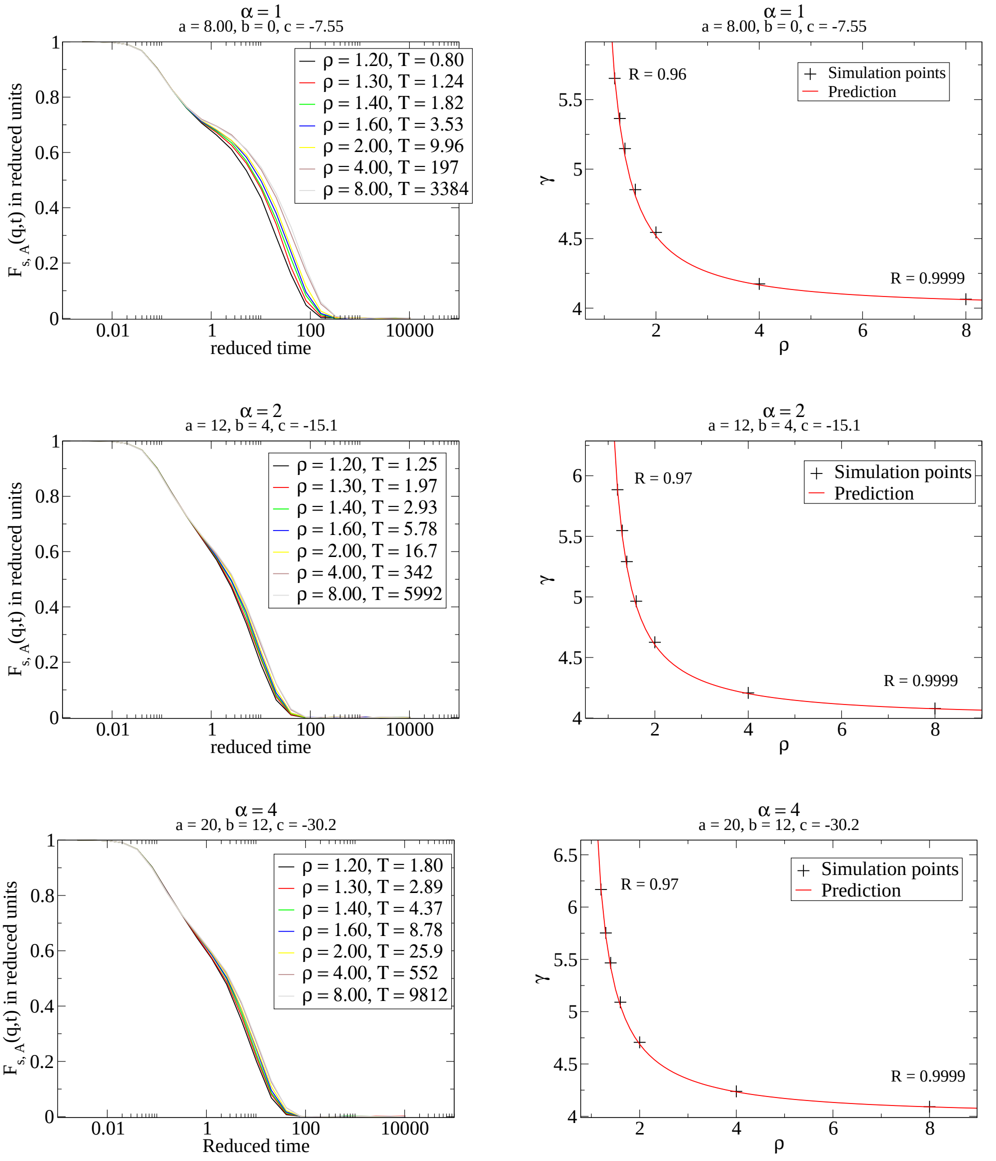

Figure B.2: Left: Dynamics is probed by the self part of the incoherent intermediate scattering function $F_s(\tilde{q}, \tilde{t})$ for the A particles with $\tilde{q} = 7.25(\rho/1.20)^{1/3}$. Right: The prediction of $\gamma(\tilde{\rho})$. Top two figures are the system with $\alpha = 1$, in the middle $\alpha = 2$ and bottom is $\alpha = 1$.

Appendix C

Rolypolys

C.1 Three and four particles in the unit cell

We investigate if three or four particles in the unit cell can be arranged to achieve a denser packing than two particles in the unit cell. Figure C.1 show the results for both three and four where it is seen that it is not the case. Actually the three particles in the unit cell arrange into packings similar to the one particle in the unit cell. This merely shows that the algorithm does not find the optimal packing fraction. It is a mix between the one and two particles in unit cell packing fractions.

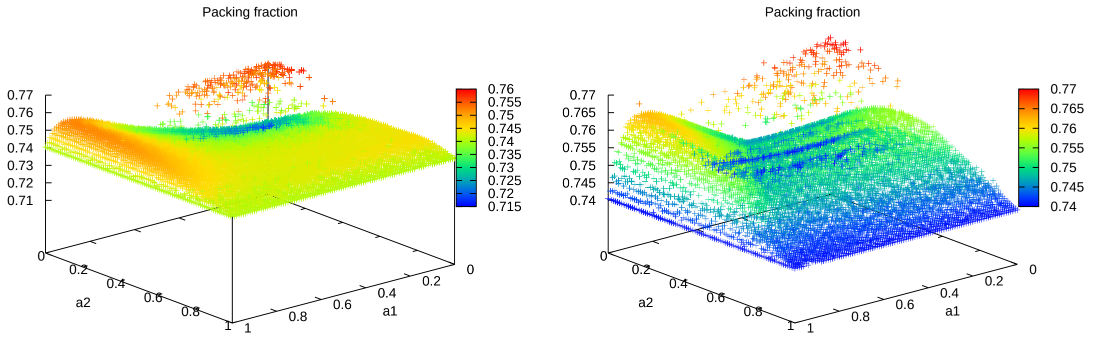

Figure C.1: Left: Densest packing simulations with 3 particles in the unit cell. Right: Densest packing with 4 particles in the unit cell.

C.2 System size dependence

In figure C.2 we plot the mean nucleation time $< \tau >$ as a function of numbers of particles in the simulation box. The error bar indicate one standard deviation.

The mean nucleation time increases slightly with increasing particles in the simulation box. Going from 1000 particles with $\langle \tau \rangle \sim 40 * 10^3$ to 16000 particles with $\langle \tau \rangle \sim 50 * 10^3$, the nucleation time has increased with 25% where the number of particles have increased with 1600%.

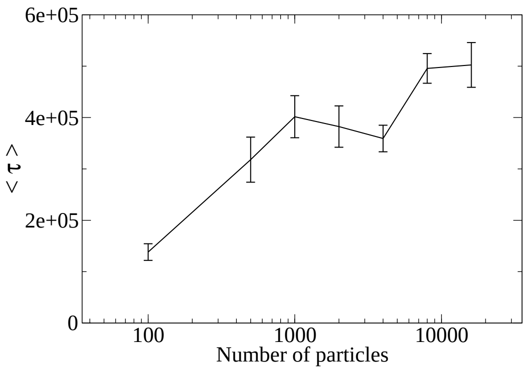

Figure C.2: System size dependence for the sphere at pressure 11. There is a small increase in $\langle \tau \rangle$ with increasing the number of particles.

C.3 Hard sphere liquid line

We reproduce the hard sphere packing fraction - liquid equilibrium line for 1000 particles in the simulation box. Figure C.3 show simulation data with error bars and figure shows literature data with picture taken from `www.sklogwiki.org/SklogWiki/index.php/Hard_sphere_model`. The shaded area corresponds to the range in figure C.4.

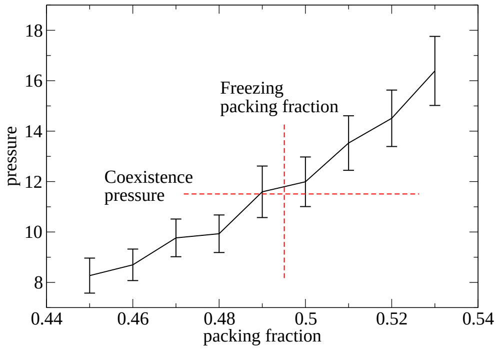

Figure C.3: Packing fraction versus pressure for the hard spheres. The broken red lines indicate the coexistence pressure and freezing packing fraction. Error bars indicate one standard deviation. Pressure units is $[\sigma^3/k_BT]$ with σ being diameter of the sphere. Converting our $[V/k_BT]$ units to diameter units, we simple scale with $6/\pi$.

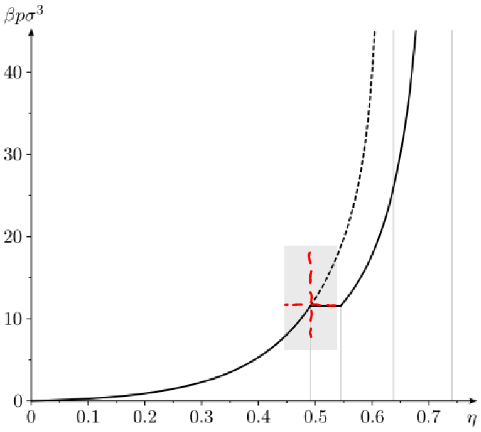

Figure C.4: Phase diagram for hard spheres. The shaded area corresponds approximately to the range in the left figure. Pressure units is $[\sigma^3/k_BT]$ with σ being diameter of the sphere.

Bibliography

[Ahmed 2009] Alauddin Ahmed and Richard J. Sadus. *Solid-liquid equilibria and triple points of n-6 Lennard-Jones fluids.* The Journal of Chemical Physics, vol. 131, no. 17, page 174504, 2009. (Cited on page 61.)

[Alba-Simionesco 2002] Christiane Alba-Simionesco, Daniel Kivelson and Gilles Tarjus. *Temperature density and pressure dependence of relaxation times in supercooled liquids.* Journal of Chemical Physics, vol. 116, no. 5033, 2002. (Cited on page 40.)

[Alba-Simionesco 2004] C. Alba-Simionesco, A. Cailliaux, A. AlegrÃa and G. Tarjus. *Scaling out the density dependence of the α relaxation in glass-forming polymers.* EPL (Europhysics Letters), vol. 68, no. 1, page 58, 2004. (Cited on page 40.)

[Allen 2010] M. P. Allen and D. J. Tildesley. Computer simulation of liquids. Oxford Science Publications, Oxford New York, 2010. (Cited on pages 4 and 86.)

[Angell 1995] C. A. Angell. *Formation of Glasses from Liquids and Biopolymers.* Science, vol. 267, pages 1924–1935, 1995. (Cited on page 15.)

[Ashcroft 1976] Neil W Ashcroft and N. David. Mermin. Solid state physics. Oxford University Press, 1976. (Cited on page 41.)

[Auer 2001] Stefan Auer and Daan Frenkel. *Prediction of absolute crystal-nucleation rate in hard-sphere colloids.* Nature, vol. 409, no. 6823, 2001. (Cited on page 87.)

[Bailey 2008a] Nicholas P. Bailey, Ulf R. Pedersen, Nicoletta Gnan, Thomas B. Schrøder and Jeppe C. Dyre. *Pressure-energy correlations in liquids. Paper I. Results from computer simulations.* Journal of Chemical Physics, vol. 129, no. 184507, 2008. (Cited on page 4.)

[Bailey 2008b] Nicholas P. Bailey, Ulf R. Pedersen, Nicoletta Gnan, Thomas B. Schrøder and Jeppe C. Dyre. *Pressure-energy correlations in liquids. Paper II. Analysis and consequences.* Journal of Chemical Physics, vol. 129, no. 184508, 2008. (Cited on pages 4, 24, 58 and 59.)

[Barron 1957] T.H.K Barron. *Gruneisen parameters for the equation of state of solids.* Annals of Physics, vol. 1, no. 1, pages 77 – 90, 1957. (Cited on page 41.)

[Berthier 2009] Ludovic Berthier and Gilles Tarjus. *Nonperturbative Effect of Attractive Forces in Viscous Liquids.* Phys. Rev. Lett., vol. 103, page 170601, Oct 2009. (Cited on page 55.)

[Bolhuis 1997a] P. G. Bolhuis, D. Frenkel, Siun-Choun Mau and David A. Huse. *Entropy difference between crystal phases.* Nature, vol. 388, pages 235–236, 1997. (Cited on pages 73 and 77.)

[Bolhuis 1997b] Peter Bolhuis and Daan Frenkel. *Tracing the phase boundaries of hard spherocylinders.* The Journal of Chemical Physics, vol. 106, no. 2, pages 666–687, 1997. (Cited on page 73.)

[Chen 2010] ElizabethR. Chen, Michael Engel and SharonC. Glotzer. *Dense Crystalline Dimer Packings of Regular Tetrahedra.* Discrete and Computational Geometry, vol. 44, pages 253–280, 2010. (Cited on pages 73, 74 and 79.)

[Coslovich 2008] D. Coslovich and C.M. Roland. *Thermodynamic scaling of diffusion in supercooled liquids Lennard-Jones liquids.* Journal of Physical Chemistry B, vol. 112, no. 5, pages 1329–1332, 2008. (Cited on page 46.)

[Damasceno 2012a] Pablo F. Damasceno, Michael Engel and Sharon C. Glotzer. *Crystalline Assemblies and Densest Packings of a Family of Truncated Tetrahedra and the Role of Directional Entropic Forces.* ACS Nano, vol. 6, pages 609–614, 2012. (Cited on page 73.)

[Damasceno 2012b] Pablo F. Damasceno, Michael Engel and Sharon C. Glotzer. *Predictive Self-Assembly of Polyhedra into Complex Structures.* Science, vol. 337, no. 6093, pages 453–457, 2012. (Cited on page 73.)

[de Graaf 2012] Joost de Graaf and Liberato Manna. *A Roadmap for the Assembly of Polyhedral Particles.* Science, vol. 337, no. 6093, pages 417–418, 2012. (Cited on page 73.)

[Dyre 1996] Jeppe C. Dyre, Niels Boye Olsen and Tage Christensen. *Local elastic expansion model for viscous-flow activation energies of glass-forming molecular liquids.* Phys. Rev. B, vol. 53, pages 2171–2174, Feb 1996. (Cited on page 15.)

[Dyre 2006] Jeppe C. Dyre. *The glass transition and elastic models of glass-forming liquids.* Reviews of Modern Physics, vol. 78, page 953, 2006. (Cited on page 3.)

[Dyre 2012] Jeppe C. Dyre and Wei Hua Wang. *The instantaneous shear modulus in the shoving model.* Journal of Chemical Physics, vol. 136, page 224108, 2012. (Cited on page 21.)

[Dyre 2013] Jeppe C. Dyre. *NVU perspective on simple liquids' quasiuniversality.* Phys. Rev. E, vol. 87, page 022106, Feb 2013. (Cited on page 30.)

[Ediger 2012] M. D. Ediger and Peter Harrowell. *Perspective: Supercooled liquids and glasses.* The Journal of Chemical Physics, vol. 137, no. 8, page 080901, 2012. (Cited on page 3.)

[Fulcher 1925] G. S. Fulcher. -. J. Am. Ceram. Soc, vol. 8, page 339, 1925. (Cited on page 33.)

[Glotzer 2007] Sharon C. Glotzer and Michael J. Solomon. *Anisotropy of building blocks and their assembly into complex structures.* Nature Materials, vol. 6, pages 557–562, 2007. (Cited on page 73.)

[Gnan 2009] N. Gnan, T. B. Schrøder, U. R. Pedersen, N. P. Bailey and J. C. Dyre. *Pressure-energy correlations in liquids. Paper IV. "Isomorphs" in liquid phase diagrams.* Journal of Chemical Physics, vol. 131, no. 234504, 2009. (Cited on pages 4, 5, 6, 15, 17, 38 and 41.)

[Gundermann 2011] Ditte Gundermann, Ulf R. Pedersen, Tina Hecksher, Nicholas P. Bailey, Bo Jakobsen, Tage Christensen, Niels B. Olsen, Thomas B. Schrøder, Daniel Fragiadakis, Riccardo Casalini, C. Michael Roland, Jeppe C. Dyre and Kristine Niss. *Predicting the density-scaling exponent of a glass-forming liquid from Prigogine-Defay ratio measurements.* Nature Physics, vol. 7, pages 816–821, 2011. (Cited on page 57.)

[Hansen 1986] J. P. Hansen and I. R. McDonald. Theory of simple liquids. Academic Press, second édition, 1986. (Cited on pages 11, 23, 29, 51, 61, 95 and 96.)

[Hoover 1985] William G. Hoover. *Canonical dynamics: Equilibrium phase-space distributions.* Phys. Rev. A, vol. 31, pages 1695–1697, Mar 1985. (Cited on page 4.)

[Ingebrigtsen 2012] Trond S. Ingebrigtsen, Thomas B. Schrøder and Jeppe C. Dyre. *What is a simple liquid?* Physical review X, vol. 2, no. 011011, 2012. (Cited on page 61.)

[Khinchin 1934] Aleksandr Khinchin. *Dette er en test.* Matematische Annalen, vol. 109, pages 604–615, 1934. (Cited on page 22.)

[Khrapak 2011] Sergey A. Khrapak and Gregor E. Morfill. *Accurate freezing and melting equations for the Lennard-Jones system.* The Journal of Chemical Physics, vol. 134, no. 9, page 094108, 2011. (Cited on page 61.)

[Kob 1994] Walter Kob and Hans C. Andersen. *Scaling Behavior in the β-Relaxation Regime of a Supercooled Lennard-Jones Mixture.* Phys. Rev. Lett., vol. 73, pages 1376–1379, Sep 1994. (Cited on pages 7, 11, 15 and 42.)

[Kohlrausch 1854] Rudolf Kohlrausch. *Theorie des elektrischen Ruckstandes in der Leidner Flasche.* Annalen der Physik und Chemie, vol. 91, pages 56–82, 1854. Poggendorff. (Cited on page 27.)

[Landau 2005] L. D. Landau and E. M. Lifshitz. Theory of elasticity, volume 7 of *Course of Theoretical Physics*. Elsevier, 3 édition, 2005. (Cited on page 95.)

[Letz 2000] M. Letz, R. Schilling and A. Latz. *Ideal glass transitions for hard ellipsoids.* Phys. Rev. E, vol. 62, pages 5173–5178, Oct 2000. (Cited on pages 74 and 84.)

[Marechal 2011] Matthieu Marechal, Alejandro Cuetos, Bruno Martínez-Haya and Marjolein Dijkstra. *Phase behavior of hard colloidal platelets using free energy calculations.* The Journal of Chemical Physics, vol. 134, no. 9, page 094501, 2011. (Cited on pages 73 and 90.)

[Michele 2004] Cristiano De Michele, Francesco Sciortino and Antonio Coniglio. *Scaling of soft spheres: fragility invariance on the repulsive potential softness.* Journal of Physics: Condensed Matter, vol. 16, page L489, 2004. (Cited on page 33.)

[Miller 2010] William L. Miller, Behnaz Bozorgui and Angelo Cacciuto. *Crystallization of hard aspherical particles.* The Journal of Chemical Physics, vol. 132, no. 13, page 134901, 2010. (Cited on pages 91, 92 and 93.)

[Mulero 2008] Angel Mulero. Theory and simulations of hard-sphere fluids and related systems. Springer, 2008. (Cited on page 83.)

[Ni 2012] Ran Ni, Anjan Prasad Gantapara, Joost de Graaf, Rene van Roij and Marjolein Dijkstra. *Phase diagram of colloidal hard superballs: from cubes via spheres to octahedra.* Soft Matter, vol. 8, pages 8826–8834, 2012. (Cited on page 73.)

[Nosé 1984] Shuichi Nosé. *A unified formulation of the constant temperature molecular dynamics methods.* The Journal of Chemical Physics, vol. 81, no. 1, pages 511–519, 1984. (Cited on page 4.)

[Pedersen 2008] Ulf R. Pedersen, Nicholas P. Bailey, Thomas B. Schrøder and Jeppe C. Dyre. *Strong Pressure-Energy Correlations in van der Waals Liquids.* Phys. Rev. Lett., vol. 100, page 015701, Jan 2008. (Cited on page 4.)

[Pedersen 2010] Ulf R. Pedersen, Thomas B. Schrøder and Jeppe C. Dyre. *Repulsive Reference Potential Reproducing the Dynamics of a Liquid with Attractions.* Phys. Rev. Lett., vol. 105, page 157801, Oct 2010. (Cited on pages 45 and 46.)

[Pedersen 2011] Ulf R. Pedersen and Peter Harrowell. *Factors Contributing to the Glass-Forming Ability of a Simulated Molecular Liquid.* The Journal of Physical Chemistry B, vol. 115, no. 48, pages 14205–14209, 2011. (Cited on page 83.)

[Puosi 2012] F. Puosi and D. Leporini. *Correlation of the instantaneous and the intermediate-time elasticity with the structural relaxation in glassforming systems.* Journal of Chemical Physics, vol. 136, page 041104, 2012. (Cited on page 21.)

[Pusey 2009] P.N. Pusey, E. Zaccarelli, C. Valeriani, E. Sanz, W.C.K Poon and M.E. Cates. *Hard Spheres: Crystallization and Glass formation.* Phil. Trans. R. Soc. A, vol. 367, no. 1909, pages 4993–5011, 2009. (Cited on pages 83, 84, 85 and 87.)

[Rintoul 1996] M. D. Rintoul and S. Torquato. *Metastability and Crystallization in Hard-Sphere Systems.* Phys. Rev. Lett., vol. 77, pages 4198–4201, Nov 1996. (Cited on page 89.)

[Rosenfeld 1998] Y. Rosenfeld and P. Tarazona. *Density functional theory and the asymptotic high density expansion of the free energy of classical solids and fluids.* Molecular Physics, vol. 95, no. 2, pages 141–150, 1998. (Cited on pages 15 and 22.)

[Schrøder 2009] Thomas B. Schrøder, Nicholas P. Bailey, Ulf R. Pedersen, Nicoletta Gnan and Jeppe C. Dyre. *Pressure-energy correlations in liquids. Paper III. Statistical mechanics and thermodynamics of liquids with hidden scale invariance.* Journal of Chemical Physics, vol. 131, no. 234503, 2009. (Cited on pages 4 and 41.)

[Schrøder 2011] Thomas B. Schrøder, Nicoletta Gnan, Ulf R. Pedersen, Nicholas Bailey and Jeppe C. Dyre. *Pressure-energy correlations in liquids. Paper V. Isomorphs in generalized Lennard-Jones systems.* Journal of Chemical Physics, vol. 134, no. 164505, 2011. (Cited on pages 4, 5, 6, 7, 8, 14 and 41.)

[Sullivan 1981] Donald E. Sullivan and C. G. Gray. *Evaluation of Angular correlation parameters and the dielectric constant in the RISM approximation.* Molecular Physics, vol. 42, no. 2, pages 443–454, 1981. (Cited on page 51.)

[Tamman 1926] G. Tamman and W. Z. Hesse. -. Anorg. Allgem. Chem., vol. 156, page 245, 1926. (Cited on page 33.)

[Tarjus 2004] Gilles Tarjus, Daniel Kivelson, Stefano Mossa and Christiane Alba-Simionesco. *Disentangling density and temperature effects in the viscous slowing down of glassforming liquids.* Journal of Chemical Physics, vol. 120, no. 6135, 2004. (Cited on page 40.)

[ten Wolde 1996] Pieter Rein ten Wolde, Maria J. Ruiz-Montero and Daan Frenkel. *Numerical calculation of the rate of crystal nucleation in a Lennard-Jones system at moderate undercooling.* The Journal of Chemical Physics, vol. 104, no. 24, pages 9932–9947, 1996. (Cited on page 85.)

[Tolle 2001] Albert Tolle. *Neutron scattering studies of the model glass former ortho - terphenyl.* Reports on Progress in Physics, vol. 64, no. 11, page 1473, 2001. (Cited on page 37.)

[Toxvaerd 2009] Søren Toxvaerd, Ulf R. Pedersen, Thomas B. Schrøder and Jeppe C. Dyre. *Stability of supercooled binary liquid mixtures.* The Journal of Chemical Physics, vol. 130, no. 22, page 224501, 2009. (Cited on pages 11 and 42.)

[Toxvaerd 2011] Søren Toxvaerd and Jeppe C. Dyre. *Communication: Shifted forces in molecular dynamics.* The Journal of Chemical Physics, vol. 134, no. 8, page 081102, 2011. (Cited on page 51.)

[Turnbull 1949] D. Turnbull and J. C. Fisher. *Rate of Nucleation in Condensed Systems.* The Journal of Chemical Physics, vol. 17, no. 1, pages 71–73, 1949. (Cited on page 85.)

[Vega 1997] C. Vega and P. A. Monson. *Plastic crystal phases of hard dumbbells and hard spherocylinders.* The Journal of Chemical Physics, vol. 107, no. 7, pages 2696–2697, 1997. (Cited on page 73.)

[Vogel 1921] Vogel. -. Z. Phys, vol. 22, page 645, 1921. (Cited on page 33.)

[Weeks 1971] John D. Weeks, David Chandler and Hans C. Andersen. *Role of Repulsive Forces in Determining the Equilibrium Structure of Simple Liquids.* Journal of Chemical Physics, vol. 54, no. 12, page 5237, 1971. (Cited on page 55.)

[Whitesides 2002] George M. Whitesides and Mila Boncheva. *Beyond molecules: Self-assembly of mesoscopic and macroscopic components.* Proceedings of the National Academy of Sciences, vol. 99, no. 8, pages 4769–4774, 2002. (Cited on page 73.)

[Wiener 1930] Norber Wiener. *Generalized Harmonic Analysis.* Acta Mathematica, vol. 55, pages 117–258, 1930. (Cited on page 22.)

[Yoshino 2010] Hajime Yoshino and Marc Mézard. *Emergence of Rigidity at the Structural Glass Transition: A First-Principles Computation.* Phys. Rev. Lett., vol. 105, page 015504, Jul 2010. (Cited on pages 15 and 21.)

[Zwanzig 1965] R. Zwanzig and R. D. Mountain. *High-Frequency Elastic Moduli of Simple Fluids.* Journal of Chemical Physics, vol. 43, no. 12, 12 1965. (Cited on pages 16 and 18.)

Summary

Part I investigates a class of generalized Lennard Jones potentials. They are all strongly correlating and so we use these systems to demonstrate a number of isomorph predictions. The transient elastic modulus exhibit a two step relaxation and it is argued that the plateau value of the transient elastic modulus $G_{\infty,p}$, compared to the truly instantaneous modulus G_∞, is the right quantity entering the elastic models. We confirm the Shoving model by demonstrating a linear dependence of the structural relaxation time, in a logarithmic plot, against $V_c G_{\infty,p}/T$ where V_c is a constant characteristic volume. The entire transient elastic modulus was found to be isomorph invariant when expressed in reduced units. Using Rosenfeld-Tarazona scaling for the potential energy and a result for isomorphs, we predict the temperature dependence of G_∞ on isochores and find good agreement with our data. We analyse two fundamentally different fitting functions and focus on the long time behavior of these. One having a finite relaxation time the other being the widely used stretched exponential with a diverging relaxation time. Our data indicates a finite relaxation time, but more investigations with better statistics are needed to make a final conclusion on this issue.

We have derived a generic form of density scaling from the isomorph definition. This isomorph scaling function was tested for a number of strongly correlating systems and seen to work extremely well. From the scaling function, the density dependence on the scaling exponent $\gamma(\rho)$ is found and seen to agree well with data. An analytical expression for the density scaling function is derived for systems interacting via a sum of inverse power law potentials. We show how the interaction potential relates to the density dependence of $\gamma(\rho)$. A direct relation linking the interatomic potential to the phase diagram, i.e. the shape of freezing and melting lines, is established.

Part II is devoted the study of a solid of constant width, named the rolypoly. Densest packings are found for this two parameter particle. Two particles in the unit cell reached the highest packing fraction of 0.7698. The glass forming ability, defined as a mean nucleation time, was calculated for a number of rolypolys and found, to a first approximation, to depend on the non sphericity of the particle. The crystallization packing fraction (a phase transition measure), densest packing for one particle in the unit cell and the glass forming ability indicates the rolypoly can be reduced to one parameter (the sphericity). At high pressures, the glass forming ability curves are controlled by the diffusion coefficient, consistent with classical nucleation theory.